SCHOOL OF INDUSTRIAL ENGINEERING OF BARCELONA

Physics Department

Advanced Nuclear Technologies Research Group

Development and validation of a simplified tritium migration simulation tool for its dynamic monitoring at ITER

MASTER'S FINAL PROJECT

Master's degree in Nuclear Engineering

Author: Jose Manuel Sojo Gordillo

Directed by: Lluis Batet Miracle
Elisabet Mas De Les Valls Ortiz

Barcelona, April 26, 2018

Abstract

The main objective of this work is to propose and validate a methodology for the implementation of a real time predictive tool into the ITER (International Thermonuclear Reactor) CODAC (Control, Data Access and Communication) system. Such tool should be able of predicting the amount of tritium present in every subsystem of the ITER tritium plant. The project framework is the cooperation between PROCON Systems, FUS ALLIANCE, IQS (Chemical Institute of Sarrià) and the ANT (Advanced Nuclear Technology) group of UPC.

This work is centred on the definition of each one of the steps considered in the methodology. First, a predictive tool is developed in order to calculate how tritium would spread over the system. This tool will be useful to create a database of perturbations simulations over the plant operation reference points. Then, such data will adjust simpler transfer functions called CPM (Condensate Parameter Model) which will be responsible of predict the tritium inventory in real time once implemented in the ITER CODAC system. Finally, the error of such tools is estimated too. Moreover, this works also deals with the characterization of hydrogen sensors developed by the IQS. Such sensors are able of measuring low hydrogen concentrations (from 60 ppm to 3000 ppm) at very high temperatures (500 °C). However, their response is slow and needs to be characterized.

All in all, this methodology provides the initial steps for the achievement of the project final aim, which is the whole control of ITER tritium plant.

Keywords: Fusion, ITER, Tritium inventory, Permeation, Predictive tool, Concentrate Parameter Model

Acknowledgments

This work would not had been possible without the support of the ARGOS Chairs's aid for the internship in the Advanced Nuclear Technology research group nor La Pedrera foundation's scholarship. Chemical Institute of Sarrià support and collaboration have been of an unquestionable help towards the realization of this work.

Contents

Abstract i

Acknowledgments i

Index iii

Preface ix
Introduction . . . ix
Backgound . . . ix
Global energy forecast . . . ix
The fusion roadmap . . . ix
ITER project . . . x
PROTOCODAC project . . . x
Objetives . . . xi
Research branches . . . xi
Scope of this work . . . xi
Software . . . xi
Contents . . . xii

1. Introduction to Fusion Technology 1
1.1. The fusion process . . . 1
1.1.1. Main reactions . . . 1
1.1.2. Lawson criteria for self sustained reaction . . . 2
1.2. Technical approaches . . . 2
1.2.1. Confinement strategies . . . 3
1.2.2. Reactor designs . . . 4
1.3. ITER reactor . . . 4
1.3.1. Main parts . . . 4
1.3.2. Operation . . . 7
1.3.3. Objectives . . . 7

2. The Tritium Plant 9
2.1. Fusion plant fuel cycle . . . 9
2.1.1. Breeding process . . . 9
2.1.2. Multiplier process . . . 9
2.2. Plant layout . . . 10

2.3. The breeding blanket . . . 12
2.3.1. Main objectives of TBS operation . . . 12
2.3.2. The HCLL TBM . . . 12
2.3.3. The HCPB TBM . . . 13
2.4. Tritium inventory management . . . 14
2.4.1. Monitoring . . . 14
2.4.2. Inventory control . . . 15

3. Fundamentals of Tritium Transport **17**
3.1. Introduction . . . 17
3.2. Transport mechanisms . . . 17
3.2.1. Advection . . . 17
3.2.2. Diffusion . . . 18
3.2.3. Sources . . . 18
3.3. Diffusive phenomena . . . 18
3.3.1. Solubility . . . 18
3.3.2. Permeability . . . 19
3.3.3. Sievert's law . . . 19
3.3.4. Trapping . . . 19
3.4. Superficial phenomena . . . 20
3.4.1. Dissociation-Recombination kinetics . . . 21
3.5. Useful relations . . . 21
3.6. Hydrogen capture . . . 22
3.6.1. Reaction . . . 22
3.6.2. PTC equilibrium curves . . . 23
3.6.3. Vant Hoff curve . . . 23
3.6.4. Hydride kinetics . . . 24
3.7. State of the art revision . . . 25

4. Predictive Transport Model **27**
4.1. Description . . . 27
4.2. Pipes . . . 27
4.2.1. Approach . . . 27
4.2.2. Balances . . . 28
4.3. Getter pebble bed . . . 29
4.3.1. Approach . . . 29
4.3.2. Balances . . . 30
4.4. Rooms . . . 32
4.5. Numerical schemes . . . 33
4.5.1. Advection . . . 33
4.5.2. Linearisation strategies . . . 33
4.5.3. Time . . . 34
4.5.4. Solver . . . 34

4.5.5. Solution algorithm 34

5. Condensate Parameters Model **35**
5.1. General description 35
5.2. CPM scope 36
5.3. Outlet concentration 37
5.3.1. Time domain function 37
5.3.2. Transfer function 37
5.4. Inlet concentration 38
5.4.1. Time domain function 38
5.4.2. Transfer function 38
5.4.3. Practical considerations 38
5.5. Pipe gas inventory 38
5.5.1. Time domain function 39
5.5.2. Transfer function 39
5.6. Wall inventory 39
5.6.1. Time domain function 40
5.6.2. Transfer function 40
5.7. Room pressure 40
5.7.1. Time domain function 41
5.7.2. Transfer function 41
5.8. Fitting methodology 41
5.8.1. Analytical formulas 41
5.8.2. Optimization algorithm 42
5.8.3. Variation with input variable 42
5.8.4. Example results 42

6. Hydrogen Detector Characterization **45**
6.1. Introduction 45
6.1.1. Sensor description 45
6.1.2. Sensor test reactor 46
6.2. Experiment 46
6.2.1. Flow uncertainties 47
6.2.2. Sensor calibration curve 48
6.2.3. Experimental data 49
6.3. Model 49
6.3.1. Time response 49
6.3.2. Sensor functions 53
6.3.3. Noise 53
6.4. Noise filter design 53
6.4.1. Hysteresis error corrector 54
6.4.2. Low-pass filters 54
6.4.3. Filter delay correction 57

6.5. Design of estimative function . . . 58
6.5.1. Time domain function . . . 58
6.5.2. Transfer function . . . 59
6.6. Results . . . 59
6.6.1. Simulation prediction . . . 60
6.6.2. Experiment data prediction . . . 60

7. Analysis of Model Errors **63**
7.1. Introduction . . . 63
7.2. Predictive model . . . 63
7.3. Total inventory . . . 63
7.4. CPM mismatches . . . 64
7.4.1. Case definition . . . 64
7.4.2. Comparison . . . 64
7.5. Sensor related errors . . . 66
7.5.1. Estimative error . . . 66
7.5.2. Sensor intrinsic error . . . 66

8. Experimental Set Up Design **67**
8.1. Introduction . . . 67
8.2. Material selection . . . 67
8.3. Designs . . . 68
8.3.1. Large layout . . . 68
8.3.2. Compact layout . . . 69
8.4. Foreseen results for experimental transient . . . 69
8.5. Proposed experiment . . . 70

9. Conclusions **75**
9.1. Predictive model . . . 75
9.2. CPM . . . 76
9.3. Sensor characterization tools . . . 76
9.4. Project budget . . . 77
9.5. Environmental impact study of the work . . . 78
9.6. Future research . . . 78

Bibliography **79**

Figure Index **85**

Table Index **86**

Appendices **89**

A. Nomenclature and Glossary **91**

B. Model equations **95**
B.1. Pipe 95
B.1.1. Constant matrix [**A**] terms 95
B.1.2. Balance to **HT** gas 95
B.1.3. Independent terms matrix [**B**] 98
B.2. Getter 100
B.2.1. Constant matrix [*A*] terms 100
B.2.2. Independent terms matrix [**B**] 106

C. Large Set Up Thermal Analysis **109**
C.1. Data 109
C.1.1. System of equations 111
C.1.2. Results 112

Preface

Introduction

The current master thesis deals with the development of a methodology able of monitorize tritium inventory all over the future ITER tritium plant. Modelling the tritium transport and the definition of effective and simple ways of predicting this inventory are the main goals of this work.

Antecedents

Global energy forecast

According to the BP Statistical Review of World Energy of 2017 [1], global energy demand is expected to double by the middle of this century. With fossil fuels providing the 80 % of the worldwide primary energy needs nowadays, the situation is completely unsustainable. The solution to this major problem is no other than a set of improvements in energy efficiency, renewable and nuclear sources. In this context, fusion energy, with its zero direct production of greenhouse gases, well distributed and virtually unlimited resources and its intrinsic safety in comparison with fission technology, is an important main character.

The fusion roadmap

In order to achieve a commercial plant by the second half of this century, an ambitious, yet realistic program is needed. The aim is to build and operate a commercial demonstrative reactor (DEMO) for those dates. With this objective targeted for near future, two main facilities must be built and operated before:

- ITER, the International Thermonuclear Experimental Reactor is the key element of this roadmap and also the critical path. It will allow to test all the technologies involved in fusion research at the same time in the same machine (since several milestones have been already achieved in different machines separately). This will challenge the technology and will teach experts how to solve problems minimizing the cost of this kind of reactor. Besides, it will provide large amounts of experience in operation, not only in plasma physics but in the rest of systems of this brand new kind of power plant.

- IFMIF, the International Fusion Materials Irradiation Facility needs to be built in parallel in order to qualify under intense neutron irradiation ($> 14\ MeV$, $> 10\ dpa$) new materials of the future reactors.

ITER project

As mentioned before, ITER is the bottleneck project in this roadmap. Its complexity is far beyond any similar fusion device ever built. As first of a kind project, many new technologies (some of them with redundant objectives) are going to be tested together. The aim is to generate the bigger knowledge and know-how outcome possible for the construction of a future commercial demonstration fusion plant.

The European contribution to this project is huge, since 50% of the budget is costed by Europe as the host member of the installation. The way ITER project has been designed claims for each of the members to develop their own designs (as commented, sometimes redundant) for all of the main parts. Hence, Europe is in charge of the construction of all those parts. Concerning the systems of interest of this work, the so called test blanket module, Europe has bet for two designs which will be tested simultaneously: the pebble bed and the lead lithium.

PROTOCODAC project

For safety reasons and operability, all nuclear facilities must control their radioisotopes inventory. ITER, as any fusion plant, is not an exception in this sense. Yet, those reactors are considerable different from conventional fission plans in some aspects. This steams for unique inventory control paradigms:

- The fuel is not solid, but a gas. Therefore, it is contained all over the systems that manage it. This leads to huge volumetric inventories of tritium (a forecast of 5-16 kg for a commercial fusion plant). Besides, its properties are quite unique. Tritium has an exceptionally permeability through metals. Hence, it has a enormous ease to leak. Besides, it has its own radiochemical interactions with materials.

- Comprehensive normative in terms of maximum error in tritium inventory estimations. This limits between regular checks are very narrow ($1\ g/year$ of maximum mismatch).

- Clear problems at its continuous monitoring. Nowadays there is not an effective and accurate enough solution for real time measurement of tritium. Sensors are not precise nor fast enough.

Hence, dynamic control of fuel inventory in complex systems (such as the ITER's tritium plant) is an unavoidable exigence for the operation flexibility expected for ITER as experiment.

Objetives

In this context, PROTOCODAC project (PROTO stands for prototype whereas CODAC is the acronym for Control, Data Access and Communication, the ITER control system) aims to develop a strategy, a methodology and finally a tool for continuous tritium balance matching. Its potential would be tested against a specific prototype demonstration.

Research branches

PROTOCODAC final success stands upon three main research branches:

- The development of an advanced simulation capacity in order to predict any likely transient scenario for the plant system. UPC-ANT is in charge of this part.
- The design of faster and more precise sensors (a measurement error lower than 5% and a response time of 1-10 s). IQS (Sarrià Chemical Institute) is in charge of this task.
- The design and implementation of a hardware/software CODAC architecture. This tool would use a database from the detailed simulation capacity in order to monitor tritium inventory in real time. UPC-ANT is as well in charge of the methodology, whereas PROCON Systems is in its implementation.

Scope of this work

The present work would show the first steps of the UPC-ANT research in the mentioned branches. In order to accomplish the first task, a sophisticated simulation code has been built. With the obtained results, a database is built. This would feed a set of simplified functions called Concentrated Parameters Model (now on CPM) specifically developed for its implementation in the CODAC interface.

Software

Due to the high complexity of the physics and phenomenology involved in the modelled system of this work, high level programming languages have been used. This is possible since computational performance is not a bottleneck any more nowadays.

For the built up of simple models (1D), data processing and transfer functions development, Python 3.6 coding language has been used [2]. On the other hand, in order to get detailed calculations used to validate simpler methods, a Computational Fluid Dynamic (CFD) code has been used. In this case, OpenFoam environment, on its fork version *foam-extend 4.0* has been used for that purpose [3]. Moreover, custom solvers originally developed by Mas de les Valls have been used [4].

Contents

The main topics of each chapter are summarized below:

1. Through the first chapter, basic principles of fusion energy are explained. The chapter covers from the basic reactions to the different fusion reactor designs. Additionally, ITER main objectives and parts are explained.

2. In the second chapter the blanket module and the basic idea behind will be discussed. The different European designs and their objectives are analysed. Besides, the ITER tritium plant main subsystems are discussed as well.

3. Then, chapter three develops the basics of tritium transport. All the phenomena involved in hydrogen permeation over metals are discussed. Moreover, basic principles of hydrogen storage for the tritium plant cleaning systems is discussed as well. Finally a state of the art research has been made regarding the transport parameters of the most commonly used materials for fusion devices.

4. Chapter four describes the model used for the predictive tritium calculations. Such model has shown to work way faster than alternative methods such as CFD, without loosing accuracy. Besides, a proposal for pebble bed getter systems has been developed for future implementations as well.

5. The fifth chapter describes the concept of Concentrated Parameter Model, a set of transfer functions that, when trained with the outcome of the predictive mode calculations in simple cases are able to predict complex perturbations. An example of its implementation is also discussed in this chapter.

6. Along chapter six an hydrogen sensor like the one IQS is developing is characterized thanks to the data provided by them. This way, parameters as response time and noise frequencies are deduced. This allows to develop some filter and predictive tools to both emulate a detector and filter the signals.

7. Then, an error assessment of each one of the tools described in the previous chapters is performed in chapter seven. This way, the order of magnitude of the model uncertainty is estimated.

8. In chapter eight, an exercise of design has been made. This design is intended to guide the future construction of an experiment by the IQS able to validate the predictive model presented in chapter 4. A selection of the optimal layout and material for this purpose is assessed.

9. Finally, conclusions regarding each step of the proposed methodology are described in the last chapter. Additionally, future steps in this project are discussed.

1. Introduction to Fusion Technology

1.1. The fusion process

Current nuclear power plants work with fission reactions, where massive nuclei are split in small pieces. These reactions are highly exothermic. By contrast, the so called fusion reactions are those nuclear reaction whose product are nuclei with higher mass number than any of the reactives involved. Those reactions are very exothermic as well. However, contrary to fission reactions, fusion ones need an extremely high pressure and temperature to take place. That is why this kind of reactions are the source of energy in stars.

1.1.1. Main reactions

Inside normal sized starts like the Sun, where the core temperature is below 15 million K, the main reaction that takes place is the proton-proton process:

$$4\,^{1}\mathrm{H} \rightarrow {}^{4}\mathrm{He} + 2\,^{1}\mathrm{e}^{+} + 2\bar{\nu} + 26.73MeV \tag{1.1}$$

There are also other mechanisms for fusion reaction inside more massive stars. Nevertheless, the technical interesting reactions are the ones involving other hydrogen isotopes since their cross sections are higher:

$$^{2}\mathrm{D} + {}^{3}\mathrm{T} \rightarrow {}^{4}\mathrm{He}(3.5MeV) + {}^{1}\mathrm{n}(14.1MeV) \tag{1.2}$$

$$^{2}\mathrm{D} + {}^{2}\mathrm{D} \rightarrow {}^{3}\mathrm{He}(0.82MeV) + {}^{1}\mathrm{n}(2.45MeV) \tag{1.3}$$

$$^{2}\mathrm{D} + {}^{3}\mathrm{He} \rightarrow {}^{4}\mathrm{He}(3.6MeV) + {}^{1}\mathrm{H}(14.7MeV) \tag{1.4}$$

For current fusion devices, the selected reaction is the deuterium-tritium because it is the one among the proposed with the highest cross section at the temperatures achievable with the technology available nowadays ($\sim 10^8$ K). Figure 1.1 shows a comparison between the reactivity of such reactions.

Nevertheless, the production of neutrons is not the most desirable outcome. for instance, protons, the result of D-^{3}He reaction, would be much more useful and easy to handle since they could be used to produce electricity directly. Besides, it is far easier to shield the reactor if the products are charged particles such as protons.

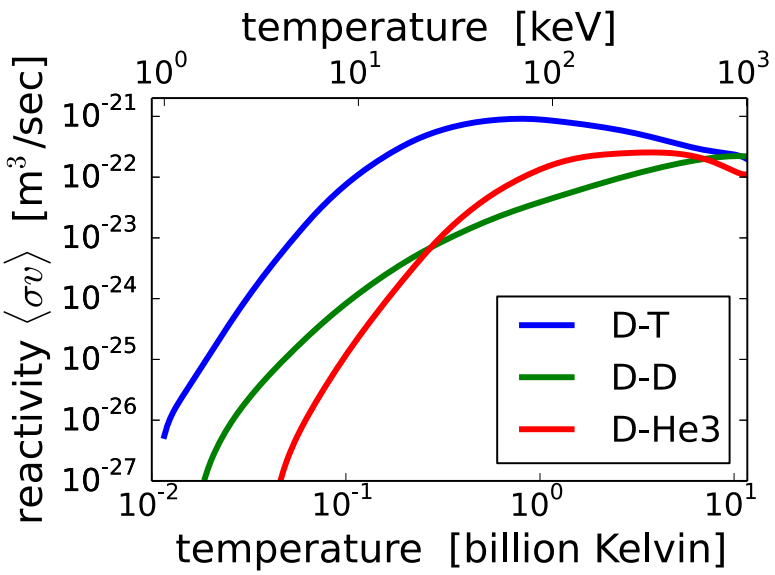

Figure 1.1.: Reactivity rate (average of cross-section times relative speed of reacting nuclei) comparison between the three most suitable fusion reactions as a function of temperature. The average is over Maxwellian ion distributions. Data extracted from [5].

1.1.2. Lawson criteria for self sustained reaction

As mentioned, in order to provoke this reactions huge amounts of energy are needed to reach such high temperatures. In order to achieve a self sustained reaction in which heat from the reactions itself is enough for keeping on the reaction, the so called Lawrson's criteria must be fulfilled [6]. This gives a threshold value for the product of density (n) and confinement time (t_E) of the particles in the plasma above which the fuel is self heated by the reaction for a given temperature T.

For the case of the D-T reaction, a minimum value of $nt_E > 1.5 \times 10^{20}$ s/m^3 is found for temperatures of 300 million K. This minimum roughly corresponds with the maximum cross section value of the D-T reaction seen in Figure 1.1. However, so far this condition has not ever been reached by any device. Hence, one of the ITER project aims is to achieve such conditions.

1.2. Technical approaches

From a strict scientific point of view, fusion are relatively well known nuclear reactions. Nevertheless, the technical challenges to overcome in order to achieve the necessary conditions are huge. This sections discusses the main ideas to built commercial and large scale fusion reactors.

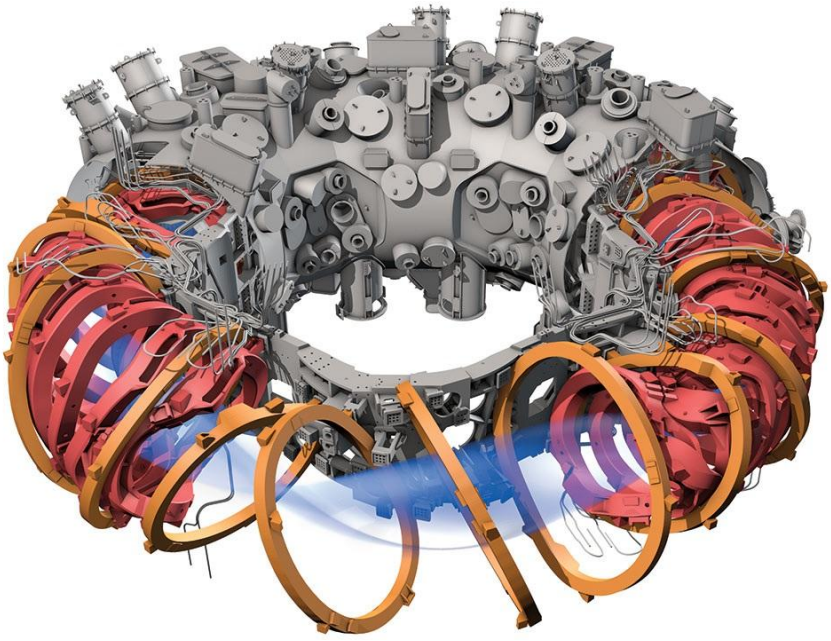

Figure 1.2.: Wendelstein 7-X Stellarator. Extracted from [7]

1.2.1. Confinement strategies

One of the main challenges is to reach the plasma to the extreme temperature and pressure conditions in a sufficient period of time (according to Lawson criteria). Two main plasma confinement techniques have been developed so far:

- Inertial: The use of powerful lasers can concentrate small pebbles (0.1 to 1 mm diameter) of fuel mixture for a short period of time (nanoseconds) up to the conditions needed to achieve the reaction (densities thousands of times higher than solid matter). Obviously, this technique consists in a discontinuous operation mode, although cycles can be shortened up to several pebbles per second.

- Magnetic: By means of using extremely strong magnetic fields (up to 10 T), charged particles of the plasma are confined and heated up. Charged particles are trapped inside the field enough time to collide with other particles before escape. In a linear set up, particles will escape when reaching the edges of the coil that produces the field. Hence, the design twists the magnetic field in a torus shape to confine particles for longer time. Ideally, this approach could work in a steady state way. However, the curvature of the field eventually provoke particles to drift out of the field. The ease with which this kind of machines can be scaled up (improving geometrically the device performance) makes it the most promising branch of research.

1.2.2. Reactor designs

Among the magnetic confinement machine designs proposed, two main ones have been built and studied in depth:

- Tokamak: Its name is the acronym of the Russian original name, which would be translated as "toroidal chamber with magnetic coils". It is the simplest and most developed device nowadays. This kind of machine is a D cross section shape torus. There are toroidal coils that generate the main magnetic field and a central solenoid used to drive currents inside the plasma in order to stabilize it. Nevertheless, such design causes it to operate discontinuously (pulses where current in coils increases). ITER device is an example of this design (see Figure 1.3).

- Stellarator: In the long run, this is the most promising technology for commercial fusion because they allow steady state functionality. This is achieved by twisting the toroidal field with a more complicated mechanical design. However, the reactor complexity compared to Tokamaks have caused it to be one step behind in their development stage. An example of this devices can be seen in Figure 1.2.

1.3. ITER reactor

As mentioned before, ITER is intended to be the first reactor that achieves the ignition condition in plasma (that is, a reaction self sustained without external heating support).

The reactor is going to be a Tokamak device of 6.2 m radius and a 840 m^3 chamber volume. Temperatures in plasma will reach 1.5×10^8 K on pulses of 300 s long. This temperatures are one order of magnitude higher than the Sun core.

1.3.1. Main parts

Figure 1.3 shows the main parts of the device. Their purposes and characteristics are described below according to ITER Organization data [8]:

- The vacuum vessel: It consist in a sealed steel toroidal container. It acts as the first safety barrier (the second is the containment building). Besides being a safety barrier it provides a vacuum environment for the plasma and will provide holding for the blankets and divertor modules. The chamber will have 44 windows though which remote handling, heating and diagnostics systems will access to the plasma. The inner volume of this chamber will be 1600 m^3.

- The magnets: Due to the extremely strong magnetic fields that will hold the plasma (of the order of 10 T), magnets used to produce them must be superconducting ones. Therefore, they would need to be chilled down to temperatures of the order of 4 K. An internal supercritical helium circuit inside the coils will provide this cooling power. Figure 1.4b shows a CAD design of toroidal magnets.

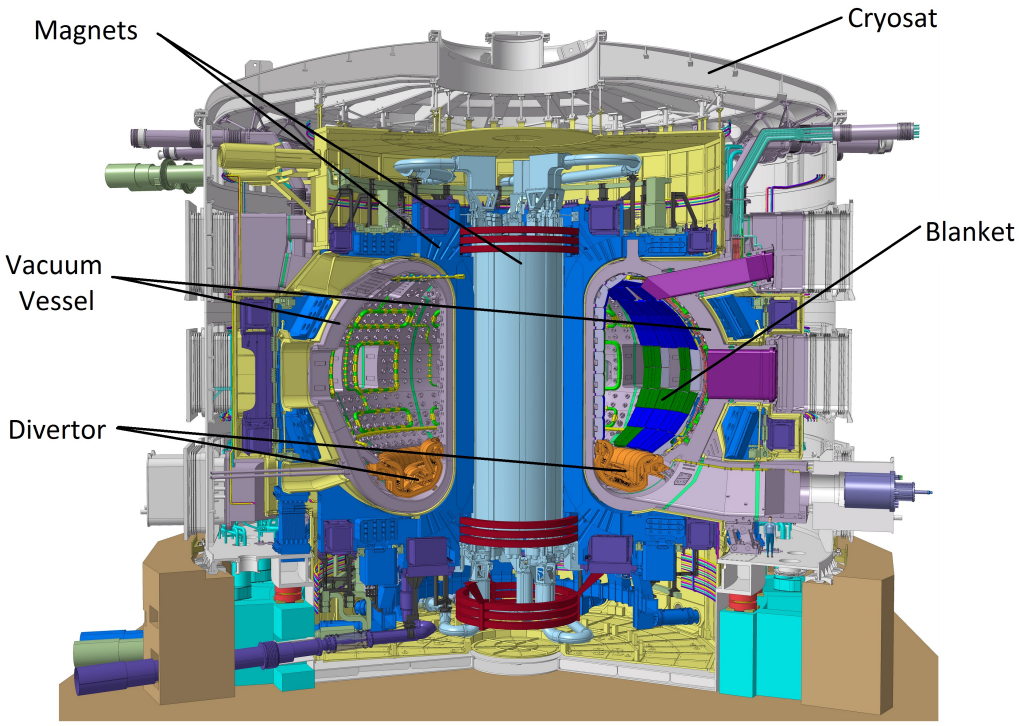

Figure 1.3.: ITER main components. Extracted from [8].

- The blanket: It shields the steel vacuum vessel and external machine components from high-energy neutrons produced during the fusion reaction. Besides, heat and tritium are produced (and then extracted) in here. The blanket will be able to extract more than 736 MW of thermal power. The 600 m^2 surface of blanket will be composed of 1×1.5 m modules. Several designs are considered and will be tested on ITER (more details are described in section 2.3).

- The divertor: This device is needed in order extract the exhaust wasted gas and impurities out of the plasma In addition to this, its characteristic form is designed to control the plasma shape and avoid it to get in contact with the walls. Located at the vessel bottom, it is designed to withstand heat fluxes over it surface higher than 20 $MW\mathrm{m}^2$.

- The cryosat: It surrounds the vacuum vessel and provides insulating in order to warranty an ultra-cool environment for the superconducting magnets. This 16000 m^3 chamber will hold a low pressure of 10^{-4} Pa. Many ancillary elements attached to the reactor will be kept inside, such as the heating and cooling systems, the coils controllers and the diagnostics devices.

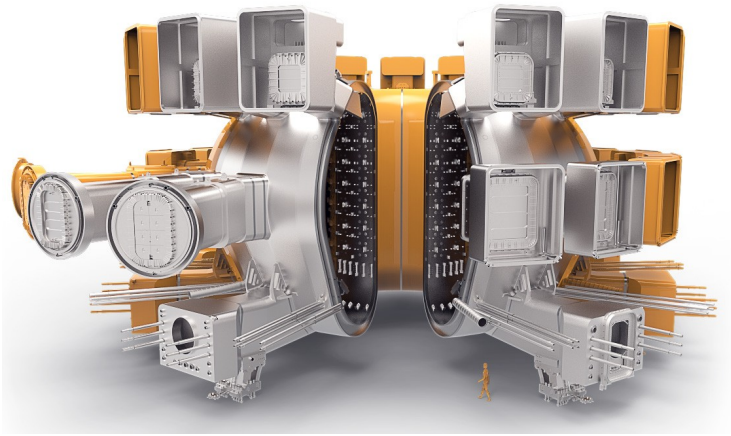

(a) Vacuum vessel.

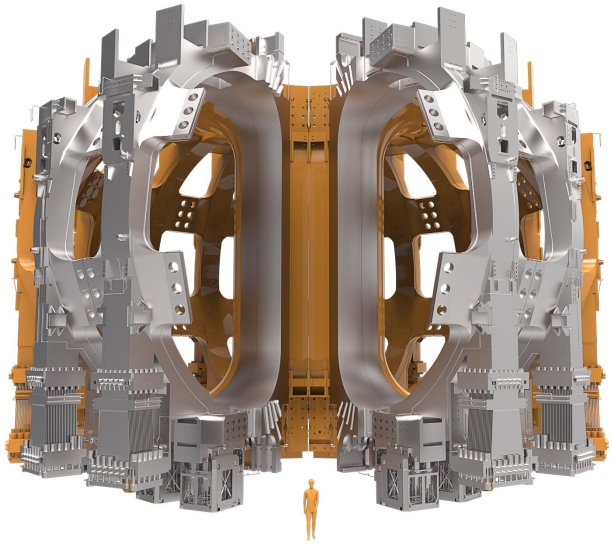

(b) Toroidal magnets.

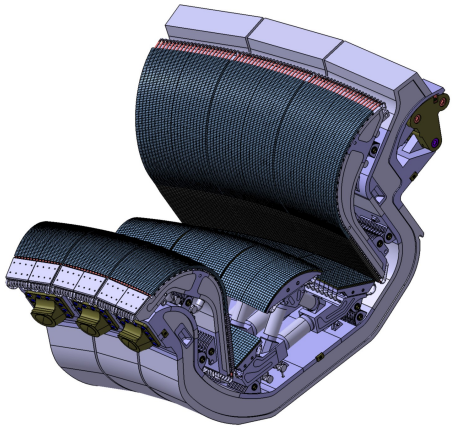

(c) Divertor.

Figure 1.4.: CAD representations of some ITER main parts. Extracted from [8].

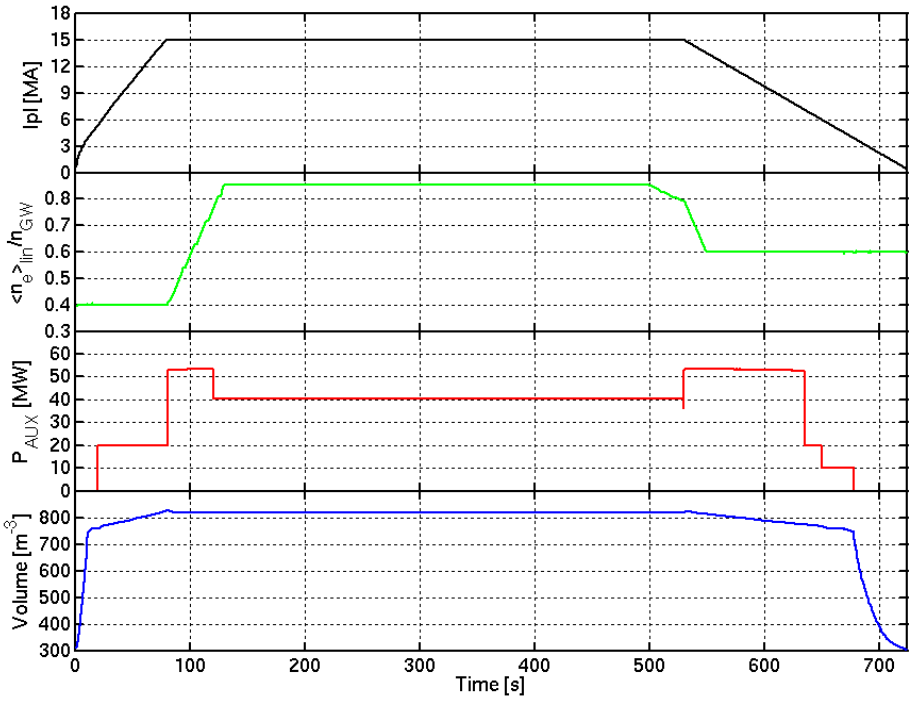

Figure 1.5.: Example of plasma shot designed for ITER operation. Extracted from [9].

1.3.2. Operation

When finally commissioned (forecast for 2020 though such date has been delayed in the past several times), ITER will begin operation following stages. The fist one will test the reactor works as designed and check all the system with hydrogen (protium).

Thereafter, D-D plasma operation will begin. In this stage, all the developed strategies for plasma stability such as fuel pebble injection to avoid instabilities (mainly ELM) will be tested.

Finally, the first D-T plasma is scheduled for 2035. This stage is an important non-return point, since once this test begin, the reactor materials will get activated and the only way to access the reactor chamber will be though the remote handling systems. During phase 2 and 3, pulses of plasma will last up to 300 s. Figure 1.5 shows an example of simulated plasma shots.

1.3.3. Objectives

As an experimental reactor, the aims of ITER are related to demonstrate the feasibility of the reactor. Its main objectives are:

- Reach engineering break-even point, which means to extract more power from the reactions than what is being imputed to heat the plasma. This corresponds to a have a net gain factor (the ratio between energy extracted and supplied to the system) higher than one (indeed, aimed up to $Q = 10$).

- Study and test an operation mode of the reactor in which the plasma can be self heated. This way the reactions could take place with a minimum heating input (only to control de plasma). This technique relies on the fine use of the radiofrequency heating systems. Hence, it would allow to solve one of the biggest drawbacks of Tokamaks, which is their intrinsic discontinuous operation.
- Test durability of plasma facing materials and components designs. Radiation damage to system materials is going to assessed as well.
- Prove the success of all the technologies involved working together. ITER must show how all the complex systems embedded can work and provide real operation feedback for the design of future commercial reactors. In this framework, all the brand new technologies involved in the tritium cycle are of major interest (see next chapter).

2. The Tritium Plant

2.1. Fusion plant fuel cycle

As mentioned before, deuterium-tritium (D-T) is the reaction selected for ITER operation. Deuterium is relatively easily produced from hydrogen isotope separation since it is present in nature with a proportion of 0.015 %. However, tritium is a short-live element (13.5 years of half live) and hence, only traces of it can be found naturally on Earth. This amount is far away of being enough for a fusion reactor needs. Therefore, tritium will be produced in the facility during operation. Though ITER is going to test all this technologies, the scale of its tritium plant will not be enough for the complete supply of tritium that will be consumed. Therefore, according to the experimental label of this reactor, part of the tritium will be brought from outside.

2.1.1. Breeding process

Due to the lack of tritium availability, it is apparent that it needs to be produced continuously at the plant, not only at DEMO but at every future fusion reactor. Henceforth, in order to produce enough tritium for the plant operation, neutron reactions with lithium isotopes are proposed as a suitable source of this fuel.

$$^{1}\mathrm{n} + {}^{6}\mathrm{Li} \rightarrow {}^{4}\mathrm{He} + {}^{3}\mathrm{H} + 4.8\mathrm{MeV} \tag{2.1}$$

$$^{1}\mathrm{n} + {}^{7}\mathrm{Li} + 2.5\mathrm{MeV} \rightarrow {}^{4}\mathrm{He} + {}^{3}\mathrm{H} + {}^{1}\mathrm{n} \tag{2.2}$$

This way, for every D-T reaction in plasma a neutron would be generated. This neutron could be used to break a lithium nucleus according with the previous reactions, producing a new tritium nucleus which would be introduced to the plasma later on in order to produce a new fusion reaction. This is the so called "tritium fuel cycle".

2.1.2. Multiplier process

As it has been seen, the breeding process provides a way to produce the fuel needed. Nevertheless, it is clear that not all the neutrons produced in plasma will induce the desired lithium reaction. Instead, many of them will be absorbed by others materials, or simply escape from the reactor. In this situation, tritium production will not be sustainable in time. Thus, in order to balance this continuous loss of neutrons, a multiplier material needs to be used.

A multiplier is a nuclide in which fast neutrons may induce nuclear reactions resulting in the production of more than one neutron as products. This way, each neutron

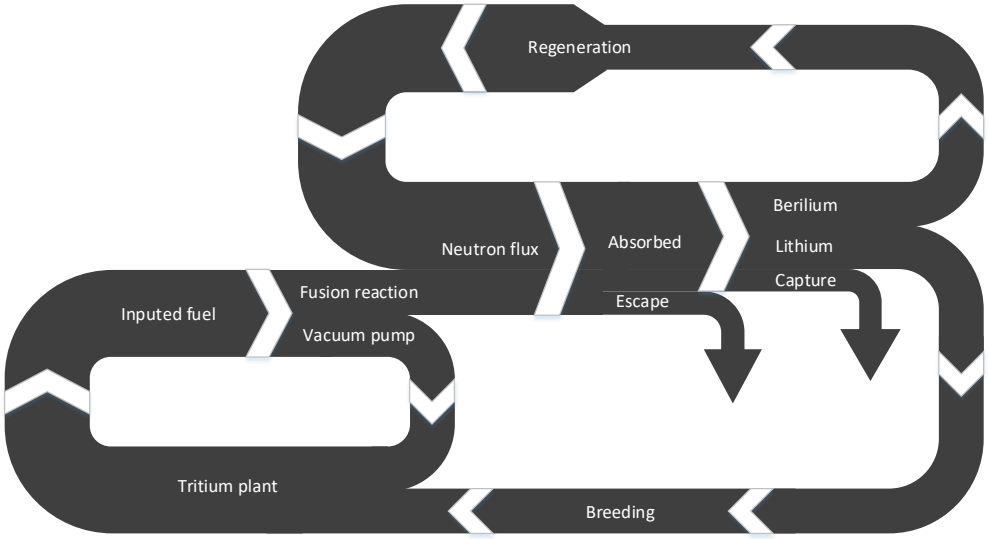

Figure 2.1.: Simplified Sankey diagram of the neutron breeding and multiplication process (neutron-tritium cycle) for a fusion power plant. Fractions derived from each branch are not proportional to reality, just descriptive.

absorbed by the multiplier element will produce more than one neutron as reaction products. Thus, lost neutrons are compensated with the new ones produced in the multiplier lattice.

Among the proposals, beryllium and lead seem to be good candidates. When a beryllium nucleus is hit by a high energy neutron, it splits into two α particles and two new neutrons as shown in expression 2.3.

$$^{1}\mathrm{n} + {}^{9}\mathrm{Be} + 1.8\mathrm{MeV} \rightarrow 2^{4}\mathrm{He} + 2^{1}\mathrm{n} \tag{2.3}$$

On the other hand, lead can also be used as a multiplier and transport fluid at the same time. Thus, it is an interesting candidate as well.

$$^{1}\mathrm{n} + \mathrm{Pb} + 8.0\mathrm{MeV} \rightarrow \mathrm{Pb} + 2^{1}\mathrm{n} \tag{2.4}$$

All the reactions mentioned in this section would take place in the dedicated component called the breeding blanket, which would be deeper explained in section 2.3. A schematic view of the neutron cycle described in this section can be seen in Figure 2.1. Tritium plant details are not shown here and are developed in next section.

2.2. Plant layout

The ITER tritium plant (sketched in a simplified way at Figure 2.2) groups all the systems related with the fuel management. In a fusion power plant, tritium processing

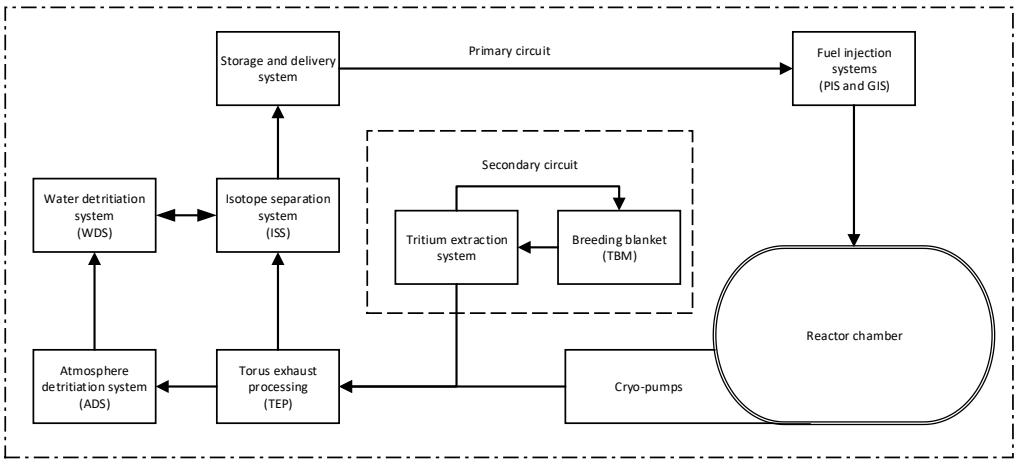

Figure 2.2.: Simplified scheme of a closed loop tritium plant system.

takes place in a closed loop. Nonetheless, since just a few ports of the first wall will be used to test the blankets at ITER (see section 2.3), not enough tritium will be produced in order to make the plant self sustainable. Hence, an external supply will be needed. The plant can be divided into two main circuits:

- Primary: Stored deuterium and tritium are introduced in the plasma in two ways. The main system will inject fuel in gas form inside the chamber. Besides, an auxiliary system will throw small frozen fuel pellets (1 mm diameter) inside the plasma. This technique allows to control plasma density and disruptions, such as ELM. However, just a very low percentage of the introduced fuel will undergo fusion reactions. Therefore, tritiated gas from the exhaust of the reactor vessel ("unburned" at the plasma) need to be processed in this circuit. Such gases are extracted out of the plasma chamber via the divertor and powerful vacuum pumps. Many auxiliary systems are used to process the exhaust, like the isotope separation and the detritiation systems. The main purpose of this system is to minimize the waste and the cost of tritium cycle by recycling it. Besides, its aim also include the deactivation of radioactive effluents.

- Secondary: Here is where new tritium is generated through the reactions mentioned in the previous section (2.1). This way, tritium consumed in the fusion reaction and in the leakages of the plant is compensated. The breeding blanket (TBM) is located in this circuit and is where the tritium production takes place. Tritium breeded is extracted from the TBM and then introduced in the primary circuit. Therefore, although this system is not strictly essential for the tritium plant operation, allows the plant to self-supply its fuel needs.

2.3. The breeding blanket

As mentioned in section 2.1, all the reactions explained before take place in the breeding blanket modules. This component, placed just behind the first wall of the reactor, is also aimed to protect the magnets from high neutron fluxes in there and to cool down the wall (this heat will be used for power generation in future fusion reactions such as DEMO too). Nevertheless, the goal of interest for this work is to proof the viability of self-sufficiency in terms of plant tritium needs of future fusion reactors.

As a key component for fusion technology research, all countries involved in ITER are developing their own blanket designs to be tested in there. European Union is focusing its research in two ideas, which would be tested simultaneously when ITER start running the D-T reactions. Those designs are the Helium cooled Lithium-Lead (HCLL) and the Helium-cooled Pebble Bed (HCPB).

2.3.1. Main objectives of TBS operation

- Tritium breeding: As mentioned in section 2.1.1 tritium is produced in the TBM mainly by inducing reaction 2.1. Therefore, lithium will be present in different forms depending of the TBM design, yet always enriched with the ^{6}Li isotope. Besides, the TBM will use a multiplier material (lead or beryllium depending on the design) in order to compensate the undesired neutron absorptions.

- Tritium removal: Once tritium is produced inside the TBM, it needs to be collected so that it can feed the fusion plasma. Again, the main way to extract the generated tritium depends on the TBM design. Nevertheless, both cases also use the Helium Coolant System as a secondary way of extracting it, since tritium will permeate though the structure towards this system too.

- Heat recovery: TBM is exposed to the extreme temperatures of the plasma. Besides, huge amount of heat is generated inside due to the neutron reactions. Therefore, heat removal is mandatory in order to keep the TBM integrity. It will be achieved thanks to a pressurized helium flow though channels embedded in the main plates of the TBM box.

- Neutron shielding: Like other in-vessel components, TBM have to protect the superconducting magnets, the vacuum vessel and the cryostat from radiation and heat. Although the TBM itself will absorb a fraction of the plasma neutron flux, secondary radiation from the breeding and multiplying process will be generated. Hence, a shield will be placed behind it.

2.3.2. The HCLL TBM

Helium Cooled Lithium Lead is a TBM design where a melted Pb-16Li eutectic alloy is used as breeder, multiplier and transport material at the same time. Tritium will be generated in this fluid bulk and will be extracted from it by the TBS ancillary systems.

Lithium used is enriched up to 90% of the ^{6}Li isotope. The system is cooled down through an helium flow at 80 bar working in the range of temperatures between 300 and 500 °C. An image of the design can be seen in Figure 2.3.

Obviously, simplicity is the main advantage of this system, since the eutectic alloy serves the three main objectives at the same time (cooler, breeder and multiplier). However, the use of lead as fluid may arise many problems, mainly regarding corrosion and solidification.

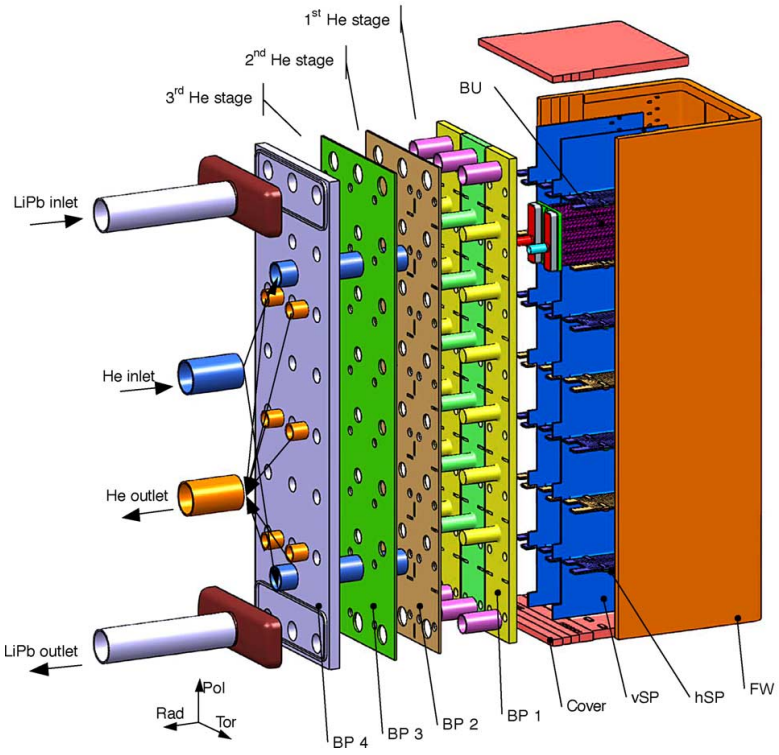

Figure 2.3.: Scheme of an European HCLL-TBM design. Extracted from [10].

2.3.3. The HCPB TBM

Helium Cooled Pebble Bed is a TBM design where a low pressure Helium flow with traces of hydrogen is used to extract tritium while circulating through the Beryllium and ceramic pebble beds. Tritium will be transported under molecular hydrogen and water molecules form. This flow is circulated then towards a specific system designed for tritium extraction. The design of this module can be seen in Figure 2.4.

In the pebble beds ceramics, enriched lithium-6 is present under the form of Li-orthosilicate (Li_4SiO_4) with 30% of ^{6}Li enrichment or Li-metatitanate (Li_2TiO_3) with 60% of ^{6}Li enrichment. Besides, beryllium multiplier pebble beds are also present in order to enhance noticeably the breeding process. For structural material, a reduced activation ferritic-martensitic steel EUROFER-97 has been selected.

The module would be cooled down though an Helium flow at 80 bar working in the range of temperatures between 300 and 500 °C (steel maximum temperature is 550 °C).

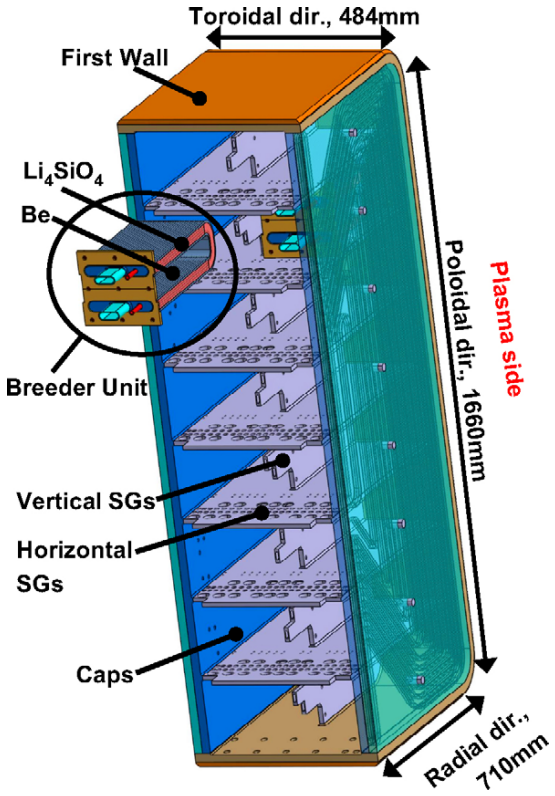

Figure 2.4.: Scheme of an European HCPB-TBM design. Extracted from [11].

2.4. Tritium inventory management

A fusion power plant consists of several systems involved in the tritium processing. Along each one, many chemical forms and physical states of tritium can be found. Therefore, a need of controlling and evaluating the quantities of tritium inventories arises since it directly connects with safety issues.

2.4.1. Monitoring

The capability of tritium monitoring over each fusion plant system is essential as it provides information to assess whether or not normal operation is being carried out in each equipment. Besides, any increase of tritium concentration in secondary confinement may indicate leakages of the primary one and will therefore require attention.

Periodical monitoring during normal operation provides information about the work area safeness. Moreover, it gives an immediate indication of changes in radiological situation. When a worker handles contaminated materials during maintenance activities, the capability of monitoring can provide an immediate warning of unexpected increase in tritium activity.

Additionally, monitoring gives essential radiological protection information regarding activity planning, for instance, maximum staying time in the area of interest and required protective measures.

2.4.2. Inventory control

Present estimation of the total tritium inventory in a fusion power plant is nearly 1 kg into the vacuum vessel, fuel cycle system and the hot cell. Besides, 15 kg are expected to be kept into the long-term storage. However ITER values are lower, and are estimated as shows Table 2.1. Following the ALARA principle, in order to keep the annual radiation exposure level of the public at the ITER site boundary under the ICRP recommended value [12], the maximum tritium annual leakage from the tokamak building must be kept below 7 g, assuming 90% or more recovery efficiency of the detritiation system. Besides, according to the same document, public radiation exposure values must be lower than the limit set to 1 $mSv/year$.

Table 2.1.: Summary of tritium inventories (maximum instantaneous values; not all simultaneous) allowed for ITER design. Extracted from [13].

System	Subsystem	T inventory (g)
In-vessel	Mobilizable (dust, deposited, PFC, etc)	330[a]
	Cryopumps open to vacuum vessel	120
	Subtotal	450[b]
Fuel cycle	Pellet fuel (PIS)	45
	Gas fuel (GIS)	10
	Mechanical vacuum pups (MVP)	20
	Torus exhaust processing (TEP)	30
	Isotope separation system (ISS)	220
	Test blanket module (TBM)	~ 15
	Water detritiatation (WDS)	~ 10
	Atmosphere detritiatation (ADS)	~ 1
	Gas analysis (ANS)	~ 2
	Subtotal	~ 353 (450[b])
Storage	Long term storage	900
Other	Hot cell and waste treatment	200
	Tritium recovery and waste storage	50
	Subtotal	250
Total		~ 1953 (< 3000[c])

[a] Excluding T bred in beryllium: 125 g (immobile for $T < 600\ ^\circ C$).

[b] Project administrative guideline (less stringent assessment values to account for uncertainties have been established).

[c] The total site inventory will be limited to 3 kg.

3. Fundamentals of Tritium Transport

3.1. Introduction

Once the importance of the tritium control and management has been discussed, next step is to understand how it will transport, and eventually escape out of the system. In essence, this problem is a scalar transport one. Hence, many synergies come up with the heat transfer field. As matter of fact, many non-dimensional numbers used for temperature transport have its mass transfer analogous. Nevertheless, some important differences arise as well. Here, tritium is transported both into fluids (where, for the case of gases, it would adopt the form of di-atomic molecules) and into solid (where is going to be present as single atoms). This issue will induce non-linearities at the interfaces of both media as will be seen in the following sections.

Additionally, this chapter will discuss as well some other phenomena which could be found in tritium plants. This is the use of chemical hydrogen absorbers-desorbers (getters) used to purify TBM cooling systems and concentrate the produced tritium in order to recycle it.

3.2. Transport mechanisms

As it has been commented before, tritium concentration transport all along the systems will always be mass conservative. Therefore, equation 3.1 will be followed as any other scalar transport expression, where D is the diffusivity of the molecule or atom transported (depending if the bulk media is a gas or solid), ρ is the density of the bulk media and S any volumetric source.

$$\frac{\delta C}{\delta t}\rho = -u\rho \cdot \nabla C + \nabla (D\nabla C) + S \tag{3.1}$$

Henceforth, from equation 3.1 three main terms have to be considered, apart from the boundary conditions which will be explained in next sections.

3.2.1. Advection

The first term of the left side of equation 3.1 is the so called advection term. It represents the concentration variation in the control volume due to the fluid motion dragging within its bulk for the studied transported specie. This term is completely similar to its temperature analogous.

Since this term is caused by the bulk fluid movement, this term is obviously null when the transport is performed inside a solid lattice.

3.2.2. Diffusion

The second term of the right side of equation 3.1 is the diffusion term. According to Fick's law, a difference in concentration of some specie drives a flux of such specie from high concentrations to lower ones. The magnitude of this flux is proportional to the difference of concentration and the diffusivity coefficient D of this specie though the material. In solids, this parameter is highly temperature dependent through an Arrhenius relationship:

$$D(T) = D^* e^{-E_D/RT} \qquad [m^2/s] \tag{3.2}$$

where D^* is a pre-exponential factor, E_D the activation energy of the diffusion process, R the ideal gas constant and T the absolute temperature expressed in Kelvin.

This term is usually negligible against the advection one. However, it is the only way that a solid can transport mass though it. Hence, it becomes quite important in solid transport. Besides, diffusivity coefficients are quite sensitive to temperature changes, hence, a system will behave very different in what concerns diffusion depending on the temperature range where it works.

3.2.3. Sources

The last term of the equation is the source term. It represents the creation of the studied specie within the control volume though other mechanism apart from transport. A good example is the tritium generated inside the breeders of ITER blanket modules though a nuclear reaction as commented in section 2.1.1. Nevertheless, for the scope of this work, no further need of considering this terms will arise.

3.3. Diffusive phenomena

As commented before, tritium and all the isotopes of hydrogen are differently transported depending on the state of the bulk where they are. In solid, the specie is diffused in atomic form whereas in gases is as molecules. This leads to the need of understanding the mechanisms that take place in the boundaries of both media.

3.3.1. Solubility

When a gas is in contact with a solid or liquid phase, some molecules of such gas will migrate from it until an equilibrium is reached. Solubility is defined as the analytical composition of a saturated solution expressed as a proportion of a designated solute in a defined solvent. This is, the maximum amount of solute that a solvent can absorb in contact with this solute gas. Therefore, solubility is the equilibrium constant K_s of the absorption-desorption process. Hence, knowing the solubility of a material will give an idea of the quantities of studied solute that is expected to be in the solvent. Alike diffusion

coefficient, this equilibrium constant is highly temperature dependent as well. Thus, its value can be expressed trough an Arrhenius relationship too:

$$K_s(T) = K_s^* e^{-E_s/RT} \qquad [mol/m^3 Pa^{1/2}] \tag{3.3}$$

being K_s^* a pre-exponential factor, E_D the activation energy of the diffusion process, R the ideal gas constant and T the absolute temperature expressed in Kelvin.

3.3.2. Permeability

The penetration of a substance through a solid is called permeability, normally represented by ϕ $[mol/msPa]$. Usually, when performing experiments, it is easier to measure a permeation ratio of the studied specie though a material than determining other transport parameters. Thus, it is common to find this data in bibliography since is very useful to compute indirectly other properties (see section 3.5).

3.3.3. Sievert's law

Sievert's law is a rule to predict the solubility of gases in metals. The law states that the solubility of a diatomic gas (such as hydrogen isotopes molecules) in metal is proportional to the square root of the partial pressure of the gas in thermodynamic equilibrium as shows expression 3.4.

$$C = K_s \sqrt{p} \tag{3.4}$$

where C represents the solubility (concentration) in the metal lattice and K_s is the Sievert's proportionality constant. This parameter is nothing but the equilibrium constant of the dissociation-recombination reaction of the gas molecule. For the case of hydrogen:

$$H_2 \text{ (molecular gas)} \rightleftharpoons 2H \text{ (dissolved atoms)} \tag{3.5}$$

3.3.4. Trapping

When studding diffusive phenomena, trapping should be considered. This effects are related with the hydrogen atoms that get strongly linked to specific centres (traps such as grain boundaries, dislocations and so). These hydrogen atoms are henceforth absorb by the metal lattice.

This effects leads to an increment in the effective hydrogen inventory absorbed (the Sievert's constant) and in an effective decrement in the material diffusivity. Nevertheless, for the scope of the work, this phenomena is considered to be embedded into each of the experimental properties of the material.

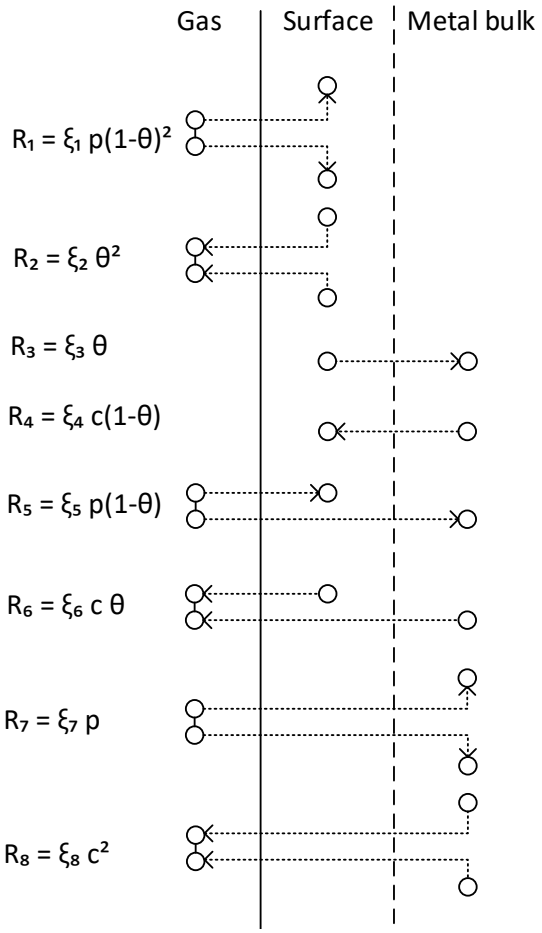

Figure 3.1.: Summary of all the possible phenomena over a metallic surface. Originally from [14].

3.4. Superficial phenomena

It has been noticed that, sometimes hydrogen transport though solid metals is limited by superficial regimes. This conditions usually involve low gas pressures and superficial state of the metal, such as level of oxidation and roughness. Theoretically, all the likely processes that take place in the surface layer of a metal are described in Figure 3.1. Each process has its own phenomenological reaction rate constant (ξ) and are dependant of the superficial coverage factor (θ). This factor is defined in expression 3.6 as the ratio between the number of superficial absorption holes already occupied by hydrogen atoms (N_Q) and the total number of holes (N_{tot}).

$$\theta = \frac{N_Q}{N_{tot}} \tag{3.6}$$

3.4.1. Dissociation-Recombination kinetics

However, in practice, processes (5), (6) (7) and (8) are only relevant when the coverage factor (θ) is high. On the other hand, usually this coverage factor is proportional to the hydrogen concentration in the surface and, therefore, processes (3) and (4) balance each other [15]. Hence, the relevant processes that remain are dissociation (1) and recombination (2). As it has been discussing, the gas-metal interactions in boundary conditions of the system will be driven by the kinetics of the dissociation-recombination reaction. Therefore, the flux over this interface could be written as expression 3.7 shows.

$$\frac{\partial C_{Q_2}}{\partial t} = J_{Q_2} = k_d R T p_{Q_2} - k_r (C_Q)^2 \tag{3.7}$$

where Q sub-index denotes all hydrogen species, k_r is the recombination kinetic coefficient and k_d the dissociation kinetic coefficient. Note that those factor intrinsically include the superficial characteristic of the material such as its roughness.

3.5. Useful relations

As it will be seen in section 3.7, tritium transport parameter data are rare due to the obvious inconveniences of experimenting with radioactive isotopes. Nevertheless, it is possible to predict those parameters by extrapolating hydrogen and deuterium results by following some useful relation:

- Graham's law [16] is an empiric relationship which stands that the rate of diffusion of a gas is inversely proportional to the square root of the mass (A) of its particles. This formula can be written as:

$$\frac{D_1}{D_2} = \sqrt{\frac{A_2}{A_1}} \tag{3.8}$$

- According to Richardson's law [17], the ratio between the permeability of material and its diffusivity is the equilibrium constant of the process, this is, the solubility:

$$K_s = \frac{\Phi}{D} \tag{3.9}$$

  Therefore, from relation 3.9 it can be easily deduced that permeability also follows an Arrhenius dependence with temperature:

$$\Phi(T) = K_s(T) D(T) = D^* K_s^* e^{-(E_D + E_s)/RT} = \Phi^* e^{-(E_\Phi)/RT} \tag{3.10}$$

- Assuming a state of the system where equilibrium conditions have been reached, total flux would be null and equation 3.7 could be rearranged as a function of the Sievert's proportionality constant using its definition (expression 3.4). This way

one kinetic coefficient (either dissociation or recombination) can be determined indirectly if the other is known.

$$K_s = \sqrt{\frac{k_d}{k_r}} \tag{3.11}$$

3.6. Hydrogen capture

As it has been seen in previous chapter, many systems connected one way or another to the blanket will collect traces of tritium. In order to reuse this tritium back to the reactor, it needs to be concentrated and extracted from those systems. In order to do so, solid storage of hydrogen techniques are used.

The main idea is to put in contact a metal hydride with a gas containing the hydrogen traces (including tritium). At room temperature the absorption processes takes place and hydrogen is cumulated into the hydrides. Then, when the metal is saturated, another stream flow can collect hydrogen that is released from the metal by putting it at high temperatures ($\sim$ 400 °C). Of course, that "purge" flow would have a higher hydrogen concentration, ideal to recycle its tritium content back to the fusion chamber.

3.6.1. Reaction

Hydrogen absorption takes place by means of two different mechanisms. On the one hand, atomic hydrogen can be stored directly into the metal lattice (thanks to its atomic small size) according to the phenomenology seen in section 3.4.1. On the other hand, the hydration reaction can take place changing the normal phase (so called α) into the hydrated phase (β). In this case, ZrCo alloy is used, although other candidates could be suitable too, such us Uranium. The absorption-desorption reaction is the following:

$$ZrCo + \frac{3}{2}H_2 \rightleftharpoons ZrCoH_3 \tag{3.12}$$

where ZrCo is the α-phase and $ZrCoH_3$ is the β-phase. As commented in previous section, at room temperature, equilibrium is displaced to the right side (and the absorption reaction takes place). However, for high temperatures (over 400 °C) the equilibrium is shifted to the left side which leads to the desorption reaction. Note that there is no distinction between hydrogen isotopes since all of them are considered to behave identically chemically speaking.

Nevertheless, there is also an irreversible reaction that could take place simultaneously (and that is tried to be avoided):

$$2\ ZrCo + H_2 \rightarrow ZrH_2 + ZrCo_2 \tag{3.13}$$

3.6.2. PTC equilibrium curves

Pressure Composition Temperature (PCT) curves also called Pressure Composition Isotherm (PCI) curves can be a source of information of thermodynamic solid hydrides properties. A typical PTC of a reversible hydride is shown in Figure 3.2. By measuring the hydrogen pressure and its corresponding changes in hydrogen concentration into the metal at a given temperature, PCT curves can be constructed. A flat plateau is expected to be obtained where both phases co-exist. Nevertheless, most practical hydrides do not show perfectly flat plateau or zero hysteresis.

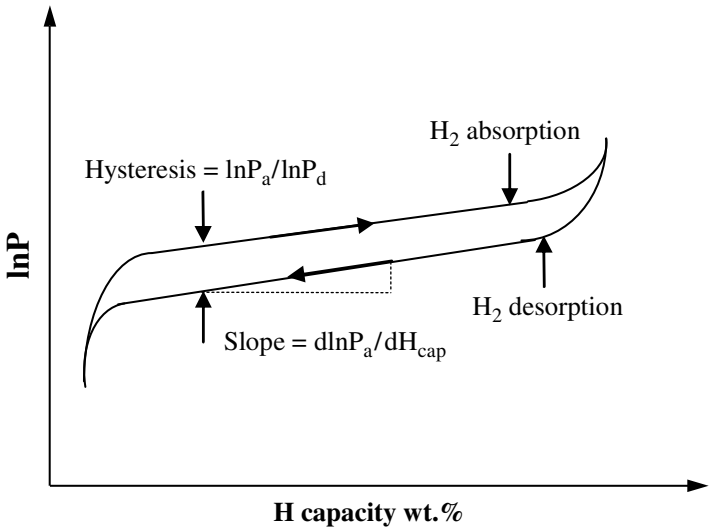

Figure 3.2.: Schematic isothermal pressure–composition hysteresis loop.

3.6.3. Vant Hoff curve

The reversible reactions (expression 3.12) will take place into the plateau of the equilibrium curve, where small changes of pressure lead to big changes in hydrogen content. The plateau region is limited between a minimum and a maximum concentration (C_{min} and C_{max}) and is where storage system will operate. Figure 3.3 shows a generic curve that could be modelled using expression 3.14.

$$\ln\left(\frac{p_{eq}}{p_0}\right) = \frac{\Delta H}{RT} - \frac{\Delta S}{R} \pm \frac{1}{2}\frac{\ln(p^a_{eq})}{\ln(p^d_{eq})} + (C - C_0)\frac{\partial \ln\left(\frac{p_{eq}}{p_0}\right)}{\partial C} \tag{3.14}$$

where p_0 is the reference pressure (usually 1 atm), ΔH and ΔS enthalpy and entropy changes of the hydring-dehydring reaction, the third term is a corrector for the curve hysteresis if ΔH and ΔS do not change depending whether there is an absorption or a desorption process and the last one is the corrector for the curve slope with hydrogen fraction, calculated at the reference concentration C_0.

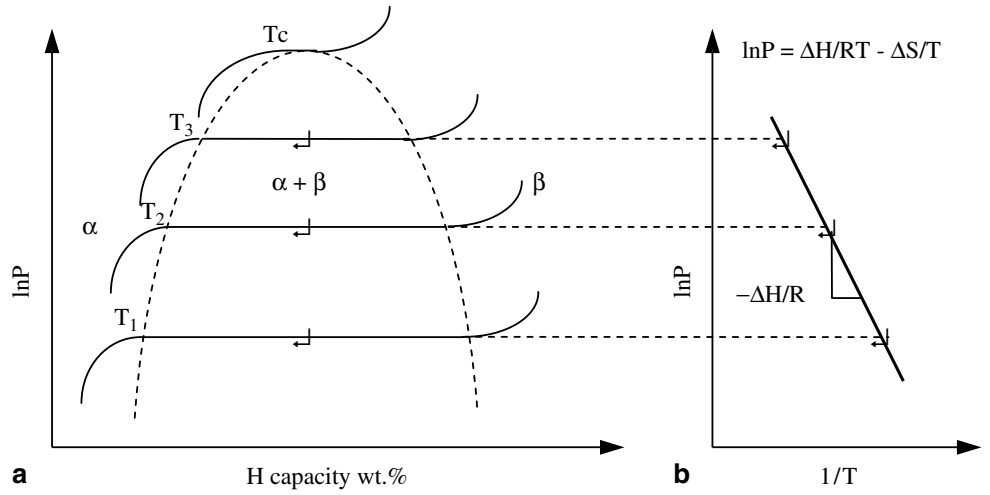

Figure 3.3.: Pressure Concentration Temperature plot (left) and Van't Hoff plot (right).

3.6.4. Hydride kinetics

When hydrogen concentration in metal lattice is lower than the beginning of the plateau ($C < C_{min}$), hydrogen is stored among the α-phase metal structure and Sievert's law can be used. Henceforth, according to Ostapov [18], the flux is the result of a dynamic equilibrium between the dissociation ratio (k_d) and the recombination ratio (k_r) as shown in equation 3.7.

On the other hand, when β-phase begin to appear (the hydrogen fraction is above the beginning of the plateau, i.e. $C > C_{min}$) the hydrogen storage takes place simultaneously in both α and β phases. This way, the variation of hydrogen concentration depends on both the proximity with the equilibrium pressure and the corresponding limiting concentrations. According to several authors [19, 20, 21, 22] the flux can be expressed as shows expression 3.15.

$$\frac{\partial C}{\partial t} = \begin{cases} J_a = k_a e^{-E_a/RT} \ln\left(\frac{p}{p_{eq}}\right)(C_{max} - C) & p > p_{eq}^a \\ 0 & p_{eq}^d < p < p_{eq}^a \\ J_{de} = k_{de} e^{-E_{de}/RT}\left(\frac{p_{eq}-p}{p_{eq}}\right)(C - C_{min}) & p < p_{eq}^d \end{cases} \tag{3.15}$$

where $p = RTC_{Q_2 tot}$, p_{eq} is calculated with the Van't Hoff's equilibrium pressure expression and $E_{a/d}$ are the activation energies of the absorption desorption processes that makes the kinetic constants (k_a and k_{de}) dependent of the temperature.

Note that since p_{eq}^a is always higher than p_{eq}^d, there is a "dead band" between both pressures in which the system does not release or absorb any hydrogen to or from the gas. As commented before, during normal operation the absorption will take place at room temperature (the process is exothermic) and the desorption at higher temperatures (since this process is endothermic).

It is also very important to note that, C_{Qtot} and p stands for the sum of all the hydrogen isotopes. This is because, differently from α-phase absorption, where each individual hydrogen isotope atom stored is not affected by its neighbourhoods, in β-phase the lattice can get saturated. Therefore, absorption and desorption rates depend on the overall hydride saturation state, regardless the isotopic composition (assuming all hydrogen isotopes have identical chemical behaviour).

$$C_{Qtot} = C_H + C_T \tag{3.16}$$

$$p = RTC_{Q_2tot} = RT(C_{H_2} + C_{T_2} + C_{HT}) \tag{3.17}$$

3.7. State of the art revision

One of the main issues in order to get precise enough models in hydrogen isotopes transport is to determine the transport parameters. Some of them such as the diffusivity or the permeability for protium and deuterium are relatively easily measured and, therefore, there is enough bibliography available. However, when it comes to tritium, a shortage of data arises due to obvious difficulties at experimenting with this radioactive isotope. Hopefully, some of them can be estimated using the relations discussed in section 3.5.

Besides, the main problem lies on superficial parameters over which the model relies on (see section 3.4.1). Few authors have determined such values in the most common material (steels). Moreover, data found are very disperse. This is caused by the huge variability of such parameters with the superficial conditions at which the sample was tested.

Henceforth, this section summarizes the effort made compiling current available data for each material of interest within the scope of this work. Table 3.1 shows the values of the Arrhenius coefficient data for diffusion, permeation and Sievert's constant for different hydrogen isotopes. On the other hand Table 3.2 shows superficial kinetic Arrhenius coefficient (dissociation and recombination) for different hydrogen isotopes as well. Note that missing values can be estimated using relations discussed in section 3.5.

Table 3.1.: Summary table of the transport parameter coefficient data for the main materials of interest. Diffusivities (D^*) is expressed in $[m^2/s]$, Sievert's constants (K_s^*) in $[mol/m^3Pa^{1/2}]$, permeabilities (Φ^*) in $[mol/msPa^{1/2}]$ and all the activation energies in $[kJ/mol]$. Temperature ranges are expressed in [K].

Material	Q	D^*	E_D	K_s^*	E_s	Φ^*	E_Φ	Range	Ref.
SS 304	H	$1.22 \cdot 10^{-6}$	54.85	—	—	$4.80 \cdot 10^{-7}$	66.40	645-945	[23]
SS 316	H	$7.30 \cdot 10^{-7}$	52.35	—	—	$8.10 \cdot 10^{-7}$	68.06	502-863	[24]
	H	$1.24 \cdot 10^{-6}$	55.10	0.42	13.8	$5.25 \cdot 10^{-7}$	68.90	623-1123	[25]
	D	$1.38 \cdot 10^{-6}$	57.50	0.33	13.7	$4.56 \cdot 10^{-7}$	71.20		
	T	$4.20 \cdot 10^{-6}$	64.00	0.19	10.2	—	—	603-853	[26]
MANET	D	$1.01 \cdot 10^{-7}$	13.21	0.27	26.7	$4.20 \cdot 10^{-8}$	42.38	373-743	[27]
α-Fe	H	$3.87 \cdot 10^{-8}$	4.5	0.51	27.0	—	—	573-873	[28]
75Pd-25Ag	H	$3.07 \cdot 10^{-7}$	25.90	0.182	19.6	$5.58 \cdot 10^{-8}$	6.30	323-773	[29]
	D	$1.87 \cdot 10^{-7}$	24.69	0.184	18.5	$3.43 \cdot 10^{-8}$	6.16		
Optifer-IV	H	$5.49 \cdot 10^{-8}$	10.6	0.328	29.0	$1.80 \cdot 10^{-8}$	39.6	423-892	[30]
	D	$4.61 \cdot 10^{-8}$	11.3	0.325	29.0	$1.50 \cdot 10^{-8}$	40.3		
	T	$4.17 \cdot 10^{-8}$	12.0	0.271	27.9	$1.13 \cdot 10^{-8}$	39.9		
ODS-Eurofer	H	$1.33 \cdot 10^{-6}$	30.4	0.009	4.2	$1.22 \cdot 10^{-8}$	34.6	420-676	[31]
Eurofer-97	H	$4.57 \cdot 10^{-7}$	22.3	0.023	15.1	$1.05 \cdot 10^{-8}$	37.4	373-723	[32]
	D	$1.50 \cdot 10^{-7}$	14.5	0.102	23.8	$1.53 \cdot 10^{-8}$	38.3		

Table 3.2.: Summary table of the superficial kinetic parameter data for the main materials of interest. Dissociation rates (K_d^*) is expressed in $[mol/m^2sPa]$ and recombination rates (K_r^*) in $[m^4/mols]$. Temperature ranges are expressed in [K].

Material	Q	K_d^*	E_d	K_r^*	E_r	Range	Ref.
SS 304	H	$1.13 \cdot 10^{-2}$	77.45	—	—	645-945	[23]
SS 316	H	—	—	$1.93 \cdot 10^{-3}$	55.96	401-1055	[33]
	T	—	—	$6.57 \cdot 10^{-5}$	20.19	293-723	[34]
	T	$1.60 \cdot 10^{-3}$	48.2	$6.80 \cdot 10^{-3}$	20.19	420-620	[35]
MANET	D	$4.9 \cdot 10^{-7}$	58.38	$6.7 \cdot 10^{-6}$	5.04	373-743	[36]
75Pd-25Ag	H	$1.7 \cdot 10^{-2}$	26.29	0.51	65.49	323-773	[29]
	D	$1.3 \cdot 10^{-2}$	24.78	0.39	61.84		
OPTIFER-IV	D	$3.00 \cdot 10^{-8}$	29.23	$2.84 \cdot 10^{-7}$	28.68	523-723	[37]

4. Predictive Transport Model

4.1. Description

As commented in the introduction, predictive tools that are studied in this project are based on very detailed predictive computations. Such outcomes are essential both to understand the physics behind each studied system and to "coach" the developed predictive functions.

The code model presented in this chapter is a tool originally developed by Batet [38] for a single pipe which capabilities has been extended and generalized for a piping system. Thus, the code has been converted in a post-processing tool for a fluid dynamic solution, where hydrogen isotopes can be transported according to profiles of mass flow, density and temperature of the fluid dynamic system. Figure 4.1 shows the proposed work flow for this code.

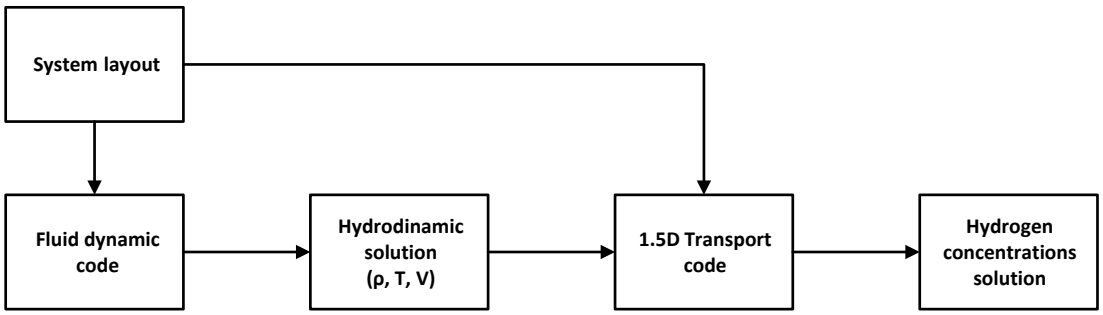

Figure 4.1.: Proposed work flow for the transport code.

4.2. Pipes

In any large scale facility, as the case of tritium plant, piping systems have several kilometres long. Regarding tritium permeation, this stems from the main source of losses, since this part of the system has the largest surface to volume ratio of the plant.

4.2.1. Approach

In order to solve the hydrogen transport trough the pipe, equation 3.1 is solved by discretizing it and setting the appropriate boundary conditions. In this case Figure 4.2 shows the scheme followed.

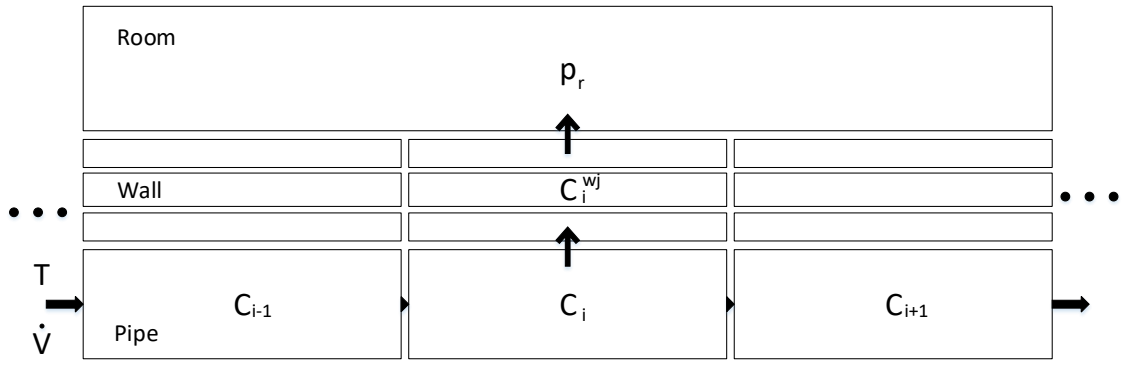

Figure 4.2.: Pipe discretization scheme.

4.2.2. Balances

Helium gas

The discretized expression derived from equation 3.1 for the control volume i is expression 4.1. There is advection and diffusion to and from the previous and the following control volume interfaces. Besides, fluxes are imposed over the inner wall of the pipe. However, there is no source term. As it will be shown in detail in section 4.5.1, upwind scheme is followed.

$$\frac{dC_{Q_2,i}}{dt} = D_{Q_2}\left(\frac{C_{Q_2,i-1} - C_{Q_2,i}}{\Delta x}\right) - D_{Q_2}\left(\frac{C_{Q_2,i} - C_{Q_2,i+1}}{\Delta x}\right) + \\ + \frac{\nu_{i-1}C_{Q_2,i-1} - \nu_i C_{Q_2,i}}{\Delta x} - \frac{2}{r_{in}}J^{in}_{Q_2,i} \tag{4.1}$$

Wall inner surface

Fluxes though the inner pipe wall surface $J^{in}_{Q_2,i}$ imposed in the gas balance are controlled by superficial kinetics described by expression 3.7 (dissociation and recombination). However, for the HT case, recombination process depends both on H and T concentrations over the surface and the expression yields:

$$J^{in}_{HT,i} = k_{d,HT}RTC_{HT,i} - k_{r,HT}C^w_{H,i}C^w_{T,i} \tag{4.2}$$

Then, those fluxes are also equal to the diffusion rate between the surface and the internal wall layer concentrations:

$$J^{in}_{Q} = 2J^{in}_{Q_2} + J^{in}_{HT} = \frac{D_Q}{\Delta r/2}\left(C^w_{Q,i} - C^1_{Q,i}\right) \tag{4.3}$$

where Δr is the discretized radial wall distance between layers. Note how surface concentrations $C^w_{Q,i}$ is a value not linked to any control volume, therefore, it has no time derivative term (no concentration inertia).

Internal wall diffusion

Inside the wall, were the pipe wall divided in several layers, equation 3.1 would be used again. Nevertheless, in this case there is no fluid movement so advection term is null and again, there are no volumetric sources. Additionally, it is important to mention no diffusion has been considered longitudinally. Hence, only radial flux is computed.

$$\left(r_{in} + \left(j - \frac{1}{2}\right)\Delta r\right)\Delta r\frac{dC_{Q,i}}{dt} = \tag{4.4}$$
$$= \frac{(r_{in} + (j-1))\,\Delta r D_Q}{\Delta r}\left(C^w_{Q,i} - C^1_{Q,i}\right) - \frac{(r_{in} + j\Delta r)D_Q}{\Delta r}\left(C^1_{Q,i} - C^2_{Q,i}\right)$$

Wall outer surface

Over the outer wall surface, expression 3.7 is considered too, like the inner one. In the case of HT molecules, the balance yields:

$$J^{out}_{HT,i} = k_{r,HT}C^w_{H,i}C^w_{T,i} - k_{d,HT}p_{r,HT} \tag{4.5}$$

being p_{r,Q_2} the partial pressure of each molecule specie in the room (volume) where the pipe is located.

4.3. Getter pebble bed

As it has been seen in chapter 2, there are many systems in the tritium plant which aim to collect and purify the cooling flows of the different blanket designs. The great majority of such systems are fluidized pebble beds made of a hydrogen absorbent like ZrCo (see section 3.6.1). Therefore, it has been considered interesting to study a possible implementation of such system into the predictive code. Nevertheless, this module has not been validated yet and further improvements in future may be introduced in order to reproduce reality better.

4.3.1. Approach

The way this system is modelled is similar to a pipe with a cross section equal to the free area that pebbles left in between. Such area is a function of the pebble density (ρ_p) and the reactor diameter (r_i), as shows equation 4.6.

$$S_{getter} = (1 - \rho_p)\pi r_i^2 \tag{4.6}$$

Hence, same discretization strategy is applied as for the pipe. However, now there is another boundary condition, witch are the pebble surface. Such boundary is going to be modelled following the theory discussed in section 3.6.4.

4.3.2. Balances

There are some similarities among this discretization and the one performed over the pipe. For instance, wall fluxes are modelled in the exact same way. Hence, is not necessary to rewrite them. Hereafter, the additional or different balances are presented.

Helium gas

As commented before, same equation as the pipe balance is derived from expression 3.1. However, flux to and from the pebbles is added.

$$V_i \frac{dC_{Q_2,i}}{dt} = V_i \left(D_{Q_2} \left(\frac{C_{Q_2,i-1} - C_{Q_2,i}}{\Delta x} \right) - D_{Q_2} \left(\frac{C_{Q_2,i} - C_{Q_2,i+1}}{\Delta x} \right) \right) + \\ + \dot{V} \frac{\nu_{i-1} C_{Q_2,i-1} - \nu_i C_{Q_2,i}}{\Delta x} - A^w J^w_{Q_2,i} - A^p J^p_{Q_2,i} \tag{4.7}$$

where $J^p_{Q_2,i}$ needs to be selected from the two available mechanisms depending on the pebble concentration, as commented in section 3.6.4.

Hence, α mechanism will be the regular inter-lattice surface kinetics described by expression 3.7 when concentration in the hydride lattice is lower than a threshold. On the other hand when hydrogen concentration in pebbles is higher than this threshold analysed $\alpha + \beta$ will include the absorption/desorption reactions of expression 3.15

$$J^p_{Q_2,i} = \begin{cases} \left(\frac{dC_{Q_2}}{dt} \right)_\alpha & \text{if} \quad C^{sp}_{Q,i} < C_{min} \\ \left(\frac{dC_{Q_2 tot}}{dt} \right)_{\alpha+\beta} f_{Q_2} & \text{if} \quad C^{sp}_{Q,i} > C_{min} \end{cases} \tag{4.8}$$

Note that $C_{Q_2,tot}$ stands for the sum of all hydrogen isotopes, since it is assumed their chemical kinetics are similar. Hence, isotopic fractions are defined (equations 4.9 to 4.10) in order to determinate the amounts of hydrogen and tritium absobered and desorbed in the pebble hydride.

$$J_H = \begin{cases} J_a f^a_H = J_a \left[\frac{C_{H_2} + \frac{1}{2} C_{HT}}{C_{H_2} + C_{T_2} + C_{HT}} \right] & \text{if} \quad p^a_{eq} < p \\ 0 & \text{if} \quad p^d_{eq} < p < p^a_{eq} \\ J_{de} f^{de}_H = J_{de} \left[\frac{C_H}{C_H + C_T} \right] & \text{if} \quad p^d_{eq} > p \end{cases} \tag{4.9}$$

$$J_T = \begin{cases} J_a f^a_T = J_a \left[\frac{C_{T_2} + \frac{1}{2} C_{HT}}{C_{H_2} + C_{T_2} + C_{HT}} \right] & \text{if} \quad p^a_{eq} < p \\ 0 & \text{if} \quad p^d_{eq} < p < p^a_{eq} \\ J_{de} f^{de}_T \left[\frac{C_T}{C_H + C_T} \right] & \text{if} \quad p^d_{eq} > p \end{cases} \tag{4.10}$$

Though these proportional factors could not be completely accurate, at least they give a good approximation of the fraction produced for each specie. Besides, they assure

molecular and atomic fluxes are linear combination of the others, that is, mass is conserved. Therefore, it is always ensured that:

$$\begin{cases} J_H = 2J_{H_2} + J_{HT} \\ J_T = 2J_{T_2} + J_{HT} \end{cases} \tag{4.11}$$

Hence, molecular fraction factors can be defined as follows:

$$J_{H_2} = \begin{cases} J_a f^a_{H_2} = J_a \frac{1}{2} \left[\frac{C_{H_2}}{C_{H_2}+C_{T_2}+C_{HT}} \right] & \text{if} \quad p^a_{eq} < p \\ 0 & \text{if} \quad p^d_{eq} < p < p^a_{eq} \\ J_{de} f^{de}_{H_2} = J_{de} \frac{1}{2} \left[\frac{C_H^2}{(C_H+C_T)^2} \right] & \text{if} \quad p^d_{eq} > p \end{cases} \tag{4.12}$$

$$J_{T_2} = \begin{cases} J_a f^a_{T_2} = J_a \frac{1}{2} \left[\frac{C_{T_2}}{C_{H_2}+C_{T_2}+C_{HT}} \right] & \text{if} \quad p^a_{eq} < p \\ 0 & \text{if} \quad p^d_{eq} < p < p^a_{eq} \\ J_{de} f^{de}_{T_2} = J_{de} \frac{1}{2} \left[\frac{C_T^2}{(C_H+C_T)^2} \right] & \text{if} \quad p^d_{eq} > p \end{cases} \tag{4.13}$$

$$J_{HT} = \begin{cases} J_a f^a_{HT} = J_a \frac{1}{2} \left[\frac{C_{HT}}{C_{H_2}+C_{T_2}+C_{HT}} \right] & \text{if} \quad p^a_{eq} < p \\ 0 & \text{if} \quad p^d_{eq} < p < p^a_{eq} \\ J_{de} f^{de}_{HT} = J_{de} \frac{1}{2} \left[\frac{C_H C_T}{(C_H+C_T)^2} \right] & \text{if} \quad p^d_{eq} > p \end{cases} \tag{4.14}$$

Pebble outer surface

This balance is performed in the same way as for the pipe walls. Again, pebble fluxes $J^p_{Q_2,i}$ are defined as shows expression 4.8. Expression then yields:

$$\frac{2D_Q}{\Delta r_p} \left(C^{sp}_{Q,i} - C^{p1}_{Q,i} \right) = J^p_{Q,i} = 2J^p_{Q_2,i} + J^p_{HT,i} \tag{4.15}$$

Internal pebble diffusion

This discretization has been made following the wall diffusion scheme, yet, in this case shperical coordinates has been coped. For the n-th layer the equation is:

$$\frac{1}{3} \left(\left((N_{lp} - j + \frac{1}{2})\Delta r \right)^3 - \left((N_{lp} - j - \frac{1}{2})\Delta r \right)^3 \right) \frac{dC^{pj}_{Q,i}}{dt} = \tag{4.16}$$

$$\frac{\left((N_{lp} - j + \frac{1}{2})\Delta r \right)^2}{\Delta r} D_Q \left(C^{pj-1}_{Q,i} - C^{pj}_{Q,i} \right) - \frac{\left((N_{lp} - j - \frac{1}{2})\Delta r \right)^2}{\Delta r} D_Q \left(C^{pj}_{Q,i} - C^{pj+1}_{Q,i} \right)$$

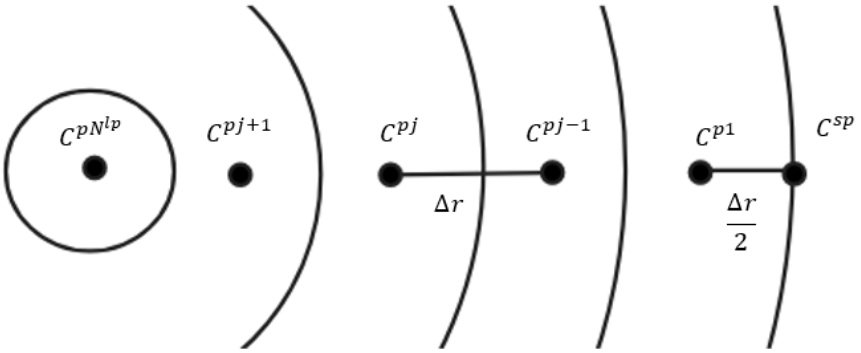

Figure 4.3.: Pebble discretization scheme.

4.4. Rooms

Whatever the layout of the system is, elements will be always located inside rooms (volumes) towards which the hydrogen leaks. Usually, more than one element permeates hydrogen to the same room. In this model, it has been considered that concentration is fully mixed over the volume. This can be done thanks to the high diffusivity among gases and the relatively small leakage compared with the total amount of room gas. Therefore, a single value of partial pressure for each molecule is needed to define the outside boundary condition of outer element surfaces. So far, the code is able to deal with three kinds of room:

- Ventilated: Those rooms have a finite volume V_r and a constant ventilation ratio. This flow inputs clean fluid to the room and drags some hydrogen out. The room pressure evolves then following expression 4.17

$$\frac{dP_{r,Q_2}}{dt} = -P_{r,Q_2}\dot{V}_{Recir} + J^{out}_{Q_2,i}\frac{RT}{V_r} \tag{4.17}$$

- Zero pressure: Those rooms are either so large or so well ventilated that the partial hydrogen pressure in contact with the ambient is considered to be negligible. Therefore, null pressure values are used as boundary condition for the different elements attached to such rooms.

- Permeation: This condition is useful for simulating small nonvented volumes, such as small reactors (an example is discussed in chapter 8). The way it works is by considering wall transport equations described for the pipe element. Those surface kinetics and internal diffusion is applied between the room concentrations and the outside, which is considered to have constant null concentration.

4.5. Numerical schemes

With all element balances defined, numerical schemes must be selected in order to solve this set of equations. As is going to be seen, sometimes simplifications need to be made in order to linearise the system.

4.5.1. Advection

Upwind scheme is used to solve advection term into the pipe gas volumes. Hence, the boundary concentration of each pipe slice are computed using the surrounding volume concentrations depending on the fluid direction. Thus, advective terms are defined as:

$$\begin{aligned} &\text{if} \quad (vS)_{i+} > 0 \quad \rightarrow \quad C_{i+} = C_i \\ &\text{if} \quad (vS)_{i+} < 0 \quad \rightarrow \quad C_{i-} = C_{i-1} \end{aligned} \tag{4.18}$$

4.5.2. Linearisation strategies

As it may be guessed, expressions 3.7 and 3.15 add non-linear terms to the system of equations to solve. Therefore, they need to be approximated by first order Taylor linearisation. This step is needed if all the variables are to be solved at directly by means of a unique set of linear equations. Besides, this strategy ensures mass conservation.

$$(C_X)^2 = 2C_X^* C_X - (C_X^*)^2 \tag{4.19}$$

$$C_X C_Y = C_X^* C_Y + C_Y^* C_X - C_X^* C_Y^* \tag{4.20}$$

$$\begin{aligned} k_0 \ln\left(\frac{k_1 (C_{X_2} + C_{Y_2} + C_{XY})}{k_2}\right)(k_3 - (C_X + C_Y)) = \\ = k_0 \ln\left(\frac{k_1 C_{Q_2}}{k_2}\right)(k_3 - C_Q) = \end{aligned} \tag{4.21}$$

$$= k_0 \left[k_3 \left(\ln\left(\frac{k_1 C_{Q_2}^*}{k_2}\right) - 1 \right) + \frac{k_3 - C_Q^*}{C_{Q_2}^*} (C_{X_2} + C_{Y_2} + C_{XY}) - C_Q^* - \ln\left(\frac{k_1 C_{Q_2}^*}{k_2}\right)(C_X + C_Y) \right]$$

$$\begin{aligned} k_0 \left(\frac{k_2 - (C_{X_2} + C_{Y_2} + C_{XY})\, k_1}{k_2}\right)(k_3 - (C_X + C_Y)) = \\ = k_0 \left(\frac{k_2 - C_{Q_2} k_1}{k_2}\right)(k_3 - C_Q) = \end{aligned} \tag{4.22}$$

$$= k_0 \left[k_3 \frac{k_2 - k_1 C_{Q_2}^*}{k_2} + k_1 \frac{C_Q^* - k_3}{k_2} \left(C_{X_2} + C_{Y_2} + C_{XY} - C_{Q_2}^*\right) + \frac{k_1 C_{Q_2}^* - k_2}{k_2} (C_X + C_Y) \right]$$

4.5.3. Time

Regarding the time derivatives, Euler discretization has been selected. However, two strategies have been followed simultaneously. Explicit scheme is used for the gas balances. On the other hand, for radial flux (diffusion) implicit scheme has been selected. Nevertheless, some simplifications have been made in this implicit scheme. For instance, slow changing terms such as room pressure is set explicitly as a boundary condition.

$$\frac{x(N_t) - x(N_t - 1)}{\Delta t} = \begin{cases} f(x(N_t - 1)) & \rightarrow \text{Euler explicit} \\ f(x(N_t)) & \rightarrow \text{Euler implicit} \end{cases} \tag{4.23}$$

4.5.4. Solver

Since the system has been linearised, the system of equations to solve can be written in matricial form:

$$[A]\{C\} = \{B\} \tag{4.24}$$

Being $\{C\}$ for the case of the pipe:

$$\{C\}^T = \left\{ C_{H_2}, C_{T_2}, C_{HT}, C_H^{sw}, C_T^{sw}, C_H^{w1}, \cdots, C_H^{wn}, C_T^{w1}, \cdots, C_T^{wn}, C_H^{so}, C_T^{so} \right\}$$

And for the case of the getter:

$$\{C\}^T = \left\{ C_{H_2}, C_{T_2}, C_{HT}, C_H^{sw}, C_T^{sw}, C_H^{w1}, \cdots, C_H^{wN}, C_T^{w1}, \cdots \right.$$
$$\left. \cdots, C_T^{wN}, C_H^{so}, C_T^{so}, C_H^{sp}, C_T^{sp}, C_H^{p1}, \cdots, C_H^{pN}, C_T^{p1}, \cdots, C_T^{pN} \right\}$$

where C_Q^{sw} and C_Q^{so} are the inner and outer wall surface concentration respectively, C_Q^{wj} the internal wall layer concentrations, C_Q^{sp} is the pebble surface concentration and C_Q^{pj} inner pebble layer concentrations.

Therefore, each time step can be solved firstly using Gaussian elimination to convert the matrix in an upper triangular one and then substituting terms backward. Appendix B shows the final definition of each term of $[A]$ and $[B]$ matrices depending on the case considered.

4.5.5. Solution algorithm

Since the code has been designed to cope with complex models, the way it works is as follows. Every global time step, each element of the system is solved following the fluid flow direction. Then, the fluxes of all elements are used to evaluate the partial pressure change over the rooms where they are located. This way, complex plant layouts can be composed by combining simplified and tested elements such as pipes and getters among others systems that may be included in the future. As showed Figure 4.1, inlet temperatures, mass flows and concentration are read from input files that, for instance, could be a thermohydraulic code outcome.

5. Condensate Parameters Model

5.1. General description

Condensate Parameters Models (CPM) are fully empiric parametric functions adjusted for a specific studied case in certain conditions. In this sense, CPM will just work close to the reference point in which it has been fitted, that is, defined. When a transient takes the system out of this reference point, CPM will adjust its parameters within its trained range. Thus, if for instance a CPM is fitted with oscillations of ± 50 %, any oscillation inside this limits will be adequately followed. Also, CPM's can be very easily graphically defined by using block diagrams as it is shown in Figure 5.1.

It is worth to mention that CPM's are set to work with variations over the reference point here. Hence, when CPM outcomes are analysed, it is understood that it is being refereed to variations over the reference, even if it is not explicitly mentioned. Therefore, increment symbol Δ nearby a variable of interest means it is being talked about such variation.

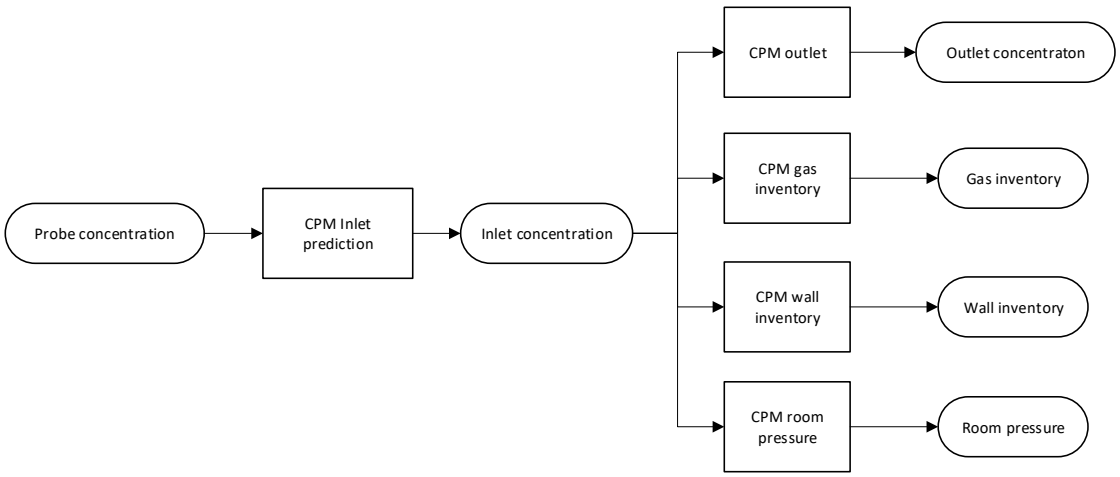

Figure 5.1.: Overall scheme of how CPM are used to predict the target variables for a pipe system.

Thanks to its simplicity, CPM's used in this study can be defined relatively easy in the time domain. Nevertheless, for future implementation of more than one CPM in a row so that they can control more complex systems, it is really helpful to use transfer functions. Those are obtained by applying the Laplace transform in order to work in the

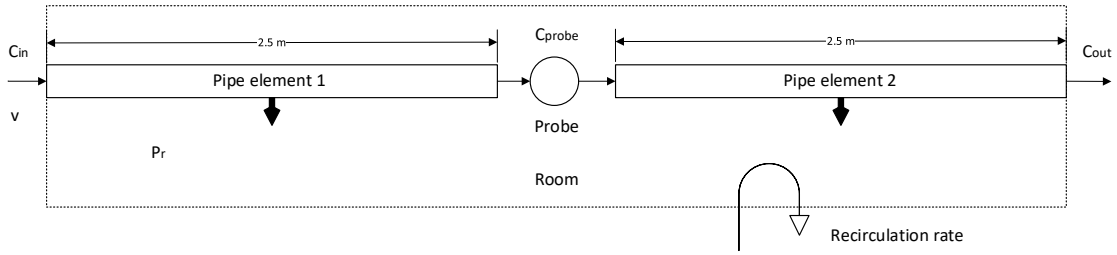

Figure 5.2.: Geometrical distribution of the CPM test case system.

Table 5.1.: Main parameters for the CPM test case system.

Variable	Nomenclature	Value	Units
Length	L	5	m
Inner diameter	d_i	0.02337	m
Outer diameter	d_o	0.02667	m
Total pressure	p_t	2.1	bar
Volume room	V_r	10	m
Recirculation rate	$\dot{V}_{Recir}$	0.001667	m^3/s
He flow rate		8	Nm/h
He velocity	v	2.73	m/s
H_2 inlet concentration	c_{in}	0.25415	mol/m^3
H_2 inlet partial pressure	p_{in}	630	Pa
Temperature	T	25	°C

imaginary domain as many authors point out [39, 40]. Transfer functions are defined as a continuous in time function, independent of the input signal and equal to the Laplace transform of the time response of the system to an impulse signal with all the initial conditions set to zero.

5.2. CPM scope

Since this chapter aims to study the potential of CPM as a real time predictive tool for tritium inventory, the simplest case has been implemented. A single pipe in a room has been tested as it is shown in Figure 5.2. It is important to notice that any different configuration, i.e. any change in the parameters described in Table 5.1, would require a new set of CPM. For instance, in the case of a getter system, new CPM would be needed for the pebble inventory. Besides, more complex ones (such as the whole tritium plant) could be built up from those simple CPM proposed.

5.3. Outlet concentration

As it can intuitively be predicted, in a pipe where advection term is several orders of magnitude larger that diffusion, changes in concentration will propagate along the pipe at gas speed. This way, diffusion can be neglected and output wave front will mostly preserve the input shape as shown in Figure 5.3.

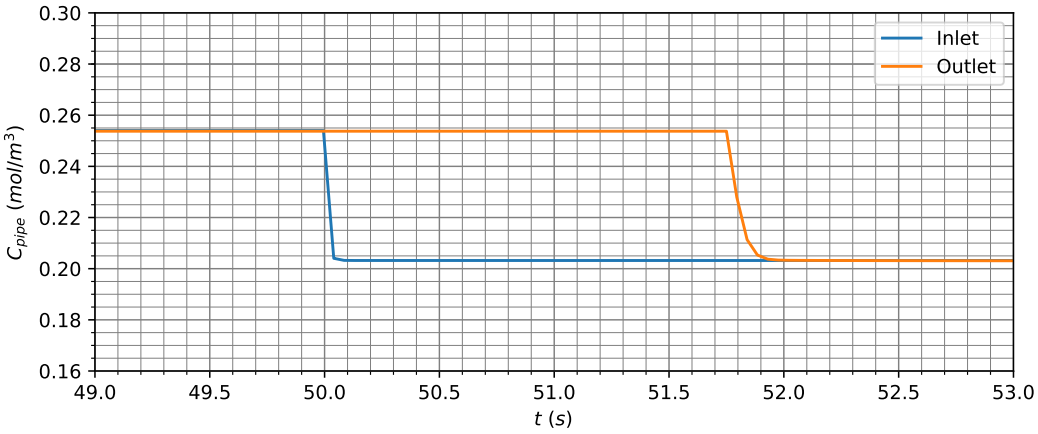

Figure 5.3.: Outlet and inlet concentration values during a transient where a step-shaped perturbation inputs the system.

5.3.1. Time domain function

Hence, as it has been seen in Figure 5.3, output concentration (equation 5.1) will be nothing but the inlet one delayed by a time τ_{out} (period of time particles take to travel from pipe beginning to the end) and reduced by a factor K_{out}, proportional to the system efficiency to maintain hydrogen inside the pipe.

$$\Delta c_{out}(t) = K_{out}\, \Delta c_{in}\,(t - \tau_{out}) \tag{5.1}$$

5.3.2. Transfer function

Applying the Laplace transform to equation 5.1 and knowing that time delays are represented as complex exponentials and constant factors are not affected by the transform it leads to expression 5.2.

$$\frac{\Delta C_{out}(s)}{\Delta C_{in}(s)} = K_{out}\, e^{-s\tau_{out}} \tag{5.2}$$

5.4. Inlet concentration

Notice that in the set up of the case simulation (Figure 5.2), a sensor probe was located in the middle of the pipe length. In an actual implementation, only probe information will be available to the control system. Since all the following parameters are going to be defined as a function of the inlet concentration, it is necessary to develop a CPM that predicts inlet concentrations as a function of the sensor measurements ones.

5.4.1. Time domain function

Essentially, the time domain function is similar one used for the C_{out} CPM in section 5.3. The difference is that, in this case, C_{in} is a function of future values of C_{probe}, and hence a "forward" function needs to be used.

$$\Delta c_{in}(t) = K_{in}\, \Delta c_{probe}\,(t + \tau_{in}) \tag{5.3}$$

5.4.2. Transfer function

In the same way as it was done in section 5.3, the transfer function for C_{in} is analogous to expression 5.2.

$$\frac{\Delta C_{in}(s)}{\Delta C_{probe}(s)} = K_{in}\, e^{s\tau_{in}} \tag{5.4}$$

5.4.3. Practical considerations

Mathematically, the function has the same shape as output concentration CPM seen in section 5.3. Nonetheless, as the function is using a forward in time value (future one), in practice, that means to predict data which has not being measured yet. Therefore, since during on-line runtime that is impossible, inlet concentration data at present time will be available after a delay of τ_{in}.

For the reasons explained before, future values can not be predicted on-line and hence, transfer function form are useless in this case. Hence, time domain function "tricked" to just give delayed data is the only alternative here.

5.5. Pipe gas inventory

Once concentrations at the main pipe locations are defined as a function of the sensor probe, inventories can be defined as the molar sum of one specific isotope. In the scope of this work, protium is the only one considered (due to obvious practical issues). Therefore, its corresponding inventory (named n_g for simplicity) is nothing but expression 5.5 shows, being V_g the inner volume of the pipe element modelled.

$$n_g = V_g(2[H_2]) \qquad [mol_H] \tag{5.5}$$

Performing a balance to the gas inside the pipe will lead to the expression 5.6. That is, pipe hydrogen inventory variations are proportional to the difference in concentrations between input and output (represented as the delayed input by a time $\tau_g = \tau_{out}$) times a constant K_g related to the hydrogen permeation efficiency out of the pipe.

$$\frac{\partial \Delta n_g}{\partial t} = K_g \left(\Delta c_{in}(t) - \Delta c_{in}(t - \tau_g)\right) \tag{5.6}$$

5.5.1. Time domain function

By redefining equation 5.6 in discrete differences and rearranging terms, the gas inventory variation with time can be described as:

$$\Delta n_g(t + \Delta t) = \Delta n_g(t) + K_g \left(\Delta c_{in}(t) - \Delta c_{in}(t - \tau_g)\right) \Delta t \tag{5.7}$$

5.5.2. Transfer function

On the other hand, if Laplace transform is applied to expression 5.6 then equation 5.8 is obtained.

$$\Delta N_g(s)\ s + \Delta n_g(t_0) = K_g \left(\Delta C_{in}(s) - \Delta C_{in}(s)\ e^{-s\tau_g}\right) \tag{5.8}$$

From the transfer function definition, initial conditions must be null, that is $\Delta n_g(t_0) = 0$ and therefore:

$$\frac{\Delta N_g(s)}{\Delta C_{in}(s)} = \frac{K_g \left(1 - e^{-s\tau_g}\right)}{s} \tag{5.9}$$

5.6. Wall inventory

Regarding molar hydrogen content in the pipe solid walls (from now on wall inventory n_w), its variation over time would be inversely proportional to the amount of hydrogen in the pipe wall itself and proportional to concentrations in the surroundings. Since CPM looks for simplicity, two major simplifications have been made:

- Firstly, hydrogen atoms are in atomic form inside the solid lattice (that means, not as H_2 molecules). However, all the surrounding media, both the exterior room and inner pipe, are gases where hydrogen is actually in molecular form. Hence, according to Sievert's law, solid concentration is squared proportionality [15]. Nevertheless, it is assumed to be almost linear for small variations close to the reference point where the model have been fitted.

- The second one is the proportionality refereed to the surroundings. All this is condensed as a function of the inlet hydrogen concentration of the pipe, since the exterior conditions are assumed to be function of the inlet concentration as well. Thus, the whole proportionality is encapsulated inside K_w constant and τ_w delay.

According to this considerations, the balance is reduced to expression 5.10, where T_w is a global time constant of the whole process, like K_w is with the C_{in} proportionality. Additionally, a possible delay τ_w is considered to be suitable of being fitted as well.

$$T_w \frac{\partial \Delta n_w}{\partial t} = K_w \, \Delta c_{in}(t - \tau_w) - \Delta n_w(t) \tag{5.10}$$

5.6.1. Time domain function

In this case, simply by rewriting the expression 5.10 in finite differences and isolating the next time step value, a expression for wall inventory in time domain can be easily found:

$$\Delta n_w(t + \Delta t) = \frac{\Delta n_w(t) + K_w \, \Delta c_{in}(t - \tau_w) \left(1 - \frac{T_w}{\Delta t}\right)}{\frac{T_w}{\Delta t}} \tag{5.11}$$

5.6.2. Transfer function

In order to obtain the transfer function from equation 5.10, Laplace transform is again applied. Knowing that initial values of N_w originated from the derivative are null, the relation leads to:

$$\frac{\Delta N_w(s)}{\Delta C_{in}(s)} = \frac{K_w \, e^{-s\tau_w}}{1 + T_w s} \tag{5.12}$$

5.7. Room pressure

Room pressure presents a similar behaviour as wall inventory. Hence, it is going to be modelled in the same way. Moreover, the same assumptions are made in order to perform the balance. However, in this case, CPM gives the result as room molecular concentration, and then pressure values will be derived from the air concentration using ideal gas law. Equivalently, given a defined volume for the room V_r, total inventory can be defined too (equation 5.13).

$$p_r = c_r R T = \frac{n_r}{V_r} R T \qquad [Pa_{H_2}] \tag{5.13}$$

This way, the simplified balance is of the form:

$$T_r \frac{\partial \Delta c_r}{\partial t} = K_r \, \Delta c_{in}(t - \tau_r) - \Delta c_r \tag{5.14}$$

5.7.1. Time domain function

From room simplified balance (equation 5.14) time domain CPM expression 5.15 is easily derived by means of finite differences and rearrange of terms.

$$\Delta c_r(t+\Delta t) = \frac{\Delta c_r(t) + K_r\,\Delta c_{in}(t-\tau_r)\left(1-\dfrac{T_r}{\Delta t}\right)}{\dfrac{T_r}{\Delta t}} \tag{5.15}$$

5.7.2. Transfer function

On the other hand, transfer function is also found by applying Laplace transform to the room balance in the same way as was done to wall inventory.

$$\frac{\Delta C_r(s)}{\Delta C_{in}(s)} = \frac{K_r\,e^{-s\tau_r}}{1+T_r s} \tag{5.16}$$

5.8. Fitting methodology

Once all CPM have been proposed for each relevant quantity of interest in a pipe system, this section will show the methodology to define the parameters. Considering a given reference point, then some step-shaped positive and negative perturbations to this reference are introduced into the system. Each perturbation will generate a different set of data from the outcome of a 1.5D simulation. For each perturbation there will be an optimal set of CPM parameter values.

With constants already fitted for each CPM, it can be easily identified some correlations between this set of constants and concentrations in the pipe. Since most CPM give as outcome the behaviour of one variable as a function of the inlet concentration, it is therefore quite useful to correlate the fitting constant variation for his set-up as a function of c_{in}. The only exception is CPM constants for inlet concentration itself, which is defined as a function of the sensor concentration measurements. In these particular case, obviously these constants are correlated as a function of this data values.

5.8.1. Analytical formulas

For some particular CPM parameters, there are simple analytical formulas to compute such values. In the case of concentrations delays, they are computed as the time a particle takes to go through the pipe, shown at equation 5.17. On the other hand, the factor for concentrations CPM would be proportional to the system efficiency for maintaining hydrogen inside the pipe, and it is computed as the concentration ratio between the objective quantity and the input one in steady state (equation 5.18).

$$\tau = \frac{2L}{v} \tag{5.17}$$

$$K_2 = \frac{c_2}{c_1} \tag{5.18}$$

5.8.2. Optimization algorithm

Nevertheless, the majority of CPM parameters can not be analytically computed. In such cases an optimization process is launched in order to find the parameters that fit the best. Since in most cases this process is multi-variable, SIMPLEX slop based algorithm is used to perform the adjustment [41], avoiding the need of computing all the possible set of combinations.

Besides, good enough initial values for the optimization are required to ensure the absolute optimal outcome is reached (avoid local maximums of the objective function). Since several optimizations are run (one per step simulated), values obtained from the previous case can be used as initial seed for the following.

5.8.3. Variation with input variable

When determining the values of CPM parameters for each step case, it is clearly seen (as shows Figure 5.5) their value depends on the input variable (in this case the inlet concentration). Therefore, in order to have a CPM capable of predicting any perturbation, these values need to be expressed as a function of the input variable of the corresponding CPM. For all the cases, a second order polynomial of the type $ax^2 + bx + c$ shows to be precise enough for the purpose. In this function, x is the used input variable of the CPM (sensor concentration for inlet one parameters and inlet concentration for the remaining). Hence, constant parameters are given with the c value.

5.8.4. Example results

As has been explained previously, parameters values will be correlated according to quadratic fits. The reference point shown in Table 5.1 is taken as an example. Over this reference, positive and negative perturbations from up to 50% of amplitude over the reference are introduced as shows Figure 5.4. The results of these example fitting process are summarized in Table 5.2 and 5.3. An example of the parameter tendencies was shown in Figure 5.5 as well.

Table 5.2.: Coefficients for CPM parameters computation. Inlet concentration (as function of probe concentration), outlet concentration and gas inventory are shown.

	$K_{in}(c_{probe})$	$\tau_{in}(c_{probe})$	$K_{out}(c_{in})$	$\tau_{out}(c_{in})$	$K_g(c_{in})$	$\tau_g(c_{in})$
	—	s	—	s	—	s
a	0.0005423	0	-0.001195	0	0	0
b	-0.0002657	0	0.0005648	0	0	0
c	1.0002656	0.91575	0.999455	1.8315	0.002341	1.8315

Table 5.3.: Coefficients for CPM parameters computation. Wall inventory and room concentration are shown.

	$K_w(c_{in})$ $\times 10^5$	$\tau_w(c_{in})$ s	$T_w(c_{in})$ s	$K_r(c_{in})$ $\times 10^5$	$\tau_r(c_{in})$ s	$T_r(c_{in})$ s
a	14.56	0	5.048	8.67	0	20.1602
b	-6.58	0	-1.804	-4.01	0	-604.49
c	5.81	0	9.065	3.93	16	147.271

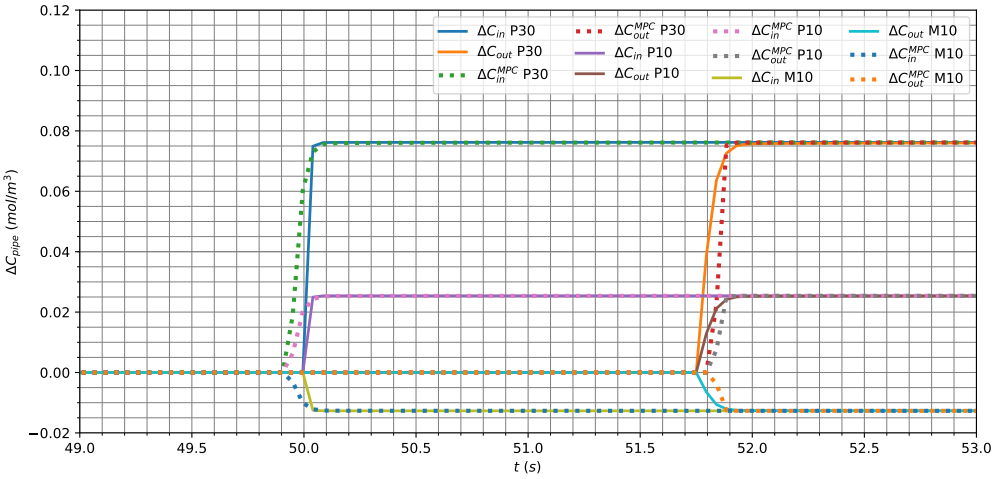

Figure 5.4.: Examples of step-shaped concentration perturbations introduced over the reference point shown in Table 5.1.

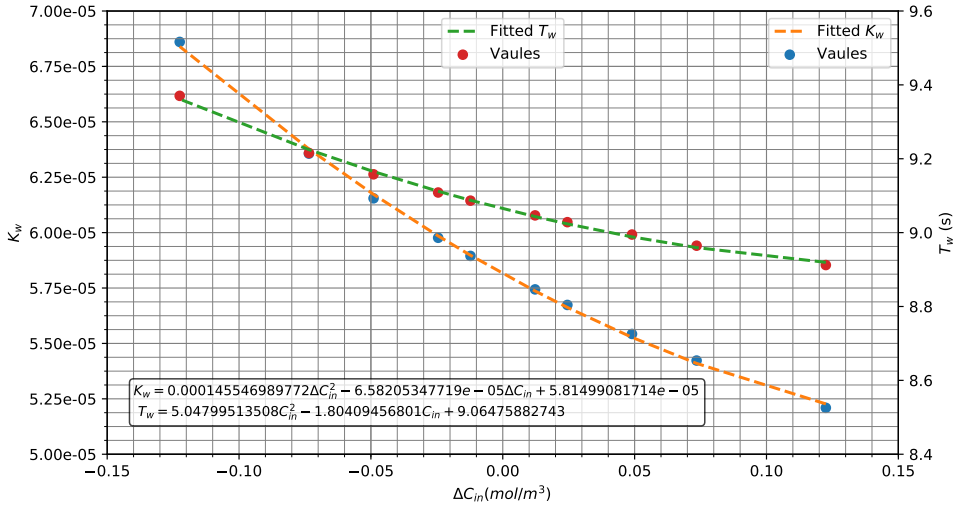

Figure 5.5.: Example of second order polynomial fitting over some CPM parameters (wall inventory).

6. Hydrogen Detector Characterization

6.1. Introduction

So far 1.5D model has computed what would be real concentrations along the pipe. This "clean" data has been used to fit properly CPM parameters. However, actual sensor probes are not free of some undesirable behaviour such as slow response to fast perturbations and signal noise. In order to confirm that CPM has real utility, it is mandatory to demonstrate they can deal with real degraded information, process them and give a reliable prediction of reality in real time.

This chapter aims to characterize a generic sensor used to measure hydrogen concentration inside the pipe. Data registered by a simple experiment run by Sarrià Chemical Institute (IQS) team would be used [42].

Once the sensor is fully characterized, it is possible to emulate how the probe signal obtained from the case simulated with the 1.5D model would look like. This allows to design processing techniques aimed to transform noised raw signal into estimations of the actual values along the system. During this chapter both noise and real estimation filters are developed. Figure 6.1 shows the whole process followed through the previous chapter and this one. Notice how, in a CPM's plant implementation, once the sensor is already characterized the process begins from the probe response directly (i.e., there is no need for emulating the sensor).

6.1.1. Sensor description

The sensor designed and built by IQS is an amperometric one. Hydrogen concentration will be proportional to the current read. Basically, it consists in a ceramic membrane where a differential of voltage is applied between its faces. On both sides of this membrane inert atmospheres (argon in this case) are in contact. When a concentra-

Figure 6.1.: Probe signal simulation process. If working with virtual reality generated data, time response simulator and noise adder are necessary, otherwise not (if applied to real sensor data).

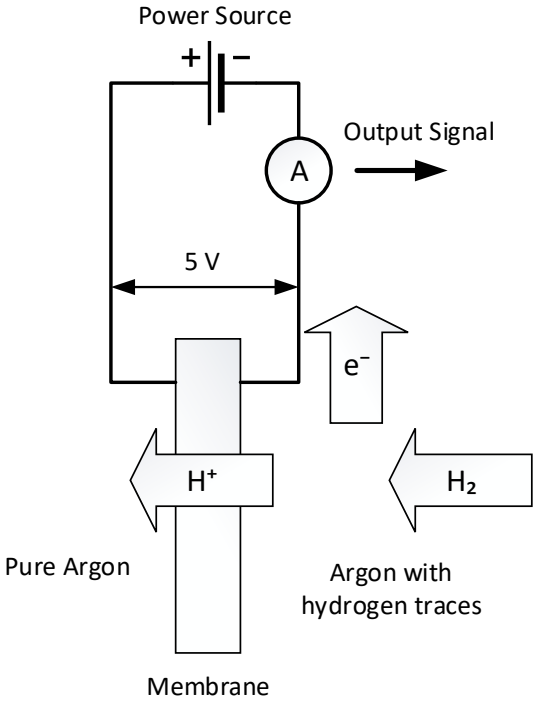

Figure 6.2.: Simplified diagram showing how the IQS tested sensor works.

tion of hydrogen is present on one side of the membrane, atoms will permeate. However, under the electric field, the membrane will only allow protons to go though. Electrons must go all over the electric circuit to meet protons at the other side. Such movement of electrons is the current measured. Figure 6.2 schemes in a very simplified way the mentioned process.

6.1.2. Sensor test reactor

In order to understand the sensor characterization process and experimental data, is quite important to bear in mind the reactor size and shape where the sensor was located as shown in Figure 6.4. Thus, reactor was a cylinder 209 mm tall with a 31.21 mm diameter. Inlet and outlet perforations are at the top whereas sensor is located in the volume centre. A thermocouple inside the reactor controls heated walls in order to maintain inner volume temperature of the gas at 500 °C. Figure 6.3 shows a scheme of the experiment set up.

6.2. Experiment

The experience performed consisted in a series of controlled concentration steps. In order to achieve so, a mixture of two gases is performed in the right proportions. On the one side there is 99.999 % pure Argon gas and on the other hand there is Argon

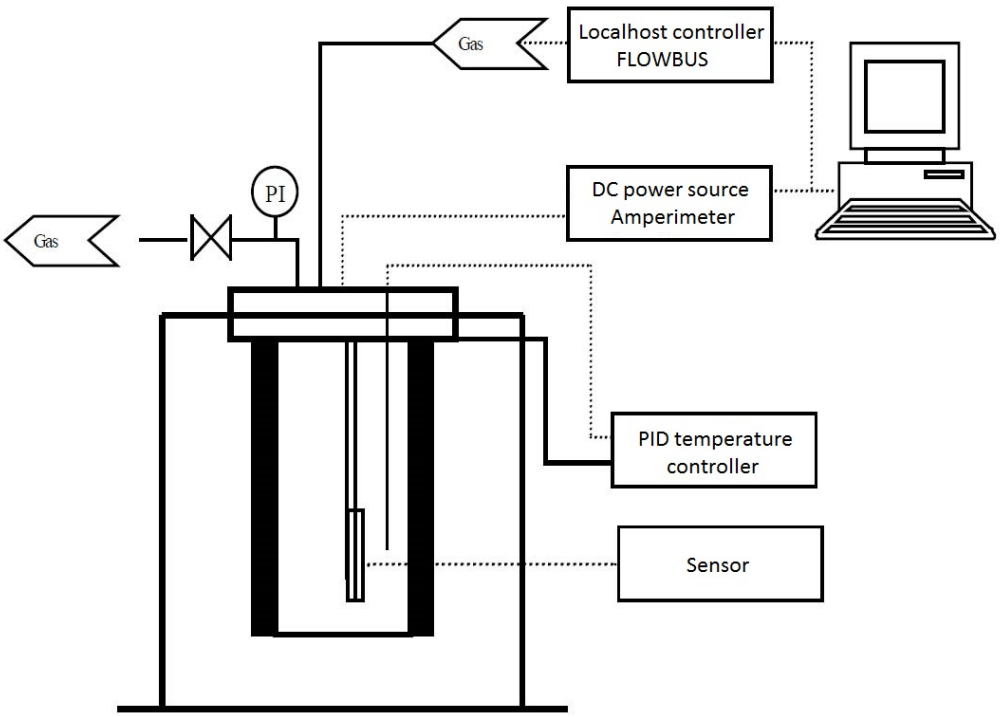

Figure 6.3.: Experimental set up used to continuous data acquisition. Adapted from [42].

mixture with 0.5 % (5000 ppm) of hydrogen content. A valve controls the released volumetric flow and set it to 600 mL/min. Desired concentrations are achieved by adjusting proportions of both gases. This way, concentration steps are produced.

Since the experiment aim is to characterize the sensor response, it is necessary to know and quantify the main sources of uncertainty in the experiment. Since fluid used is a gas, full mixture can be assumed as a good approximation. The corresponding characteristic time τ_v given the reactor volume and experiment mass flow is 62 s. Besides, calibration of the mixing valves will determine whether or not the theoretical concentrations of the mixture are followed. Moreover, the probe calibration is another source of uncertainty, and must be quantified as well. Hence, probe calibration determines the valid range of concentrations the experiment is allowed to move within.

6.2.1. Flow uncertainties

As mentioned before, hydrogen concentration in the pipe flow is adjusted by increasing or decreasing valve opening positions of the two mixed gas sources. Hence, any uncertainty over the actual value of these flows is directly and proportionally translated into an uncertainty in the actual value of the hydrogen concentration released through the flow valve.

For the explained set up, flow uncertainties after the calibration process are within the range of ± 0.5 %. So all measurements will have at least this uncertainty trans-

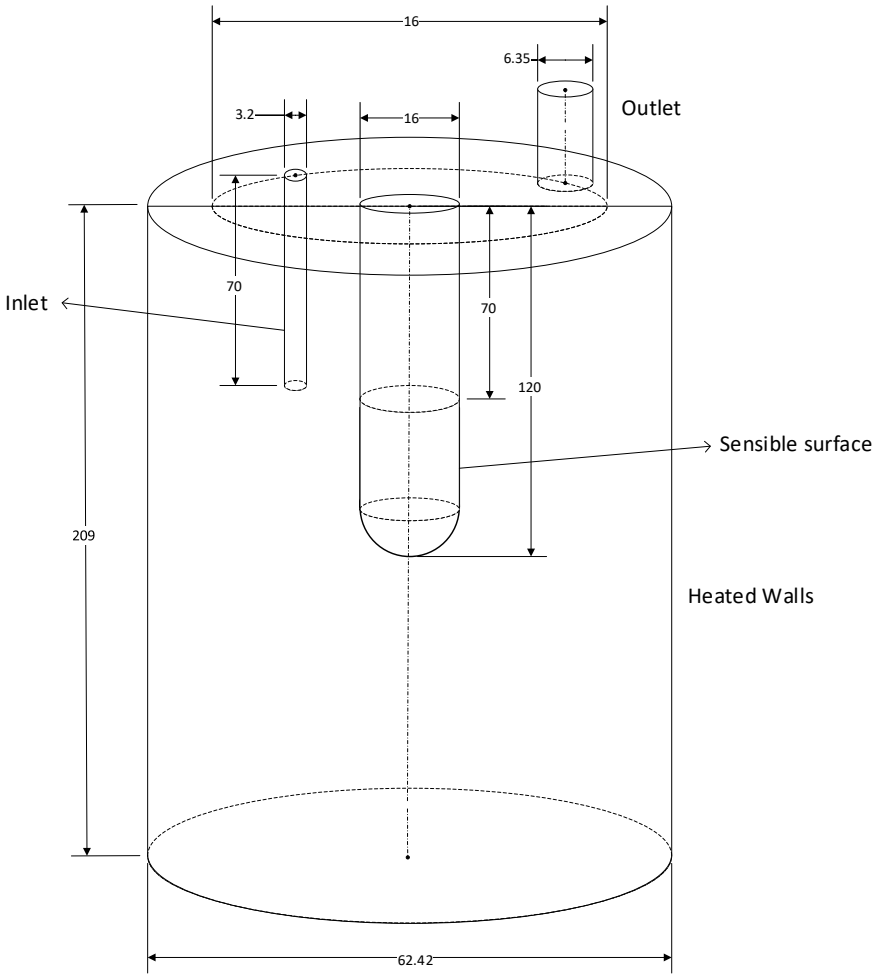

Figure 6.4.: Scheme with the shape and size of the reactor used in the experiment.

lated to concentration. In this case that will result in ± 25 ppm.

6.2.2. Sensor calibration curve

On the other hand, the sensor itself provides an electric current output (of mA) proportional to the measured concentration in ppm. To determine the proportion, firstly the probe calibration curve must be determined by performing some steady state measurements. Figure 6.5 shows results and the fitted curve obtained for concentrations within the range of 250 to 1600 ppm.

As can be seen in Figure 6.5, though R^2 of the fitted curve is high, standard deviation S of this fit turns out to be 26.1 ppm. Hence, values of the curve are within the range of ± 52.2 ppm with 95 % confidence interval.

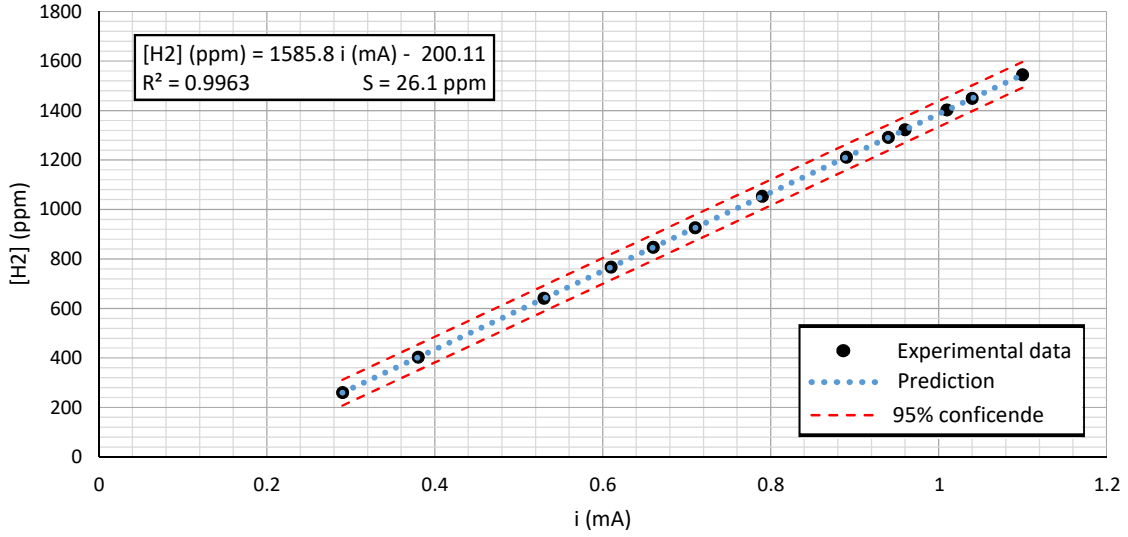

Figure 6.5.: Probe calibration curve fitted by steady state measures. Data extracted from IQS experiment [42].

6.2.3. Experimental data

Figure 6.6 shows the results of the experiment, a row of variable steps which goes from 0 to 1600 ppm. In this graph, current signal has not been yet translated to hydrogen concentration by means of the fitted curve presented in the previous section. A zoom in one of these steps can be seen in Figure 6.8.

Nonetheless, it has been noticed quite clear dependencies between the current measured and the total mass flow though the sensor reactor in other experiments carried out by IQS. They seem to appear even when concentration is kept constant. Figure 6.7 shows the commented dependencies. Such dependency is unknown and should be studied deeper in order to fully understand the detector. Hopefully, since the set of data used in this case was performed at constant mass flow this phenomena is not affecting the results.

6.3. Model

Now, with the information from section 6.2.3 a model to characterise the probe behaviour with two main components is proposed. First, the overall slow characteristic time of the probe and second, the signal noise.

6.3.1. Time response

It is clearly seen from the experiment results that the probe response is not instantaneous. Instead, against a sharp concentration variation, the probe takes some min-

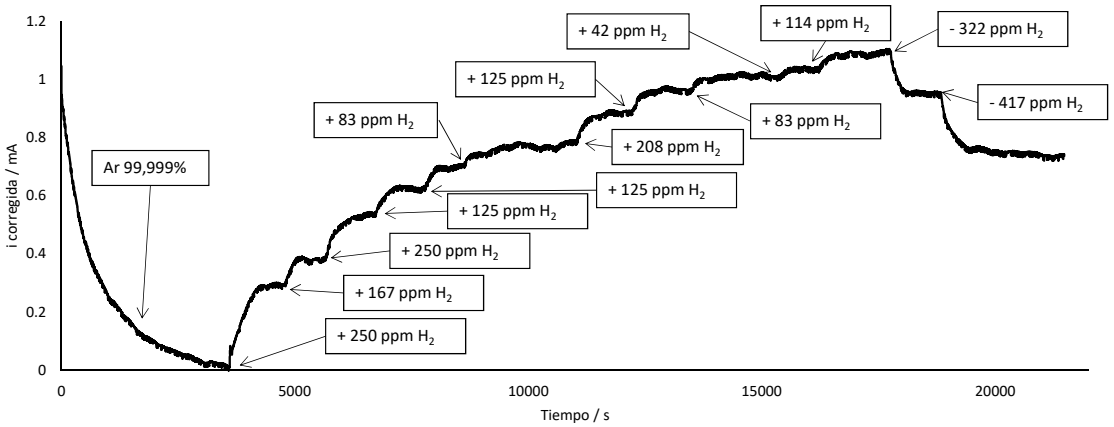

Figure 6.6.: Measurements recorded in the IQS experiment [42] used for determine the time constant of the detector. Changes in reference concentration are shown in boxes, mass flow was constant at 600 ml/min.

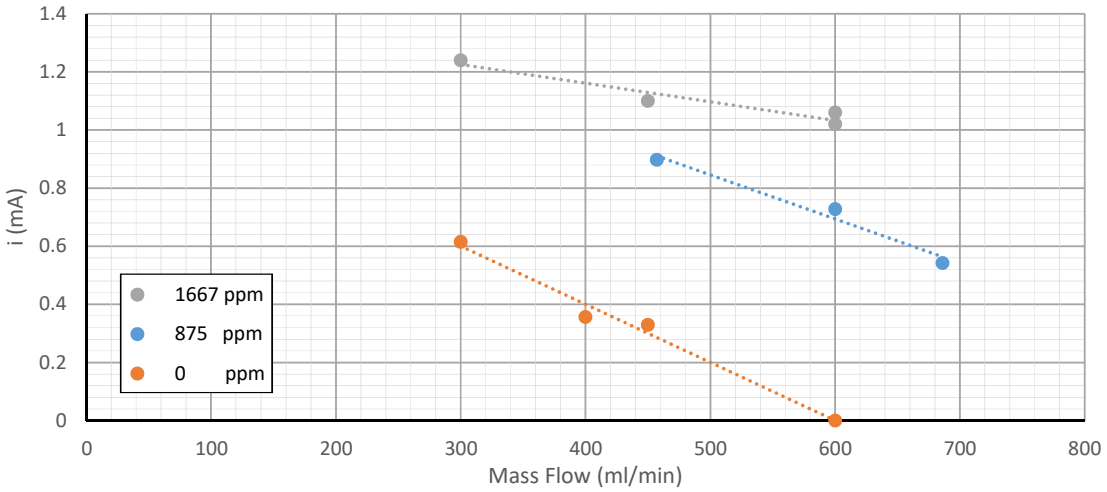

Figure 6.7.: Correlations between current measured and mass flow for steady state points. Data used to elaborate it has been obtained from IQS experiment [42].

utes to reach the equilibrium again. With the set up description of the reactor shape and size given in section 6.1.2, it is clear that part of this delay is due to the characteristic time of the reactor volume ($T_v = 62$ s) calculated from the full mixture assumption. That is, the time that cylinder takes to be homogeneously fulfilled at the new concentration level.

Hence, the aim is to determine how much of this slow time response is due to this effect and how it is intrinsic of the sensor. In order to do so, an analytical expression can be determined by solving the system of differential equations 6.1 and 6.2 obtained by performing a balance both to the cylinder volume and to the sensor itself. For the reactor, balance is straightforward, and for the sensor, an analogy is made so that the variation of probe measure c_s depends on the difference between actual values c_v on the probe location (in this case reactor volume) and the measurements themselves. Concentration at this place is assumed to be equal to the average of the cylinder, according with the full mixture assumption. This way, the probe signal trends asymptomatically to the real value after several characteristic times T_s.

$$\begin{cases} T_v \dfrac{\partial c_v}{\partial t} = c_{in}(t) - c_v(t) & (6.1) \\ T_s \dfrac{\partial c_s}{\partial t} = c_v(t) - c_s(t) & (6.2) \end{cases}$$

Considering initial conditions are known values from a previous steady state where sensor has reached equilibrium with the volume concentration:

$$\begin{cases} c_{in}(t=0) = \Delta c_{in} & (6.3) \\ c_v(t=0) = c_s(t=0) = c^0 & (6.4) \end{cases}$$

Equation 6.1 can be easily solved alone and leads to expression 6.5. Using this solution into Equation 6.2, a formula for the evolution of sensor measurement with time is deduced as a function of the characteristic times of the cylinder T_v and the sensor T_s.

$$c_v(t) = c^0 e^{-t/T_v} + \Delta c_{in}\left(1 - e^{-t/T_v}\right) \tag{6.5}$$

$$c_s(t) = c^0 e^{-t/T_s} + \frac{T_v}{T_s - T_v}\left[\left(e^{-t/T_v} - 1 + \frac{T_s}{T_v}\left(1 - e^{-t/T_s}\right)\right) + c^0\left(e^{-t/T_s} - e^{-t/T_v}\right)\right] \tag{6.6}$$

This way, sensor characteristic time T_s can be determined by fitting this parameter separately for each step transient of the experimental data set using curve 6.6 and performing a non-linear least squares process. An instance of such fit can be seen at Figure 6.8. Then, an average time value and its statistical deviation for the selected useful steps is computed (some of those steps have been discarded, either because they were out of the calibration range of the probe or because they clearly shows fluctuations on the concentration once steady state has been reached).

From this adjust process, the followings results shown at Table 6.1 have been obtained. Values found for the characteristic time of the sensor reveals that is about

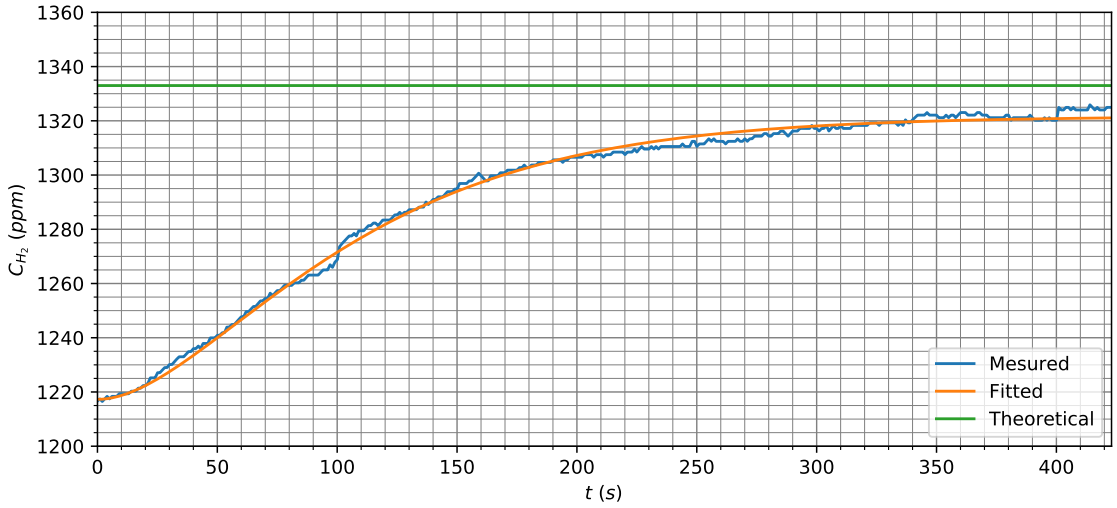

Figure 6.8.: Example of the step from 1208 to 1333 ppm and its fitted curve. Notice how in this particular case, there is a difference between the reference value and measurement steady state value of the order of 15 ppm. Note that measured signal has been post-processed using the algorithm that will be shown in section 6.4.1 to eliminate the hysteresis noise (described in the following section).

Table 6.1.: Sensor characteristic parameter values obtained from the analysed data.

Parameter		Values (95% confidence)			
Response time	T_s	53.76 $\pm$	14.65 s		
Reference error	$o(c)$	-23.11 $\pm$	50.49 ppm	(-10.3 $\pm$	22.5)$\times 10^{-4}$ mol/Nm^3
Noise amplitude	A_n	2.30 $\pm$	4.11 ppm	(1.03 $\pm$	1.83)$\times 10^{-4}$ mol/Nm^3

half of the reactor volume time. On the other hand, $o(c)$ is the error found between the reference value, and the steady state value from the fitting process. As can be seen, its mean is close to -23 ppm, and its deviation is of the order of 50 ppm. Correcting this offset can get the probe inside the predicted error due to calibration found in section 6.2.2. Besides, noise amplitude has been characterized, its noticeable how such values are one order of magnitude lower than the reference value error.

Additionally, it is worth to mention that the sensor intrinsic characteristic time T_s could be decomposed in several components, such as chemical characteristic time and electronics. In these terms, capacitive behaviour of the electronic circuit may play an important role, since at each system this circuits will differ. However, for CPM purposes, all this issues are included in the time response parameter T_s. By doing such simplification it is possible to simulate the probe with a simple functions (both in time and complex domains) as it will be shown in section 6.3.2. However, this means for each set up this parameter needs to be adjusted by a set of tests if fine precision is needed.

In any case, as it can be seen from the uncertainties values, this first set of data

gives an estimation of the order of magnitude. Yet, it is not enough to characterize them properly. In order to reduce the this dispersion, a larger row of experiments is needed.

6.3.2. Sensor functions

Along previous section, the system of equations used describe the sensor behaviour was presented. Once the characteristic times T_v and T_s are known, in order to implement a model which can simulate such instrument this system must be solved, either in time domain or with a transfer function. For the first case, simple discretization leads to:

$$\begin{cases} c_v(t+\Delta t) = c_v(t) + \dfrac{\Delta t}{T_v}\left(c_{in}(t) - c_v(t)\right) & (6.7) \\ c_s(t+\Delta t) = c_s(t) + \dfrac{\Delta t}{T_s}\left(c_v(t) - c_s(t)\right) & (6.8) \end{cases}$$

On the other hand, using Laplace transform the transfer function for the sensor signal can be defined in one step:

$$\frac{C_s(s)}{C_{in}(s)} = \frac{1}{(sT_s+1)(sT_v+1)} \tag{6.9}$$

6.3.3. Noise

Additionally is clear that, besides the time response, some noise is attached to the signal while measuring it. However, as seen in Figure 6.10, this noise seems to have two component. One is a fine random noise with a low dispersion (less than 2 ppm). Besides, there is a bias major component which oscillates in a hysteresis like cycle of a variable frequency within the range of 0.1 to 0.02 Hz and a dispersion of about 15 ppm.

Therefore, the proposed models to reproduce the same kind of noise signal is a hysteresis cycle between one position or another. Every time step there is a chance of changing the hysteresis state $\pm e$, and this probability is set by the mean frequency at which this changes take place $\bar{f}$, and of course, the time step size used in the simulation ∂t. Then, inside each state, there is always a random noise added. This way, Figure 6.9 represents the two Gaussian distribution of the model, where the probability to go from one to the other is given by expression 6.10. As can be seen in Figure 6.10 the proposed model shows to be suitable for representing the noise behaviour.

$$P(+e \rightarrow -e) = P(-e \rightarrow +e) = 2\bar{f}\partial t \tag{6.10}$$

6.4. Noise filter design

As it has being seen in section 6.3.3, noise of the probe signal is characterized by two main components. White random noise has a frequency equal to the sampling time

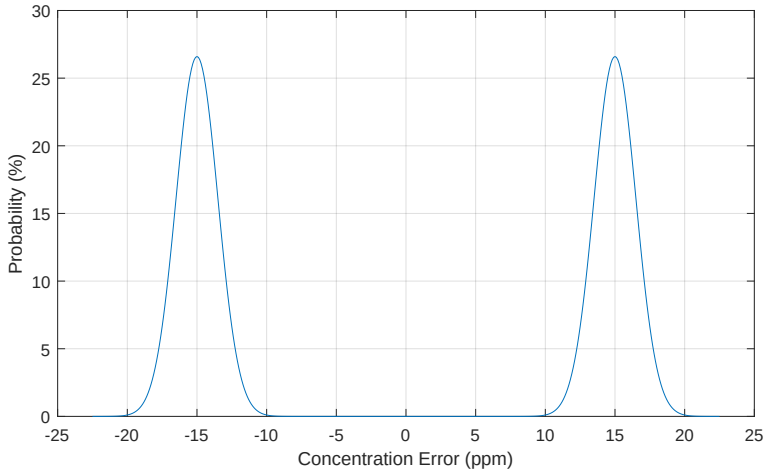

Figure 6.9.: Gaussian distribution of the sensor concentration error. Notice how each bell integral sums a probability equal to one. This is because there is an independent chance every time step given by expression 6.10 in order to change from one bell to other (hysteresis biased noise).

itself, and its amplitude is within in the range of 2 ppm or lower. On the other hand, hysteresis noise is harder to characterize. Besides, its characteristic period varies from 10 up to 50 s, which means an average frequency of 0.03 Hz.

6.4.1. Hysteresis error corrector

As commented in previous chapter, it seem to appear an hysteresis like error in the experimental data recorded. This kind of noise is not particular of any physical system nor electronic circuit, so with all likelihood it is caused during the digitalization of data. While this problem is being understood and fixed, this work proposes a simple algorithm in order to post-process the signal and eliminate such errors.

The algorithm basically chooses either the high value signal or the low one and defines it as the reference signal. This way, any variation of its value several times higher the average white nose is interpreted as the hysteresis error. Then, the variation value is stored as a bias error and used to correct the following data points until the signal comes back to near zero bias error. Figure 6.11 shows an example of the results of this process.

6.4.2. Low-pass filters

In order to eliminate white noise, a low-pass filter is proposed [43]. These are characterized because they pass signals with a frequency lower than a certain cut-off frequency and attenuates signals with frequencies higher than the cut-off one. Mathematically, this filters are transfer functions of a certain order whose coefficients are selected so that they produce the desired cut-off frequency. First and second order examples of basic

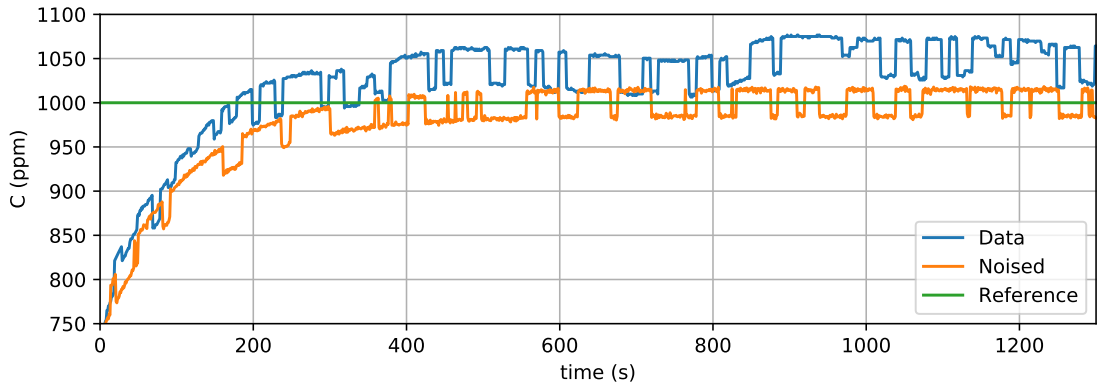

Figure 6.10.: Comparison between real data and simulated noised data. Notice how fluctuations and the reference error are not simulated.

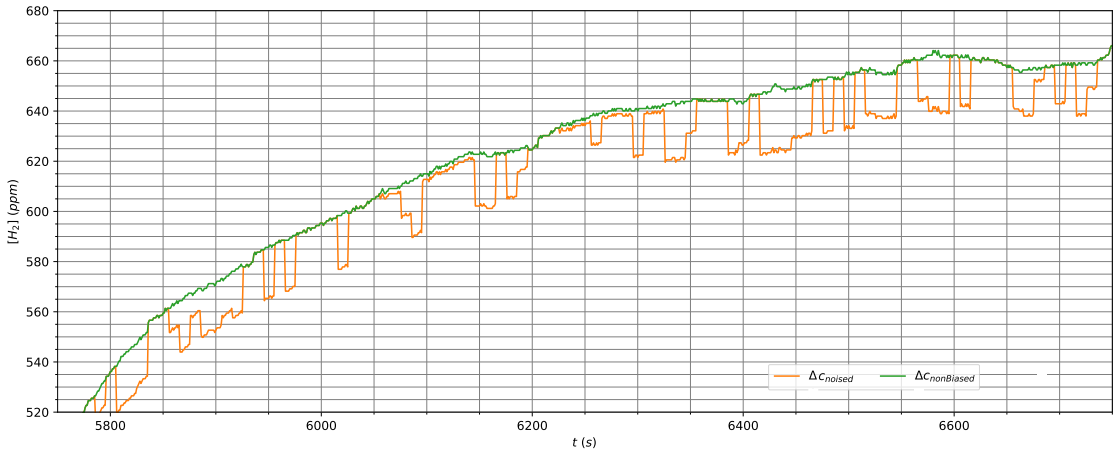

Figure 6.11.: Example of the hysteresis corrector algorithm applied to experimental data records.

low-pass filters can be seen in equations 6.11 and 6.12 respectively, being ω_0 the cutoff frequency expressed in rad/s and ζ the damping ratio.

$$F^{1)}(s) = \frac{1}{1 + s/\omega_0} \tag{6.11}$$

$$F^{2)}(s) = \frac{\omega_0^2}{s^2 + 2\zeta\omega_0 s + \omega_0^2} \tag{6.12}$$

More generically, filter of other n have the expression 6.13 form. In order to be coherent with bibliography, b_i are the numerator coefficients and a_i the denominator ones.

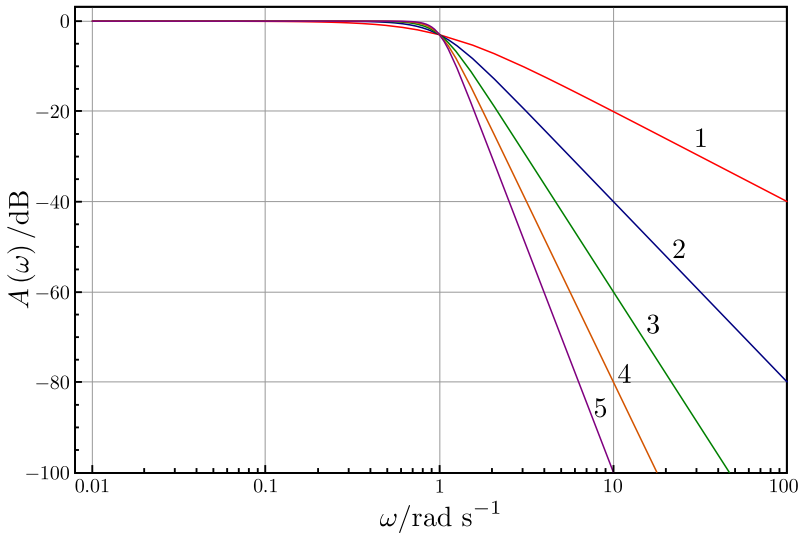

Figure 6.12.: Comparison of the influence of the filter order for the same cut-off frequency.

$$F(s) = \frac{\sum_{i=0}^{n-1} b_{i+1} s^i}{\sum_{i=0}^{n-1} a_{i+1} s^i} \tag{6.13}$$

A bode diagram representing the magnitude and phase response of this kind of filters can be seen in Figure 6.12. As can be seen, the higher filter order, the faster grows the attenuation ratio with frequency.

Among the filters available, IIR (Infinite Impulse Response) filters are the most simple ones and they casually meet a given set of specifications with a much lower filter order than a corresponding FIR (Finite Impulse Response) filter. In such category, there are Butterworth, Chevisev types I and II and elliptic filters. Their responses can be seen in Figure 6.13. For this application, Butterworth filter has been selected due to its relatively simplicity and effectiveness.

With the noised signal characterized, cut-off frequency and the order of the low-pass filter must be selected so that real concentration values in the sensor position can be estimated adequately.

As a matter of fact, it is desirable to find values of such parameters that reduce the noise, so that the estimation function can work properly, without increasing the response time of the signal. Otherwise results will be just as delayed as raw signals. The higher filter order, the more noise attenuation is achieved, necessary for keeping the output signal stable. However, with this response time also rises. On the other hand, the higher selected cut-off frequency the, best noise reduction is get, but again, its time response increases too. Hence, there is a compromise between noise reduction grade and time response speed. In this case, filter order was set to 3 and cut-off frequency tuned to 0.01 Hz.

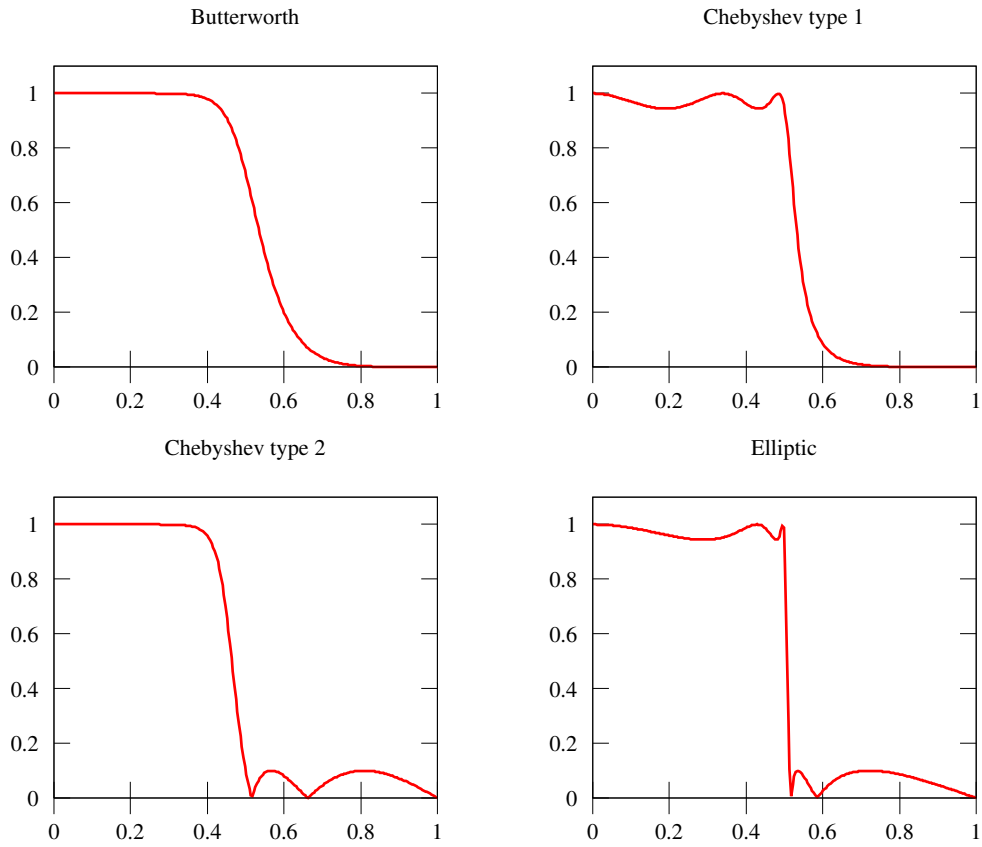

Figure 6.13.: Comparison of the most commonly used FIR filter responses.

6.4.3. Filter delay correction

As it can be seen in the example of filter outcome in Figure 6.14, it is clear that such tool also delays the signal. In order to correct that, the group delay of the filter can be computed for each frequency as shown from expression 6.14. The average delay applied to the signal can be estimated and then used to correct it calling the "forward" function 5.3 described in section 5.4.

If $H(e^{i\omega})$ is the frequency response of a filter, thus group delay is defined as:

$$\tau_f(\omega) = -\frac{\partial\theta(\omega)}{d\omega} \tag{6.14}$$

where $\theta(\omega)$ is the phase of $H(e^{i\omega})$. Nevertheless, alternatively to the use of the "forward" function, double filter (fist forward and then backwards) can be used instead. Thus, the group delay provoked by the first filtering is compensated by the second filtering, which is performed backwards and leads to an advancement of the signal equal to the delay of the first filtering process. This process is clearly illustrated in Figure 6.14.

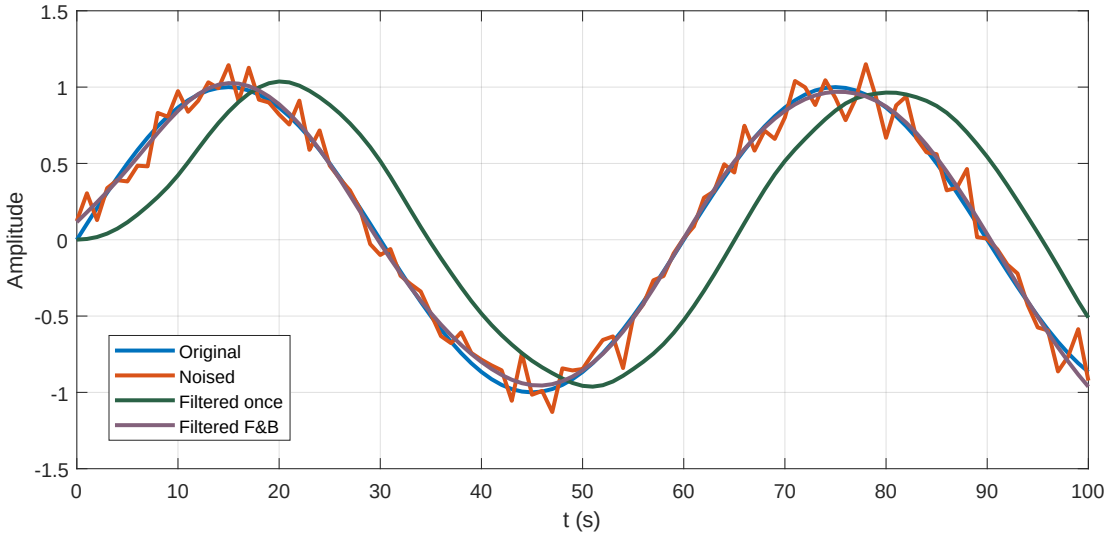

Figure 6.14.: Example of filter group delay and its correction using double (forward and backward) filtering technique.

6.5. Design of estimative function

Section 6.3.1 showed how time response of the sensor can be modelled by using equation 6.6. Then, since now it is interesting to define actual input value of concentration c_{in} as a function of the value read from the sensor c_s, terms can be rearranged in order to do so, following an inverse plant strategy [44]. In the same way as it has been done on each CPM its function can be defined both at time domain or as a transfer function.

Nevertheless, it is very important to mention these implementations result in the evaluation of improper functions (predicting future values), whose gains are infinite for high frequencies inputs. That is why a high frequency filter must always be set up among them and the signal source (the sensor) to prevent the output to become highly unstable.

6.5.1. Time domain function

Rearranging terms and using one more time finite differences over equations 6.7 and 6.8 leads to the following expressions. Notice how, in this occasion, derivatives are discretized using present and past values, so that on-line available information is used.

$$\begin{cases} c_v(t) = T_s \dfrac{c_s(t) - c_s(t-\Delta t)}{\Delta t} - c_v(t) & (6.15) \\ c_{in}(t) = T_v \dfrac{c_v(t) - c_v(t-\Delta t)}{\Delta t} - c_{in}(t) & (6.16) \end{cases}$$

Notice how, were the sensor placed directly into a pipe (as the case analysed in section 5.2) it would not be needed the volumetric balance. In such case, only sensor

characteristic time constant is used. This is the reason why computing both characteristic time contributions was quite interesting. Now intrinsic information about the detector itself is known.

6.5.2. Transfer function

Here, simply using transfer function 6.9 and inverting it:

$$\frac{C_{in}(s)}{C_s(s)} = (sT_s + 1)(sT_v + 1) \tag{6.17}$$

However, $(sT + 1)$ functions are not causal, that is, they have a numerator order higher than denominator one. Thus, this expressions are predicting future values and can not be computed in such way. Luckily, according to [45], there is a mathematical approximation which can be used:

$$sT \simeq \frac{sT}{s\alpha + 1} \qquad \text{with} \quad \alpha \ll T \tag{6.18}$$

Notice how α its just a numerical zero, for instance, $\alpha \sim 10^{-6}$. The smaller this value, the more exact is this approximation. In practice, such trick works when this value is at least two orders of magnitude smaller (too small α values might become the function unstable when the input signal is noised). Therefore, transfer function 6.17 can be rewritten as follows:

$$\frac{C_{in}(s)}{C_s(s)} \simeq \left(\frac{sT_s}{s\alpha_s + 1} + 1\right)\left(\frac{sT_v}{s\alpha_v + 1} + 1\right) = \left(\frac{s\,(T_s + \alpha_s) + 1}{s\alpha_s + 1}\right)\left(\frac{s\,(T_v + \alpha_v) + 1}{s\alpha_v + 1}\right) = \\ = \frac{s^2(T_s + \alpha_s)(T_v + \alpha_v) + s(T_s + \alpha_s + T_v + \alpha_v) + 1}{s^2\alpha_s\alpha_v + s(\alpha_s + \alpha_v) + 1} \tag{6.19}$$

As commented before, in the case of a sensor directly placed into a pipe section, the volume constant would be zero, and then the expression is simplified to:

$$\frac{C_r(s)}{C_s(s)} = \frac{sT_s}{s\alpha_s + 1} + 1 = \frac{s\,(T_s + \alpha_s) + 1}{s\alpha_s + 1} \tag{6.20}$$

Section 6.6.1 will show how the estimative functions performs ideally (when there is no added perturbations to the signals). Additionally, this tool is tested in section 6.6.2 with real lectures, where other perturbations and noises are mixed with the signal.

6.6. Results

Finally, in order to assess the quality of the described filter, it is going to be applied to some examples. Firstly, simulated results are going to be predicted. They can be compared with the reference values since they are other output of the simulation.

Table 6.2.: Concentration perturbation input function used for the 1.5D simulation. Discontinuities in function values stem for sharp steps.

Time (s)	Variation (percentage or function)
0 - 50	0%
50 - 1050	Sin between $\pm$10%
1050 - 2050	Ramp from +20% to +5%
2050 - 3000	0%

Then, the experimental data input is foreseen. Since the reference concentration values are known, differences with the model can be assessed too.

6.6.1. Simulation prediction

Results from the 1.5D model simulation of the system described in section 5.2 at sensor location are used in this approach. The simulation consist in the system response against a concentration perturbation input function with the shape shown at Table 6.2.

This data is manipulated with the treatments explained previously in this chapter. Thus, it can be simulated how an actual sensor will response against such kind of perturbations. Once this is done, filters along this chapter are used too. The aim is to estimate the original signal as well as possible. This way, the full process described at section 6.4 is followed. Figure 6.15 shows each step of the mentioned process. As can be seen, the prediction quality is remarkably good despite the big perturbations introduced.

It is worth to mention that for this particular layout, the sensor was considered to be placed directly into the pipe. Therefore, the reactor characteristic time was zero and expression 6.20 could be used.

6.6.2. Experiment data prediction

The second assessment is performed to the recorded data. This time not only noise but other perturbations on real data are present. Thus, it can be evaluated whether or not the estimation tool works in this situation too. Since this time the input signal is the actual sensor one, only filters explained in this chapter are used over it.

The outcome of this test is shown in Figure 6.16. As can be seen, now predictive tool can not perform as precise as before. Other fluctuations in the signal alter the final result. Nevertheless, the prediction is always closer to the reference ($\pm$20 ppm) and follows the step perturbations with just a delay of the order of 100 s (a noticeable improvement compared to the 500 s of the filtered sensor signal).

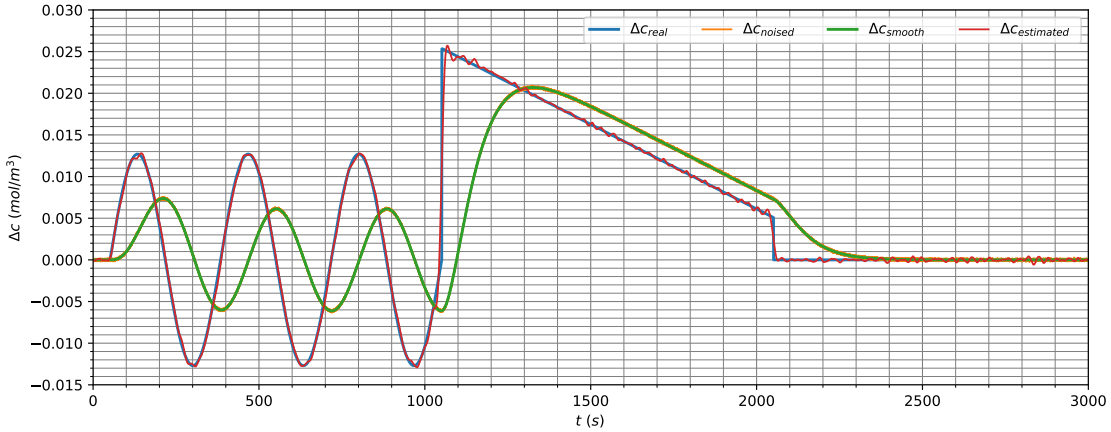

Figure 6.15.: Simulation of the sensor response (orange) calculated over the simulated model outcome (blue). The signal low pass filter is applied then (green) and finally, the estimative function (red) is used to predict what was the original concentration value (which in this case is taken as the model outcome).

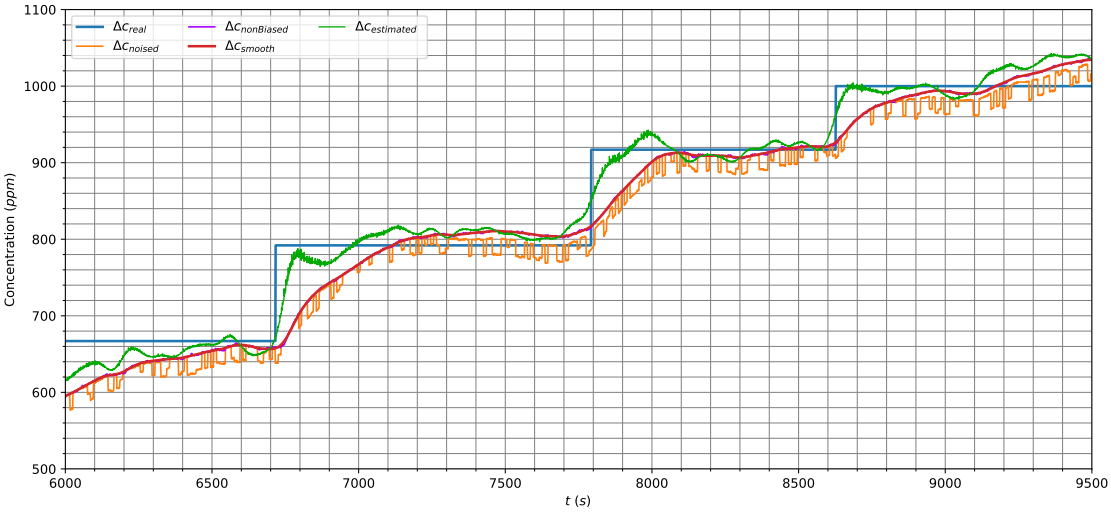

Figure 6.16.: Signal treatment applied to experimental data (orange). Hysteresis error corrector was used first (purple), then low pass filter was applied (red) to finally predict the signal using the estimative function (green).

7. Analysis of Model Errors

7.1. Introduction

In order to assess the quality of all the predictions, a deeper study on the sources of error along the methodology is discussed in this chapter. First, quality of the predictive model is discussed. Then a comparison between CPM predictions of system inventories and detailed model outcomes is performed. Finally, errors provoked by the CPM itself will be compared in magnitude with the errors coming from the sensor and other sources of uncertainty.

7.2. Predictive model

A comprehensive validation of the 1.5D code will require the experimental analysis of test cases. This due to the fact that bibliographic data is quite disperse (especial mention to surface parameters as mentioned in section 3.7). As the next chapter will show, such experiments are already being designed and will be a very important milestone within PROTOCODAC project. Nevertheless, so far the model must show that is mass conservative and that gives same results as other much more detailed (in terms of time and spatial discretization) codes, like CFD simulations.

Regarding mass conservation, the code proves to close the global mass balance with a numerical error of the order of 10^{-18}. This order of magnitude corresponds to the precision of 64 bits float variables natively used by Python [2]. Besides, relatively speaking, this value represents an error of 0.0001 % of the lowest value computed across the simulation.

On the other hand, the code has been tested against CFD simulations. CFD results have been computed with a custom OpenFoam solver originally developed by Mas de les Valls [4]. Such solver includes the same physic models and parameters used for the predictive 1.5D code.

7.3. Total inventory

So far, each amount of hydrogen inventory has been computed separately. However, for the purpose of understanding how much CPM solution differs from detailed model, total inventory n_{tot} is used instead:

$$n_{tot} = n_g + n_w + 2n_r \qquad [mol_H] \tag{7.1}$$

This total inventory can be computed both for the detailed results and the CPM ones. Besides, another total inventory can be defined by integrating the global balance of the system using CPM values, that is:

$$\frac{\partial n_{tot}^{int}}{\partial t} = 2\left(c_{in}^{CPM} - c_{out}^{CPM}\right)\dot{V} - n_r^{CPM}\dot{V}_{Recir} \tag{7.2}$$

where $\dot{V} = vS$ is the volumetric flow through the pipe.

Notice how this defined variable gives an idea of the global performance of the prediction. Some materials tend to cumulate more hydrogen than others. Therefore, estimating accurately those values becomes more crucial than the rest.

7.4. CPM mismatches

This section aims to assess the error committed by each CPM prediction function over the precise results of the virtual model. Notice how this way, CPM work with clean simulated values, so that the intrinsic error of those functions can be assessed separately.

7.4.1. Case definition

In order to test the CPM predictive performance, 1.5D model outcome resulting form the test concentration input function defined in section 5.2 is used again. Indeed, the input for CPMs is the same as the one used to fed the sensor functions in previous chapter. As it can be seen, such input profile is quite more complex than the simple steps used to adjust the CPM parameters. CPM would have real application only if they are able to predict complicated inputs from a relatively simple set of training simulations.

7.4.2. Comparison

Figure 7.1 shows the different concentrations, pressures and inventories simulated for the test input on the virtual reality model versus the values predicted by the CPM. As it can be seen, the prediction performs very well against the test input.

However, in order to assess the error produced by the prediction, differences between both results are computed in Figure 7.2. Since each inventory has its own magnitude, relative error values are plot so that they can be easily compared. These are calculated based on the reference inventory values at steady state.

As it can be seen in Figure 7.2, room inventory is the magnitude with the largest average error. This is understandable as it is the least related magnitude, that is, physically, it is the farthest magnitude computed from the inlet concentration. Moreover, sharp fluctuations cause the bigger errors. Nevertheless, such sudden peaks are very unlikely during real plant operation. In any case, the average error (referred to total inventory) is always below 0.05 %, with possible punctual mismatches of some variables up to 0.5 %.

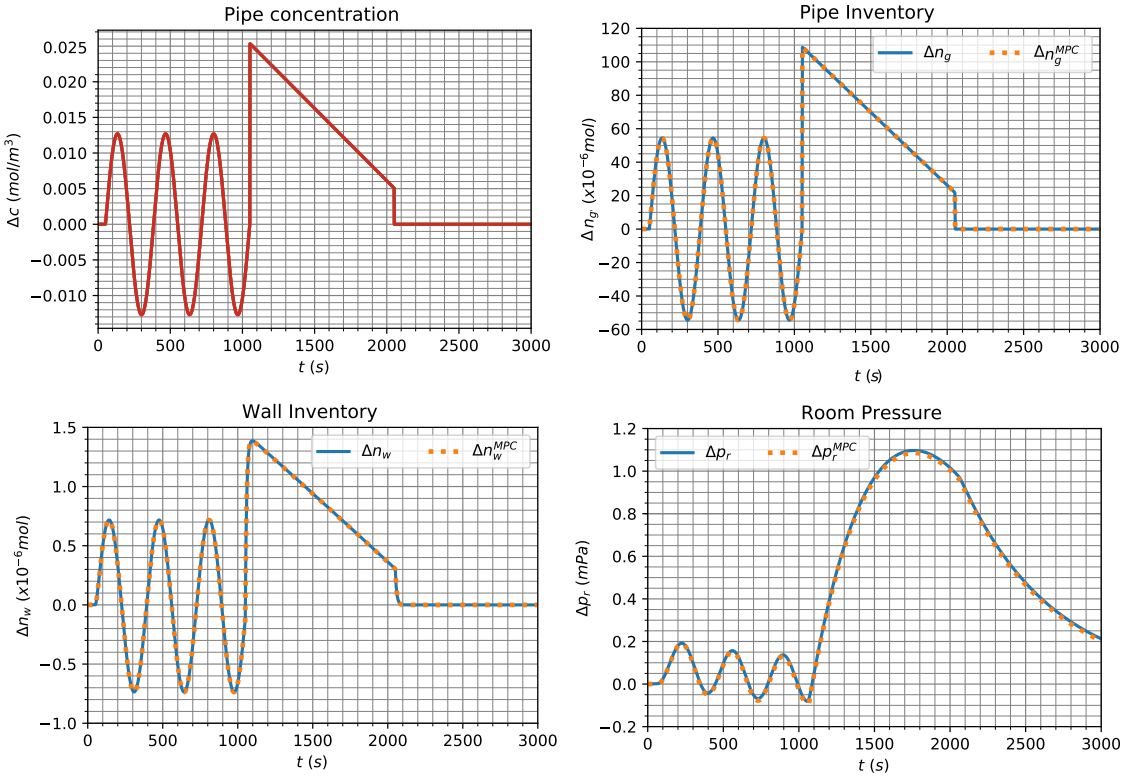

Figure 7.1.: Different CPM estimations compared with the simulated values. Note that variables plotted are variations over the reference (steady state) values.

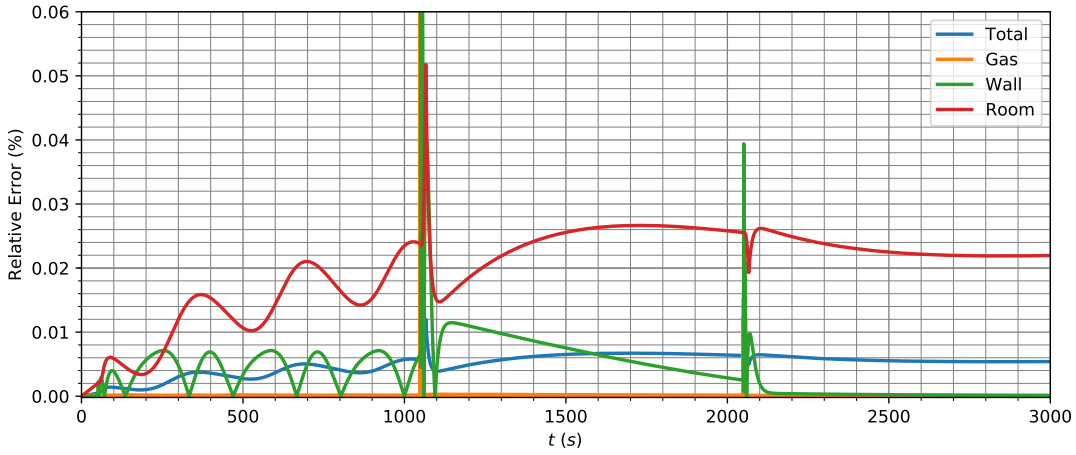

Figure 7.2.: Relative error between virtual model outcome and CPM prediction. Reference inventories are the corresponding absolute steady state values.

7.5. Sensor related errors

Now that errors due to CPM have been quantified, quality of the concentration estimated at sensor location needs to be assessed as well. Error related to this prediction is going to be split up in two sources.

On the one hand there is the error of the estimative tool. This error can be computed using clean values produced by the 1.5D model (already seen in section 6.6.2). On the other hand, intrinsic errors of the sensor itself and external fluctuations, as it could be non constant gas flow. These errors can be indirectly computed from the differences between predictions performed over simulated and real data.

As mentioned, in order to ease the comparison, same input perturbation used for CPMs (described on Table 6.2) is used here.

7.5.1. Estimative error

When using clean input data from the 1.5D model to feed the sensor simulations, differences in those estimations over the simulated values are the errors committed by the tool. Since noise is introduced randomly to the signal when emulating it, a statistic study have been made. By running the tool 50 times, an average mean error and an average maximum error have been computed. Results are summarized in Table 7.1. As can be seen, those errors are an order of magnitude larger than those computed for the CPM.

7.5.2. Sensor intrinsic error

Finally, error from the predictions of data recorded in experiments are compared to the reference values. This difference minus the already computed error for the estimative tool should be the intrinsic errors of the sensor and measurement system as described by expression 7.3.

$$\frac{c_{ref} - c_{estimated}}{c_{ref}} = o(c)_{global} = o(c)_{intrinsic} + o(c)_{estimative} \tag{7.3}$$

As can be seen in Table 7.1, averaged intrinsic errors of the calculated resulted one order of magnitude larger than the estimative ones. Moreover, it is very noticeable that the intrinsic error of the sensor was founded to be in the same order of magnitude than the predicted uncertainties due to mass flow in section 6.2.1 (± 25 ppm caused by flow variations winch would be translated to ± 2.5 % in a flow with a reference concentration of 1000 ppm).

Table 7.1.: Global measurement error, statistical error associated with the use of estimation tool and calculated value of the intrinsic sensor error.

Error	Global	Estimative	Intrinsic
Mean	2.3997 %	0.1825 ± 0.0116 %	2.2172 ± 0.0116 %
Maximum	43.7435 %	6.3279 ± 0.2554 %	37.4156 ± 0.2554 %

8. Experimental Set Up Design

8.1. Introduction

Alike it has been seen along previous chapters, accuracy of the predictive model is a key element to ensure that CPM are actually computing a good inventory prediction. So far, CFD calculations have been used to check the results. However, such simulations include the same physical principles. Therefore, without an actual experimental test, the model can not be truly validated.

With this purpose, a piping set up experiment is discussed in this chapter. The idea is to locate 2 of the sensor reactors studied in chapter 6 in a row. A pipe will be placed between both sensors. This pipe will be located within a controlled volume where concentrations measurements can be made as well. Ideally, if the permeation throughout pipe walls is fast enough, the increase in the concentration outside should match the difference in concentration between inlet an outlet sensors. Though its likely that such difference falls below the detection limit of the sensors (due to their accuracy), it might be possible to induce tendencies in both detectors.

As it will be seen, the main issue is to determine the appropriate material, experiment dimensions and conditions so that permeation could take place fast enough. This way its variation could be measured in a reasonable time outside the pipe. Besides, if the process took too long, hydrogen could eventually leak out of the experimental device.

As it will be seen during next section, different reactor designs compromise their operation temperature. This is very relevant for the expected permeation rate since transport parameters are strongly temperature dependant (they follow Arrhenius laws as explained in chapter 3).

8.2. Material selection

Beforehand, there is plenty of possible materials to be selected for the pipe. Studied ones are listed below:

- Stainless Steel ALSI 316: It is commonly used in fusion designs. It has the lowest diffusivity and slowest superficial kinetics rates. However, its relatively low price allows to built a large set up (large pipe lengths).
- Stainless Steel ALSI 304L: Not so considered as a fusion material. Nevertheless is the cheapest option having similar properties to SS316. Besides, thinner walls can be purchased.

- α-Fe: Pure BCC ferritic iron has much better diffusivity than stainless steel options. However, there is too much uncertainties regarding the superficial kinetic rates (depending whether or not is oxidised and the superficial treatment). Moreover, this option is more expensive, so pipe length is limited.
- 75Pd-25Ag: This specific alloy is widely used for isotopic membrane separation of hydrogen. Therefore, it has great permeation rates. Besides, pipes can be found with very thin thickness. Nevertheless it is too expensive for more than some centimetres of pipe.

Table 8.1.: Experimental set up design options considered for different layouts. Each material transport parameters used have been computed from Tables 5.2 and 5.3 at the specific temperatures of each case.

Material	L (m)	ϕ (mm)	e (mm)	Layout	H (mm)	D (mm)	V (l)	T (°C)
SS 304	1-3	6.35	0.5	Compact	208.9	62.48	0.63-0.54	500
SS 316			0.89					
75Pd-25Ag	0.1-0.2		0.1					
α-Fe	1-2	4	0.2				0.63-0.60	
SS 304	60	6.35	0.89	Large	510	400	62.18	27.3
SS 316	60		0.5					

8.3. Designs

Two designs were proposed to allocate the piping system. Each of them intend to maximise one of the two main parameters in which permeation rates depend on, length and temperature.

Nevertheless, since both designs rely on the sensor set ups described in chapter 6, inlet conditions of both designs are similar. That implies an inlet concentration of 3000 ppm and a volumetric flow of 600 ml/min at 500 °C.

8.3.1. Large layout

This layout was the first design proposed. Thanks to its big volume (62.18 l), it could allocate up to 60 m of pipe in a coil like distribution. Figure 8.1 shows a scheme of the proposed design.

However, the reactor size of makes impossible to pressurize it. Consequently, no heating systems are allowed for safety reasons. Only the pipe gas heated in the inlet sensor will provide thermal energy to the reactor. However, such amount of heat is not enough to keep the volume temperature at 500 °C despite the use of a good insulation. Therefore, according to the thermal calculations provided in Appendix C, equilibrium temperature of such set up would eventually stabilise close to room temperature.

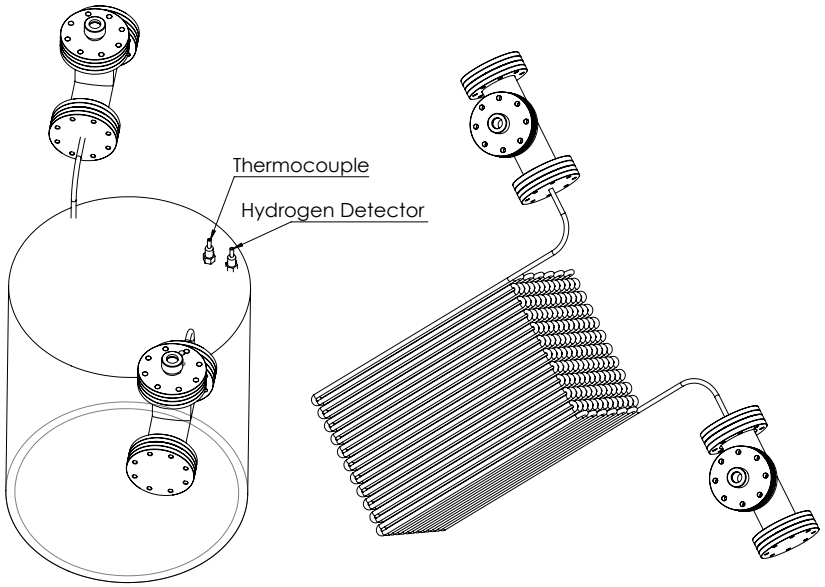

Figure 8.1.: Large experimental set up proposed for the predictive model validation. Original from IQS designs.

8.3.2. Compact layout

In order to provide a solution for the lack of heating in the pipe volume, a second design is proposed. This proposal takes advantage of the same mechanical parts that allows sensor volumes to be heated up. Nevertheless the reactor volume is reduced drastically here down to 500-600 cm^3. Figure 8.2 shows the design characteristics.

Inside this volume, a maximum of roughly 3 m coiled pipe could be allocated. On the other hand temperature could be kept at 500 °C, speeding up dramatically the permeation ratio of hydrogen throughout the pipe.

8.4. Foreseen results for experimental transient

In order to compare different options two parameters are studied over time. The ratio at witch hydrogen permeate out of the pipe, which equals to the variation of concentration in the reactor volume:

$$\frac{dC_r}{dt} = J_{out} \tag{8.1}$$

And the concentration difference between inlet an outlet, defined as:

$$dC = C_{S,i} - C_{S,o} \tag{8.2}$$

Due to the foreseen lack of resolution of sensors, conditions of the experimental transient must maximize the variation of the defined studied variables. This way, the

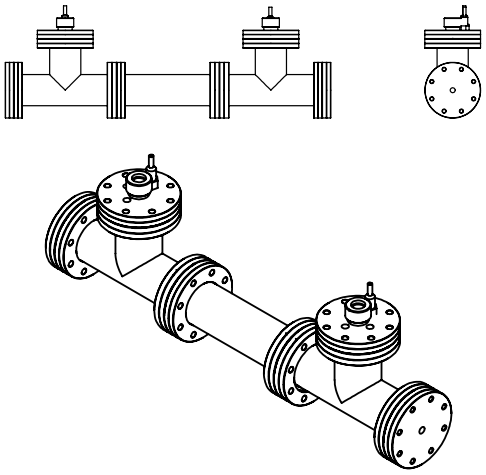

Figure 8.2.: Compact experimental set up proposed for the predictive model validation. Original from IQS designs.

oscillation proposed to test will consist in a sharp jump of concentration. Before the experiment starts, the whole set-up is taken to the design temperature. Then, a pure flux of Argon is released through the device ensuring all materials of the set-up are free of hydrogen. When the simulation begins, a concentration step of 3000 ppm is performed.

It has been computed that permeation rates of the large layout (at room temperature) are several orders of magnitude below the detection limit (below 0.01 ppm/h in the reactor volume). Therefore, this option is quite infeasible.

On the other hand, for the compact layout where temperatures can be hold high, all material considered seem to permeate faster despite the shorter pipe lengths. Figure 8.3 shows the results for steels options (304 and 316) in various lengths. The case of α-Fe outcomes can be found in Figure 8.4 and 75Pd-25Ag ones in Figure 8.5.

8.5. Proposed experiment

According with the results seen in previous section, it has bee decided to select the compact layout. The reason is that, as can be seen, temperature effects are much more important than the improvement achieved thanks to the increase in pipe area. Regarding the material, Stainless steels have shown the optimal permeation ratios at such conditions. 75Pd-25Ag permeation is forecast to be too fast (more than detectors response time) and get saturated in few seconds whereas for iron it is too slow. Since there are similar results between both types of steels, 304 is selected since it is easier to be shaped and cheaper.

However, as Figure 8.3b shows, no concentration difference is expected to be detected in the long run of the experiment. Only during the first minutes (while pipe walls are not saturated yet) it could be possible to detect some differences.

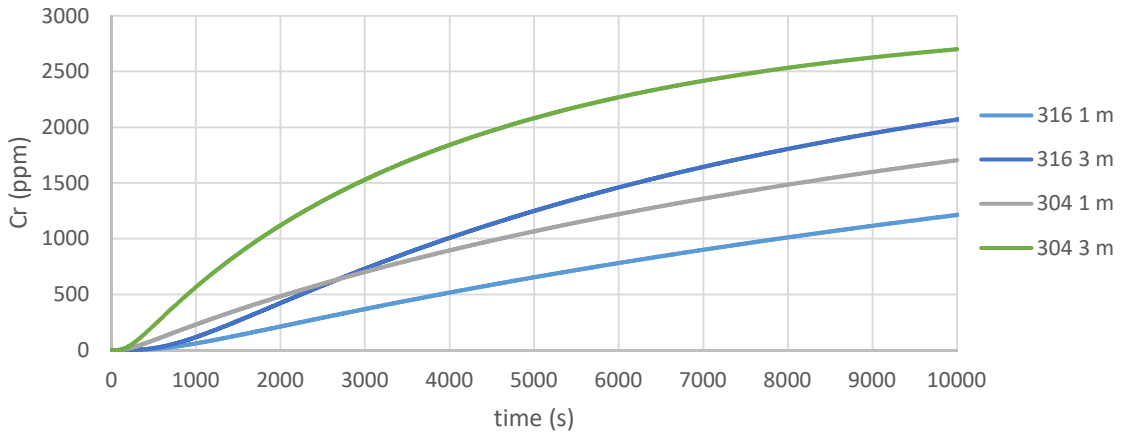

(a) Reactor volume hydrogen concentration (permeated) over time.

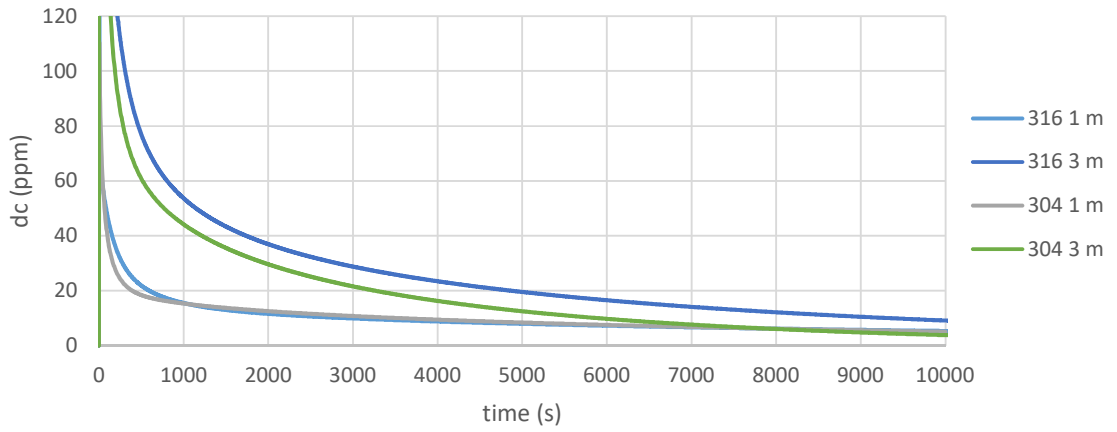

(b) Concentration difference between inlet and outlet.

Figure 8.3.: Compact layout stainless steel results for several lengths.

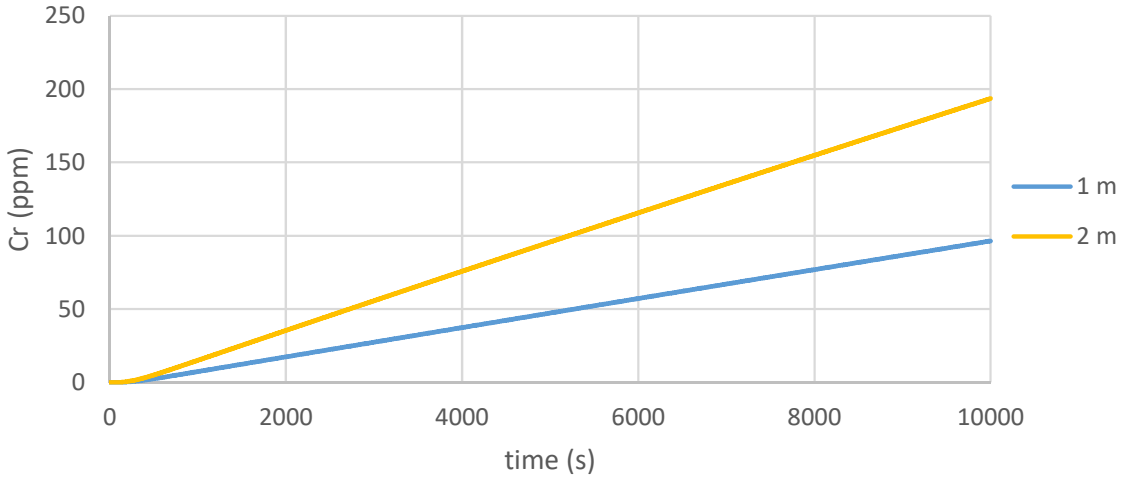

(a) Reactor volume hydrogen concentration (permeated) over time.

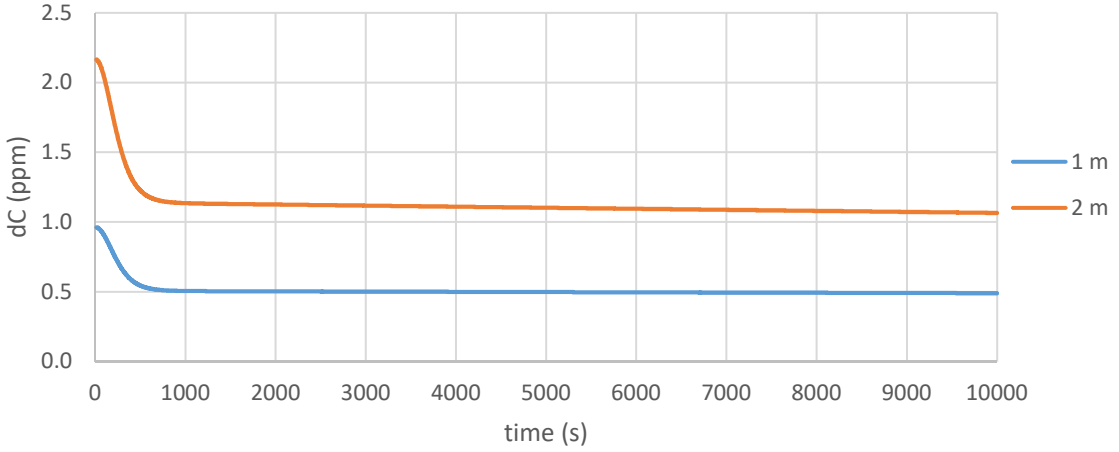

(b) Concentration difference between inlet and outlet.

Figure 8.4.: Compact layout α-Fe results for several lengths.

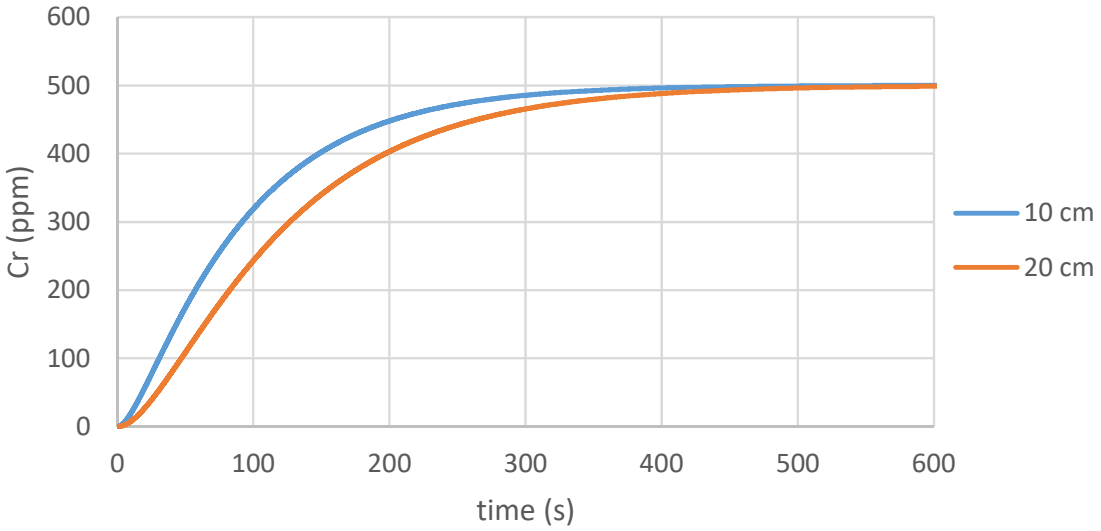

(a) Reactor volume hydrogen concentration (permeated) over time.

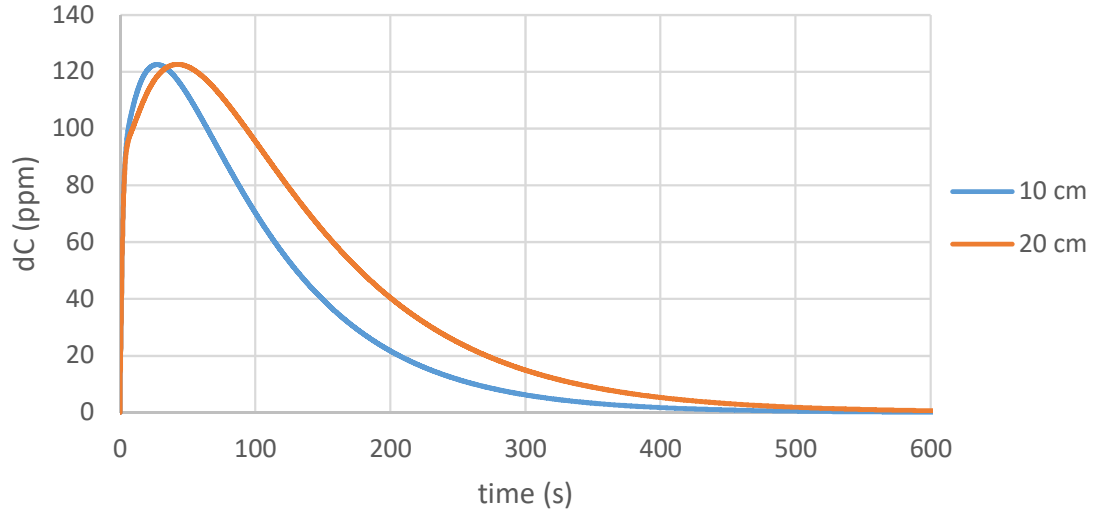

(b) Concentration difference between inlet and outlet.

Figure 8.5.: Compact layout 75Pd-25Ag results for several lengths.

9. Conclusions

Finally, in this last chapter, an analysis of the knowledge outcome produced in each of the main points of this work is made. Thus, achieved milestones regarding the predictive model, CPM and detector characterization issues are assessed. Moreover, other aspects of interest and future work paths are discussed as well.

9.1. Predictive model

It has been seen along this work the relevance of a good reality estimation via the predictive model. The proposed simplified 1.5D model rises up as an alternative to the highly computational costly CFD methods. Some of this technique avails can be highlighted:

- The code is way more faster than a CFD calculation, and achieves almost the same results. This makes feasible to compute up a relatively wide database of cases to train the transfer functions.
- Since the code has been developed from scratch, it is fully customizable and any change that would need to be done in future can be done relatively easy. Conversely, specific CFD solvers need to be developed for each case.
- The code has been developed so it could works as a post-processing tool for a hydraulic code. Therefore complex plant thermal-hydraulics can be solved first with a tested code such as RELAP5 [46] before running the code.

Nevertheless, some drawbacks of this tool has been identified during its developing. The main ones are listed below:

- The code, relies on kinetics parameters that are usually difficult to find if they have been measured and have lot of uncertainty depending on many unregistered factors.
- As a post-processing tool, the code requires lots of input information that may not be always available.

Nonetheless, the objectives of this tool has been successfully satisfied at this phase of the project. The code has shown to be mass conservative and therefore, the model precision relies on the transport properties supplied.

Moreover, the model has been designed to be modular, and therefore capable to cope with larger and quite complex systems as the ITER tritium plant ones. Hence, this tool represent an interesting approach to the whole plant simulation goal.

9.2. CPM

As it has been seen along this work, CPM have shown their capability for predicting inventories within simple systems. Among the advantages of these kind of models the most relevant are:

- They represent a very simple and quick way of computing inventories in real time. There is no need of powerful hardware to do so.
- Allows to predict upstream values easily simply by using forward in time expressions.
- Chapter 7 has shown that errors computed using these models are lower (two orders of magnitude) than the ones originated from the sensor itself. Moreover, it seems that such sensor intrinsic error has been mainly caused by uncertainties in the gas mixture (and hence, in the actual concentration that was input.)

However, this approach clearly shows some drawbacks too:

- It needs to be adjusted for every equilibrium point. So far it is possible to do so, but in future, temperature dependence must be taken in consideration as well. Hence, this will increase dramatically the number of previous calculations needed in order to fit the model parameters. Therefore, the model can only work within a predefined and limited range of situations.
- When a transient puts the system on a new steady state, some logic must be defined so that CPM parameters are reset to a new bunch calculated for the new equilibrium point.

All in all, the main objective of this study has been accomplished successfully as well. Inventory values have been predicted adequately. As a matter of fact, since the main source of error is the sensor itself, there is no concerns regarding the possibility of testing this predictive tools in larger and more complex systems. Indeed, next steps in this project will be aimed in such direction, testing CPM against more complex elements and layouts.

9.3. Sensor characterization tools

It has been seen how the proposed models for the sensor behaviour fits good enough with the real experiment to use them as a representation of the reality. Nevertheless, parameters obtained, such as the characteristic time, lack on precision due to the following aspects:

- The lack of more data makes the statistic results very poor in such way. Besides, more kind of perturbations should have been tested, such as down steps plus increasing and decreasing ramps. However, so far the IQS set up does not allow this kind of inputs.

- The reference concentration which is supposedly introduced in the system is not actually known. It has been demonstrated that read current data in the detector is also dependant of the total flow of gas. Since there are uncertainties on hydrogen valve opening, it can not be assured a constant mass flow. Hence, neither a precise input concentration can be assumed. This issue might explain the visible fluctuations in the concentration data measured even when steady state was reached.

- The mentioned oscillations also leads to a calibration standard deviation too high (26.1 ppm) to determine whether reference errors in steady state signals $o(c)$ are due to this uncertainties in the calibration value or caused by other reasons.

- Although it has been modelled adequately, the hysteresis behaviour of the sensor is quite strange and it has to be determined whether this noise is intrinsic of the probe or comes from other foreign reasons, such as a deficient electrical connections or, most likely, analogical to digital converter. Since a post-processing algorithm to correct this errors is developed and explained in section 6.4.1, this noise has not been considered any further in this work.

Regarding the sensor predictive tools developed, as it has been seen in the previous experiences, the they perform as expected. Predictions made over simulated sensor data are quite accurate. However, when applied to reality, many other fluctuations take place as well. Nevertheless, the tools have shown the feasibility to estimate concentration values from the sensor output and therefore quicken the acknowledgement of a change in the system conditions.

On the other hand, this preliminary work with experimental data has shown that emphasis must be put in controlling on a much accurate way the gas mixture and the mass flow inserted in the reactor in order to asses the real precision of the sensor. In addition, an effort must be put as well in finding the root cause of the signal hysteresis like noise that this work coped with.

All in all, there is still a lot to improvement on these tools. Firstly, physics of the sensor dynamics must be studied deeper, so as to understand each components of its characteristic time and develop more detailed tools. Additionally, there is work to do at improving signal quality as well, since the source of the hysteresis noise found is still unknown. However, this experience allows to understand the order of magnitude of parameters used to feed this CPM feasibility analysis.

9.4. Project budget

As a theoretical and data analysis research project, the necessary means to carry out this job has been a computer. Since all the software used has been free source codes, no licenses has been needed.

This project is part of the numerical tools development area of the ANT research group at UPC. As commented, since all the IT resources has been free source codes, no

Table 9.1.: Summary of the total project budget.

Description	Units	Unitary cost	Total
Manpower hours	900 h	8 €/h	7200 €
IRPF (2 %)	-	-	144 €
PC hours	270 kWh	0.14 €/kWh	37.8 €
OpenFoam license	1	0	0 €
Python license	1	0	0 €
Total			7381.8 €

cost has been derived from this part. Therefore, only electricity costs and manpower cost are derived from this project. Table 9.1 shows the total budget of this project.

For this project, it has been estimated a total amount of 900 working hours. Regarding the manpower costs, the scholarship holder wage is set up to 8 €/h. Electricity cost is computed assuming a power consumption of 300 W for the computer and an average electricity cost of 0.14 €/kWh.

9.5. Environmental impact study of the work

As commented in section 2.4, the control of tritium inventory as a mayor security issue. This is due to the fact that tritium permeation capacity is very high, as discussed in chapter 3. That is why the development of inventory prediction tool as the one discussed along this work are so relevant for radiation protection purposes.

In the present work, the only component analysed is the piping systems. This is just one element among the complexity of the tritium plant described in section 2.2. That is why the quantification of tritium leakages of ITER is far beyond the scope of this work. However one the whole project in which this work is framed in will be developed, a good estimation of such releases could be performed.

Regarding the impact of developing this work, only computer aid has been necessary. Therefore, the only impact to the environment has been the CO_2 emissions derived from the electricity consumption. According to [47], an average conversion factor of 298 g_{CO_2}/KWh can be applied to the electrical consumption shown in Table 9.1 in order to estimate the amount of carbon dioxide released to te environment. The value obtained has been 80.46kg_{CO_2}. Of course, many other consumptions could be considered as well, such as all related to the UPC building where this job has been carried out. Nonetheless, since those consumptions are independent of this work activity development, it has been decided not to include them.

9.6. Future research

Although the objectives of this first phase of the project have been accomplished, there are many issues remaining for the following stages:

- The priority next step is to validate the predictive detailed code in depth. First, pipe element outcomes should match with the proposed experiment results (see chapter 8). Then, getter systems are proposed as the following ones to be tested with future new test set-ups.
- Develop a large CPM database using predictive model calculations. Besides concentration, variations of mass flow, temperature and pressure may be considered as well. New CPMs might be needed to be built so they could cover the variation of such parameters. MISO (Multiple Input Single Output) transfer functions might be developed for such purpose.
- Design the CPM database strategy, consisting in the logics that should determine when a CPM function has reach a new stationary point in which new parameters are set automatically.
- Deeper understanding of the sensor, such as the dependences with mass flows and any other non trivial dependency.
- Finally, once the previous steps are accomplished, the final aim is to start simulating real plant systems and develop the proper CPM to predict on-line inventories of the whole plant.

Bibliography

[1] BP, "BP Statistical Review of World Energy 2017," Tech. Rep. 66, British Petroleum, 2017.

[2] Python Fundation Software, "Python 3.6," 2018.

[3] C. J. Greenshields, "OpenFOAM User Guide," tech. rep., OpenFOAM Foundation Ltd, 2015.

[4] E. Mas de les Valls and L. Batet, "Hydrogen transport in a TES pipe as applied to HCPB design CFD analysis," Tech. Rep. 1, Universitat Politècnica de Catalunya, 2017.

[5] J. Juba, "NRL Plasma Formulary," tech. rep., Naval Research Laboratory, Washington, DC, 2013.

[6] J. D. Lawson, "Some Criteria for a Power Producing Thermonuclear Reactor," *Proceedings of the Physical Society. Section B*, vol. 70, no. 1, pp. 6–10, 1957.

[7] Max Planck Institute of Plasma Physics, "Wendelstein Stellarator," 2018.

[8] ITER Organization, "ITER," 2018.

[9] M. Cavinato, "Operation and control of the ITER Tokamak," in *Master's Fusion Lectures*, (Barcelona), 2017.

[10] G. Rampal, A. Li Puma, Y. Poitevin, E. Rigal, J. Szczepanski, and C. Boudot, "HCLL TBM for ITER-design studies," *Fusion Engineering and Design*, vol. 75-79, pp. 917–922, 2005.

[11] F. Cismondi, S. Kecskés, M. Ilic, G. Légrádi, B. Kiss, O. Bitz, B. Dolensky, H. Neuberger, L. V. Boccaccini, and T. Ihli, "Design update, thermal and fluid dynamic analyses of the EU-HCPB TBM in vertical arrangement," *Fusion Engineering and Design*, vol. 84, no. 2-6, pp. 607–612, 2009.

[12] J. D. B. Jr, R. H. Clarke, C. Cousins, A. J. Gonza, J. Lee, B. Lindell, Y. Sasaki, C. B. Meinhold, N. Shandala, W. K. Sinclair, C. Streffer, A. Sugier, Z. Pan, R. J. Pentreath, R. J. Preston, R. M. Alexakhin, C. Cousins, B. Aires, A. J. Gonza, H. Menzel, R. J. Pentreath, N. Shandala, P. Burns, J. Cooper, B. C. Winkler, S. Africa, R. Cox, R. J. Preston, C. Streffer, J. Valentin, R. H. Clarke, and G. J. Dicus, "The 2007 Recommendations of the International Commission on Radiological Protection," tech. rep., Health Protection Agency, 2007.

[13] D. Murdoch, I. R. Cristescu, and R. Lässer, "Strategy for determination of ITER in-vessel tritium inventory," *Fusion Engineering and Design*, vol. 75-79, pp. 667–671, 2005.

[14] I. Peñalva, *Influencia de los componentes metalúrgicos C, Cr y P en la permebilidad del hidrógeno para aleaciones férreas*. PhD thesis, Universidad del País Vasco, 2017.

[15] F. Waelbroeck, P. Wienhold, and K. Jülich, *Influence of Bulk and Surface Phenomena on the Hydrogen Permeation Through Metals*. Berichte der Kernforschungsanlage Jülich, Kernforschungsanlage Jülich, Institute für Plasmaphysik, 1984.

[16] E. A. Mason and B. Kronstadt, "Graham's Laws of diffusion and effusion," *Journal of Chemical Education*, vol. 44, no. 12, p. 740, 1967.

[17] G. Esteban, *Cinética de los Isótopos del Hidrógeno en Materiales de Interés para la Tecnología de Reactores de Fusión*. PhD thesis, Universidad del País Vasco, 2002.

[18] A.V. Ostapov, "Hydrogen in Zirconium," *Journal of Chemical Education*, vol. 37, no. 10, pp. 533–536, 2013.

[19] M. Gambini, M. Manno, and M. Vellini, "Numerical analysis and performance assessment of metal hydride-based hydrogen storage systems," *International Journal of Hydrogen Energy*, vol. 33, no. 21, pp. 6178–6187, 2008.

[20] K. B. Minko, V. I. Artemov, and G. G. Yan'Kov, "Numerical simulation of sorption/desorption processes in metal-hydride systems for hydrogen storage and purification. Part I: Development of a mathematical model," *International Journal of Heat and Mass Transfer*, vol. 68, pp. 683–692, 2014.

[21] A. Freni, F. Cipitì, and G. Cacciola, "Finite element-based simulation of a metal hydride-based hydrogen storage tank," *International Journal of Hydrogen Energy*, vol. 34, no. 20, pp. 8574–8582, 2009.

[22] C. A. Chung and C. J. Ho, "Thermal-fluid behavior of the hydriding and dehydriding processes in a metal hydride hydrogen storage canister," *International Journal of Hydrogen Energy*, vol. 34, no. 10, pp. 4351–4364, 2009.

[23] D. M. Grant, D. L. Cummings, and D. A. Blackburn, "Hydrogen in 304 Steel - Diffusion, Permeation and Surface-Reaction," *Journal of Nuclear Materials*, vol. 149, no. 2, pp. 180–191, 1987.

[24] D. M. Grant, "Hydrogen in 316 Steel - Diffusion, permeation and surface reaction," *Analysis*, vol. 152, pp. 139–145, 1988.

[25] S. K. Lee, S. H. Yun, H. G. Joo, and S. J. Noh, "Deuterium transport and isotope effects in type 316L stainless steel at high temperatures for nuclear fusion and nuclear hydrogen technology applications," *Current Applied Physics*, vol. 14, no. 10, pp. 1385–1388, 2014.

[26] M. Sugisaki, H. Furuya, K. Ono, and K. Idemitsu, "Tritium solubility in SUS-316 stainless steel," *Journal of Nuclear Materials*, vol. 120, no. 1, pp. 36–40, 1984.

[27] E. Serra and A. Perujo, "Influence of the surface conditions on permeation in the deuterium-MANET system," *Journal of Nuclear Materials*, vol. 240, no. 3, pp. 215–220, 1997.

[28] K. S. Forcey, I. Iordanova, and M. Yaneva, "The diffusivity and solubility of deuterium in a high chromium martensitic steel," *Journal of Nuclear Materials*, vol. 240, no. 2, pp. 118–123, 1997.

[29] E. Serra, G. Benamati, and O. Ogorodnikova, "Hydrogen isotopes transport parameters in fusion reactor materials," *Journal of Nuclear Materials*, vol. 255, no. 2-3, pp. 105–115, 1998.

[30] G. A. Esteban, A. Perujo, K. Douglas, and L. A. Sedano, "Tritium diffusive transport parameters and trapping effects in the reduced activating martensitic steel OPTIFER-IVb," *Journal of Nuclear Materials*, vol. 281, no. 1, pp. 34–41, 2000.

[31] G. A. Esteban, A. Peña, F. Legarda, and R. Lindau, "Hydrogen transport and trapping in ODS-EUROFER," *Fusion Engineering and Design*, vol. 82, no. 15-24, pp. 2634–2640, 2007.

[32] G. A. Esteban, A. Peña, I. Urra, F. Legarda, and B. Riccardi, "Hydrogen transport and trapping in EUROFER'97," *Journal of Nuclear Materials*, vol. 367-370 A, no. SPEC. ISS., pp. 473–477, 2007.

[33] F. Reiter, K. S. Forcey, and G. Gervasini, *A compilation of tritium-material interaction parameters in fusion reactor materials*. Commission of the European Communities, 1993.

[34] I. Ricapito, A. Aiello, A. Bükki-Deme, J. Galabert, C. Moreno, Y. Poitevin, D. Radloff, A. Rueda, A. Tincani, and M. Utili, "Tritium technologies and transport modelling: Main outcomes from the European TBM Project," *Fusion Engineering and Design*, no. January, pp. 1–7, 2018.

[35] A. Perujo, K. Douglas, and E. Serra, "Low pressure tritium interaction with inconel 625 and AISI 316 L stainless steel surfaces: An evaluation of the recombination and adsorption constants," *Fusion Engineering and Design*, vol. 31, no. 2, pp. 101–108, 1996.

[36] E. Serra, A. Perujo, and G. Benamati, "Influence of traps on the deuterium behaviour in the low activation martensitic steels F82H and Batman," *Journal of Nuclear Materials*, vol. 245, no. 2-3, pp. 108–114, 1997.

[37] E. Serra and A. Perujo, "The surface rate constants of deuterium in the martensitic steel DIN 1.4914 (MANET)," *Journal of Nuclear Materials*, vol. 223, no. 2, pp. 157–162, 1995.

[38] L. Batet, "H2, HT and T2 transport in a gas pipe," tech. rep., Universitat Politècnica de Catalunya, 2017.

[39] B. C. Kuo, *Sistemas de control automatico*. Prentice Hall, 1996.

[40] K. Ogata, *Ingeniería de Control Moderna*. Prentice Hall, 2013.

[41] J. A. Nelder and R. Mead, "A Simplex Method for Function Minimization," *The Computer Journal*, vol. 7, pp. 308–313, jan 1965.

[42] J. Abella, "Diseño y construcción de un sistema experimental de ensayos para sensores de hidrógeno para metales fundidos," tech. rep., Instituto Químico de Sarrià, 2017.

[43] A. V. Oppenheim and A. S. Willsky, *Signals and Systems*. Prentice Hall, 1997.

[44] B. Widrow and E. Walach, *Adaptive Inverse Control*. IEEE Press Series on Power Engineering, Hoboken, NJ, USA: John Wiley & Sons, Inc., 2007.

[45] Mathworks, "Matlab Simulink User's Guide," tech. rep., Mathworks, Natick, 2015.

[46] Idaho National Laboratoy, "RELAP5-3D," 1980.

[47] UNESA, "Estimación de las emisiones de CO2 en la prodcción de electricidad en España," tech. rep., UNESA, Madrid, 2015.

List of Figures

1.1. Reactivity rate comparison between the three most suitable fusion reactions as a function of temperature. . . . 2
1.2. Wendelstein 7-X Stellarator. . . . 3
1.3. ITER main components. . . . 5
1.4. CAD representations of some ITER main parts. . . . 6
1.5. Example of plasma shot designed for ITER operation. . . . 7

2.1. Simplified Sankey diagram of the neutron-tritium cycle. . . . 10
2.2. Simplified scheme of a closed loop tritium plant system. . . . 11
2.3. Scheme of an European HCLL-TBM design. . . . 13
2.4. Scheme of an European HCPB-TBM design. . . . 14

3.1. Summary of all the possible phenomena over a metallic surface. . . . 20
3.2. Schematic isothermal pressure–composition hysteresis loop. . . . 23
3.3. Pressure Concentration Temperature plot and Van't Hoff plot. . . . 24

4.1. Proposed work flow for the transport code. . . . 27
4.2. Pipe discretization scheme. . . . 28
4.3. Pebble discretization scheme. . . . 32

5.1. Overall scheme of how CPM are used to predict the target variables for a pipe system. . . . 35
5.2. Geometrical distribution of the CPM test case system. . . . 36
5.3. Outlet and inlet concentration values during a transient where a step-shaped perturbation inputs the system. . . . 37
5.4. Examples of step-shaped concentration perturbations introduced over the reference point shown in Table 5.1. . . . 43
5.5. Example of second order polynomial fitting over some CPM parameters (wall inventory). . . . 43

6.1. Probe signal simulation process. . . . 45
6.2. Simplified diagram showing how the IQS tested sensor works. . . . 46
6.3. Experimental set up used to continuous data acquisition. . . . 47
6.4. Scheme with the shape and size of the reactor used in the experiment. . . . 48
6.5. Probe calibration curve fitted by steady state measures. . . . 49
6.6. Measurements recorded in the IQS experiment used for determine the time constant of the detector. . . . 50

6.7. Correlations between current measured and mass flow for steady state points. 50
6.8. Example of the step from 1208 to 1333 ppm and its fitted curve. 52
6.9. Gaussian distribution of the sensor concentration error. 54
6.10. Comparison between real data and simulated noised data. 55
6.11. Example of the hysteresis corrector algorithm applied to experimental data records. 55
6.12. Comparison of the influence of the filter order for the same cut-off frequency. 56
6.13. Comparison of the most commonly used FIR filter responses. 57
6.14. Example of filter group delay and its correction using double (forward and backward) filtering technique. 58
6.15. Simulation of the sensor response calculated over the simulated model outcome. 61
6.16. Signal treatment applied to experimental data. 61

7.1. Different CPM estimations compared with the simulated values. 65
7.2. Relative error between virtual model outcome and CPM prediction. 65

8.1. Large experimental set up proposed for the predictive model validation. . 69
8.2. Compact experimental set up proposed for the predictive model validation. 70
8.3. Compact layout stainless steel results for several lengths. 71
8.4. Compact layout α-Fe results for several lengths. 72
8.5. Compact layout 75Pd-25Ag results for several lengths. 73

C.1. Argon temperature evolution in the experimental set up pipe. 112

List of Tables

2.1. Summary of tritium inventories allowed for ITER design. 16

3.1. Summary table of the transport parameter coefficient data for the main materials of interest. 26
3.2. Summary table of the superficial kinetic parameter data for the main materials of interest. 26

5.1. Main parameters for the CPM test case system. 36
5.2. Coefficients for CPM parameters computation. Inlet concentration (as function of probe concentration), outlet concentration and gas inventory are shown. 42
5.3. Coefficients for CPM parameters computation. Wall inventory and room concentration are shown. 43

6.1. Sensor characteristic parameter values obtained from the analysed data. . 52
6.2. Concentration perturbation input function used for the 1.5D simulation. . 60

7.1. Global measurement error, statistical error associated with the use of estimation tool and calculated value of the intrinsic sensor error. 66

8.1. Experimental set up design options considered. 68

9.1. Summary of the total project budget. 78

A.1. Used nomenclature and its units. 92
A.2. Upper and lower index used. 93

Appendices

A. Nomenclature and Glossary

In this appendix nomenclature used along this work is shown. Corresponding units are indicated as well (SI unit system has been used whenever possible). Magnitude definitions is defined in Table A.1 whereas upper and lower sub-index are summarized in table Table A.2. The acronyms used along this work are shown below:

- ALARA: As Low As Reasonable Achievable. The ALARA radiation safety principle is based on the minimization of radiation doses and limiting the release of radioactive materials into the environment by employing all "reasonable methods".
- ANT: Advance Nuclear Technologies. Research group at UPC.
- CPM: Concentrated Parameters Model. Proposed transfer function model to be implemented in the CODAC system.
- BCC: Body-Centered Cubic: A cubic crystal system where there is an atom in the middle of the cubic unit cell.
- CODAC: Control, Data Access and Communication. ITER control system.
- DEMO: DEMOstration fusion plant. Proposed commercial fusion plant which would demonstrate the economical feasibility of fusion reactors.
- ELM: Edge Localized Mode. It is a disruptive instability occurring in the edge region of a tokamak plasma.
- ICRP: International Commission on Radiological Protection.
- IQS: Sarrià Chemical Institute.
- ITER: International Thermonuclear Experimental Reactor.
- PTC: Pressure Composition Temperature. Curve used for computing equilibrium pressure in ZrCo hydrogen storage systems.
- TBM: Test Blanked Module. Plasma facing modules which would produce the tritium for the reactor and would be tested in ITER.
- TOKAMAK: TOroidal CAmera MAgnetic Coils (translated from Russian).
- UPC: Polithecnical University of Catalonia.

Table A.1.: Used nomenclature and its units.

Parameter	Units	Description
α	$-$	Numerical zero
c	mol/m^3	Concentration
$C(s)$	$-$	Concentration (complex variable)
d	m	Diameter
D	m^2/s	Diffusivity
f	Hz	Frequency
e	m	Thickness
k	$-$	Coefficient/Constant
L	m	Length
n	mol	Hydrogen inventory
N	$-$	Number
o	$-$	Error (uncertainty)
ω	rad/s	Frequency (radians)
p	Pa	Pressure
ρ	kg/m^3	Density
Φ	$mol/msPa$	Permeability
r	m	Radius
t	s	Time
T	K	Temperature
τ	s	Delay or advancement
ξ	$-$	Reaction rate constant
ζ	$-$	Damping ratio
θ	rad	Phase
v	m/s	Fluid velocity
V	m^3	Volume

Table A.2.: Upper and lower index used.

Index	Description
0	Initial
$*$	Reference
a	Absorption
CPM	Calculated using CPM tool
d	Dissociation
de	Desorption
eq	Equilibrium
f	Filter
g	Gas
H_2	Hydrogen (molecular)
H	Hydrogen (atomic)
HT	Hydrogen-Tritium molecule
i	Inner
in	Inlet
out	Outlet
n	Noise
o	Outer
Q	Any hydrogen specie
r	Recombination
R	Room
Recir	Recirculation
s	Sensor
S	Sievert's
tot	Total
T_2	Tritium (molecular)
T	Tritium (atomic)
v	Reactor volume
w	Wall
$\dot{x}$	Amount of x per unit time
$\bar{x}$	Mean amount of de x

B. Model equations

Model used to estimate the spread out of hydrogen over the system is described in chapter 4. The equations to solve can be written in a matricial form. Depending on the system to model, the set of equations will vary, yet the same notation is used.

$$[A]\{C\} = \{B\} \tag{B.1}$$

B.1. Pipe

In this case, extracted from [38], the unknown concentrations are:

$$\{C\}^T = \left\{ C_{H_2}, C_{T_2}, C_{HT}, C_H^w, C_T^w, C_H^1, \cdots, C_H^n, C_T^1, \cdots, C_T^n, C_H^o, C_T^o \right\}$$

B.1.1. Constant matrix $[A]$ terms

The $a_{i,j}$ terms being zero, except the following:

Balance to H_2 gas

$$a_{0,0} = 1 + \frac{2}{r_{in}} k_{d,H_2} RT\Delta t$$

$$a_{0,3} = -\frac{2}{r_{in}} 2k_{r,H_2} C_{H,i}^{w,0} \Delta t$$

Balance to T_2 gas

$$a_{1,1} = 1 + \frac{2}{r_{in}} k_{d,T_2} RT\Delta t$$

$$a_{1,4} = -\frac{2}{r_{in}} 2k_{r,T_2} C_{T,i}^{w,0} \Delta t$$

B.1.2. Balance to HT gas

$$a_{2,2} = 1 + \frac{2}{r_{in}} k_{d,HT} RT\Delta t$$

$$a_{2,3} = -\frac{2}{r_{in}} k_{r,HT} C_{T,i}^{w,0} \Delta t$$

$$a_{2,4} = -\frac{2}{r_{in}} k_{r,HT} C_{H,i}^{w,0} \Delta t$$

Balance to H at inner wall surface

$$a_{3,0} = -2k_{d,H_2} RT$$
$$a_{3,2} = -k_{d,HT} RT$$
$$a_{3,3} = 4k_{r,H_2} C_{H,i}^{w,0} + k_{r,HT} C_{T,i}^{w,0} + \frac{2D_H}{\Delta r}$$
$$a_{3,4} = k_{r,HT} C_{H,i}^{w,0}$$
$$a_{3,5} = -\frac{2D_H}{\Delta r}$$

Balance to T at inner wall surface

$$a_{4,1} = -2k_{d,T_2} RT$$
$$a_{4,2} = -k_{d,HT} RT$$
$$a_{4,3} = k_{r,HT} C_{T,i}^{w,0}$$
$$a_{4,4} = 4k_{r,T_2} C_{T,i}^{w,0} + k_{r,HT} C_{H,i}^{w,0} + \frac{2D_T}{\Delta r}$$
$$a_{4,n+5} = -\frac{2D_T}{\Delta r}$$

H diffusion inside the wall

$$a_{5,3} = -\frac{2r_{in} D_H}{\Delta r} \Delta t$$
$$a_{5,5} = \left(r_{in} + \frac{\Delta r}{2} \right) \Delta r + \frac{2r_{in} D_H}{\Delta r} \Delta t + \frac{(r_{in} + \Delta r) D_H}{\Delta r} \Delta t$$
$$a_{5,6} = -\frac{(r_{in} + \Delta r) D_H}{\Delta r} \Delta t$$
$$a_{j+4,j+3} = -\frac{(r_{in} + (j-1)\Delta r)\, D_H}{\Delta r} \Delta t$$
$$a_{j+4,j+4} = (r_{in} + (j - 1/2)\Delta r)\, \Delta r + \frac{(r_{in} + (j-1)\Delta r)\, D_H}{\Delta r} \Delta t + \frac{(r_{in} + j\Delta r)\, D_H}{\Delta r} \Delta t$$
$$a_{j+4,j+5} = -\frac{(r_{in} + j\Delta r)\, D_H}{\Delta r} \Delta t$$

$$a_{n+4,n+3} = -\frac{(r_{out} - \Delta r)\, D_H}{\Delta r} \Delta t$$

$$a_{n+4,n+4} = (r_{out} - 1/2\Delta r)\,\Delta r + \frac{(r_{out} - \Delta r)\,D_H}{\Delta r}\Delta t + \frac{2r_{out}D_H}{\Delta r}\Delta t$$

$$a_{n+4,2n+5} = -\frac{2r_{out}D_H}{\Delta r}\Delta t$$

$$a_{n+5,4} = -\frac{2r_{in}D_T}{\Delta r}\Delta t$$

T diffusion inside the wall

$$a_{n+5,n+5} = \left(r_{in} + \frac{\Delta r}{2}\right)\Delta r + \frac{2r_{in}D_T}{\Delta r}\Delta t + \frac{(r_{in} + \Delta r)D_T}{\Delta r}\Delta t$$

$$a_{n+5,n+6} = -\frac{(r_{in} + \Delta r)D_T}{\Delta r}\Delta t$$

$$a_{n+j+4,n+j+3} = -\frac{(r_{in} + (j-1)\Delta r)\,D_T}{\Delta r}\Delta t$$

$$a_{n+j+4,n+j+4} = (r_{in} + (j-1/2)\Delta r)\,\Delta r + \frac{(r_{in} + (j-1)\Delta r)\,D_T}{\Delta r}\Delta t + \frac{(r_{in} + j\Delta r)\,D_T}{\Delta r}\Delta t$$

$$a_{n+j+4,n+j+5} = -\frac{(r_{in} + j\Delta r)\,D_T}{\Delta r}\Delta t$$

$$a_{2n+4,2n+3} = -\frac{(r_{out} - \Delta r)\,D_T}{\Delta r}\Delta t$$

$$a_{2n+4,2n+4} = (r_{out} - 1/2\Delta r)\,\Delta r + \frac{(r_{out} - \Delta r)\,D_T}{\Delta r}\Delta t + \frac{2r_{out}D_T}{\Delta r}\Delta t$$

$$a_{2n+4,2n+6} = -\frac{2r_{out}D_T}{\Delta r}\Delta t$$

Balance to H at outer wall surface

$$a_{2n+5,n+4} = -\frac{2D_H}{\Delta r}$$

$$a_{2n+5,2n+5} = 4k^o_{r,H_2}C^{o,0}_{H,i} + k^o_{r,HT}C^{o,0}_{T,i} + \frac{2D_H}{\Delta r}$$

$$a_{2n+5,2n+6} = k^o_{r,HT}C^{o,0}_{H,i}$$

Balance to T at outer wall surface

$$a_{2n+6,2n+4} = -\frac{2D_T}{\Delta r}$$

$$a_{2n+6,2n+5} = k^o_{r,HT}C^{o,0}_{T,i}$$

$$a_{2n+6,2n+6} = 4k^o_{r,T_2}C^{o,0}_{T,i} + k^o_{r,HT}C^{o,0}_{H,i} + \frac{2D_T}{\Delta r}$$

B.1.3. Independent terms matrix [B]

Balance to H_2 gas

$$b_0 = C^0_{H_2,i} + \left[D_{H_2,i-1/2} \left(\frac{C^0_{H_2,i-1} - C^0_{H_2,i}}{\Delta x^2} \right) - D_{H_2,i+1/2} \left(\frac{C^0_{H_2,i} - C^0_{H_2,i+1}}{\Delta x^2} \right) + \frac{\nu_{i-1/2} C^0_{H_2,i-1} - \nu_{i+1/2} C^0_{H_2,i}}{\Delta x} - \frac{2}{r_{in}} k_{r,H_2} \left(C^{w,0}_{H,i} \right)^2 \right] \Delta t$$

Balance to T_2 gas

$$b_1 = C^0_{T_2,i} + \left[D_{T_2,i-1/2} \left(\frac{C^0_{T_2,i-1} - C^0_{T_2,i}}{\Delta x^2} \right) - D_{T_2,i+1/2} \left(\frac{C^0_{T_2,i} - C^0_{T_2,i+1}}{\Delta x^2} \right) + \frac{\nu_{i-1/2} C^0_{T_2,i-1} - \nu_{i+1/2} C^0_{T_2,i}}{\Delta x} - \frac{2}{r_{in}} k_{r,T_2} \left(C^{w,0}_{T,i} \right)^2 \right] \Delta t$$

Balance to HT gas

$$b_2 = C^0_{HT,i} + \left[D_{HT,i-1/2} \left(\frac{C^0_{HT,i-1} - C^0_{HT,i}}{\Delta x^2} \right) - D_{HT,i+1/2} \left(\frac{C^0_{HT,i} - C^0_{HT,i+1}}{\Delta x^2} \right) + \frac{\nu_{i-1/2} C^0_{HT,i-1} - \nu_{i+1/2} C^0_{HT,i}}{\Delta x} - \frac{2}{r_{in}} k_{r,HT} C^{w,0}_{H,i} C^{w,0}_{T,i} \right] \Delta t$$

Balance to H at inner wall surface

$$b_3 = 2k_{r,H_2} \left(C^{w,0}_{H,i} \right)^2 + k_{r,HT} C^{w,0}_{H,i} C^{w,0}_{T,i}$$

Balance to T at inner wall surface

$$b_4 = 2k_{r,T_2} \left(C^{w,0}_{T,i} \right)^2 + k_{r,HT} C^{w,0}_{H,i} C^{w,0}_{T,i}$$

H diffusion inside the wall

For the first layer (inner) where $j = 1$:

$$b_5 = \left(r_{in} + \frac{\Delta r}{2} \right) \Delta r C^{1,0}_{H,i}$$

For the j layer (intermediate):

$$b_{j+4} = (r_{in} + (j - 1/2)\Delta r)\,\Delta r C^{j,0}_{H,i} \qquad j = 2, ..., n-1$$

for the last layer (outer):

$$b_{n+4} = (r_{out} - 1/2\Delta r)\,\Delta r C^{n,0}_{H,i}$$

T diffusion inside the wall

For the first layer (inner) where $j = 1$:

$$b_{n+5} = \left(r_{in} + \frac{\Delta r}{2}\right)\Delta r C^{1,0}_{T,i}$$

For the j layer (intermediate):

$$b_{n+j+4} = (r_{in} + (j - 1/2)\Delta r)\,\Delta r C^{j,0}_{T,i} \qquad j = 2, ..., n-1$$

For the last layer (outer):

$$b_{2n+4} = (r_{out} - 1/2\Delta r)\,\Delta r C^{n,0}_{T,i}$$

Balance to H at outer wall surface

$$b_{2n+5} = 2k^{o}_{r,H_2}\left(C^{o,0}_{H,i}\right)^2 + k^{o}_{r,HT}C^{o,0}_{H,i}C^{o,0}_{T,i} + 2k^{o}_{d,H_2}P^{o,0}_{H_2} + k^{o}_{d,HT}P^{o,0}_{HT}$$

Balance to T at outer wall surface

$$b_{2n+6} = 2k^{o}_{r,T_2}\left(C^{o,0}_{T,i}\right)^2 + k^{o}_{r,HT}C^{o,0}_{H,i}C^{o,0}_{T,i} + 2k^{o}_{d,T_2}P^{o,0}_{T_2} + k^{o}_{d,HT}P^{o,0}_{HT}$$

B.2. Getter

This model is based on the pipe one, however new terms are modified or introduced. The wall terms commonly use for the pipe case are now shown here but are present in both matrices [A] and [B].

B.2.1. Constant matrix [A] terms

The new non zero terms of [A] matrix are shown below. In order to simplify notation, the beginning position of the pebble concentrations is defined as $pb^0 \equiv 7+2N^{lw}$.

Balance to H_2 gas

$$a_{0,0} = Vol_i + A^w k^w_{d,H_2} RT\Delta t +$$

$$+\left\{\begin{array}{l} N^p A^p k^p_{d,H_2} RT\Delta t \quad C^{n-1}_{Qtot} < C_{min} \\ \left\{\begin{array}{ll} N^p A^p K_a e^{-\frac{E_a}{RT}} f^{a,n-1}_{H_2} \Delta t \frac{C_{max}-C^{n-1}_{Qtot}}{C^{n-1}_{Q_2 tot}} & p > p^a_{eq} \\ 0 & p^d_{eq} < p < p^a_{eq} \\ N^p A^p K_d e^{-\frac{E_d}{RT}} f^{d,n-1}_{H_2} RT\Delta t \frac{C^{n-1}_{Qtot}-C_{min}}{p_{eq}} & p < p^d_{eq} \end{array}\right. \quad C^{n-1}_{Qtot} > C_{min} \end{array}\right.$$

$$a_{0,1} = \left\{\begin{array}{l} 0 \quad C^{n-1}_{Qtot} < C_{min} \\ \left\{\begin{array}{ll} N^p A^p K_a e^{-\frac{E_a}{RT}} f^{a,n-1}_{H_2} \Delta t \frac{C_{max}-C^{n-1}_{Qtot}}{C^{n-1}_{Q_2 tot}} & p > p^a_{eq} \\ 0 & p^d_{eq} < p < p^a_{eq} \\ N^p A^p K_d e^{-\frac{E_d}{RT}} f^{d,n-1}_{H_2} RT\Delta t \frac{C^{n-1}_{Qtot}-C_{min}}{p_{eq}} & p < p^d_{eq} \end{array}\right. \quad C^{n-1}_{Qtot} > C_{min} \end{array}\right.$$

$$a_{0,2} = \left\{\begin{array}{l} 0 \quad C^{n-1}_{Qtot} < C_{min} \\ \left\{\begin{array}{ll} N^p A^p K_a e^{-\frac{E_a}{RT}} f^{a,n-1}_{H_2} \Delta t \frac{C_{max}-C^{n-1}_{Qtot}}{C^{n-1}_{Q_2 tot}} & p > p^a_{eq} \\ 0 & p^d_{eq} < p < p^a_{eq} \\ N^p A^p K_d e^{-\frac{E_d}{RT}} f^{d,n-1}_{H_2} RT\Delta t \frac{C^{n-1}_{Qtot}-C_{min}}{p_{eq}} & p < p^d_{eq} \end{array}\right. \quad C^{n-1}_{Qtot} > C_{min} \end{array}\right.$$

$$a_{0,3} = -2K^w_{r,H_2} C^{w,n-1}_H \Delta t$$

$$a_{0,pb^0+1} = \left\{\begin{array}{l} -2N^p A^p K^p_{r,H_2} C^{sp,n-1}_H \Delta t \quad C^{n-1}_{Qtot} < C_{min} \\ \left\{\begin{array}{ll} N^p A^p K_a e^{-\frac{E_a}{RT}} f^{a,n-1}_{H_2} \Delta t \ln\left(\frac{RTC^{n-1}_{Q_2 tot}}{p_{eq}}\right) & p > p^a_{eq} \\ 0 & p^d_{eq} < p < p^a_{eq} \\ N^p A^p K_d e^{-\frac{E_d}{RT}} f^{d,n-1}_{H_2} \Delta t \frac{RTC^{n-1}_{Q_2 tot}-p_{eq}}{p_{eq}} & p < p^d_{eq} \end{array}\right. \quad C^{n-1}_{Qtot} > C_{min} \end{array}\right.$$

$$a_{0,pb^0+2} = \left\{ \begin{array}{c} 0 \\ \left\{ \begin{array}{cc} N^p A^p K_a e^{-\frac{E_a}{RT}} f_{H_2}^{a,n-1} \Delta t \ln\left(\frac{RTC_{Q_2tot}^{n-1}}{p_{eq}}\right) & p > p_{eq}^a \\ 0 & p_{eq}^d < p < p_{eq}^a \\ N^p A^p K_d e^{-\frac{E_d}{RT}} f_{H_2}^{d,n-1} \Delta t \frac{RTC_{Q_2tot}^{n-1} - p_{eq}}{p_{eq}} & p < p_{eq}^d \end{array} \right\} \end{array} \begin{array}{l} C_{Qtot}^{n-1} < C_{min} \\ C_{Qtot}^{n-1} > C_{min} \end{array}$$

Balance to T_2 gas

$$a_{1,0} = \left\{ \begin{array}{c} 0 \\ \left\{ \begin{array}{cc} N^p A^p K_a e^{-\frac{E_a}{RT}} f_{T_2}^{a,n-1} \Delta t \frac{C_{max} - C_{Qtot}^{n-1}}{C_{Q_2tot}^{n-1}} & p > p_{eq}^a \\ 0 & p_{eq}^d < p < p_{eq}^a \\ N^p A^p K_d e^{-\frac{E_d}{RT}} f_{T_2}^{d,n-1} RT \Delta t \frac{C_{Qtot}^{n-1} - C_{min}}{p_{eq}} & p < p_{eq}^d \end{array} \right\} \end{array} \begin{array}{l} C_{Qtot}^{n-1} < C_{min} \\ C_{Qtot}^{n-1} > C_{min} \end{array}$$

$$a_{1,1} = Vol_i + A^w k_{d,T_2}^w RT\Delta t +$$

$$+ \left\{ \begin{array}{c} N^p A^p k_{d,T_2}^p RT\Delta t \\ \left\{ \begin{array}{cc} N^p A^p K_a e^{-\frac{E_a}{RT}} f_{T_2}^{a,n-1} \Delta t \frac{C_{max} - C_{Qtot}^{n-1}}{C_{Q_2tot}^{n-1}} & p > p_{eq}^a \\ 0 & p_{eq}^d < p < p_{eq}^a \\ N^p A^p K_d e^{-\frac{E_d}{RT}} f_{T_2}^{d,n-1} RT \Delta t \frac{C_{Qtot}^{n-1} - C_{min}}{p_{eq}} & p < p_{eq}^d \end{array} \right\} \end{array} \begin{array}{l} C_{Qtot}^{n-1} < C_{min} \\ C_{Qtot}^{n-1} > C_{min} \end{array}$$

$$a_{1,2} = \left\{ \begin{array}{c} 0 \\ \left\{ \begin{array}{cc} N^p A^p K_a e^{-\frac{E_a}{RT}} f_{T_2}^{a,n-1} \Delta t \frac{C_{max} - C_{Qtot}^{n-1}}{C_{Q_2tot}^{n-1}} & p > p_{eq}^a \\ 0 & p_{eq}^d < p < p_{eq}^a \\ N^p A^p K_d e^{-\frac{E_d}{RT}} f_{T_2}^{d,n-1} RT \Delta t \frac{C_{Qtot}^{n-1} - C_{min}}{p_{eq}} & p < p_{eq}^d \end{array} \right\} \end{array} \begin{array}{l} C_{Qtot}^{n-1} < C_{min} \\ C_{Qtot}^{n-1} > C_{min} \end{array}$$

$$a_{1,3} = -2A^w K_{r,T_2}^w C_H^{w,n-1} \Delta t$$

$$a_{1,pb^0+1} = \left\{ \begin{array}{c} 0 \\ \left\{ \begin{array}{cc} N^p A^p K_a e^{-\frac{E_a}{RT}} f_{T_2}^{a,n-1} \Delta t \ln\left(\frac{RTC_{Q_2tot}^{n-1}}{p_{eq}}\right) & p > p_{eq}^a \\ 0 & p_{eq}^d < p < p_{eq}^a \\ N^p A^p K_d e^{-\frac{E_d}{RT}} f_{T_2}^{d,n-1} \Delta t \frac{RTC_{Q_2tot}^{n-1} - p_{eq}}{p_{eq}} & p < p_{eq}^d \end{array} \right\} \end{array} \begin{array}{l} C_{Qtot}^{n-1} < C_{min} \\ C_{Qtot}^{n-1} > C_{min} \end{array}$$

$$a_{1,pb^0+2} = \left\{ \begin{array}{c} -2N^p A^p K_{r,T_2}^p C_T^{sp,n-1} \Delta t \\ \left\{ \begin{array}{cc} N^p A^p K_a e^{-\frac{E_a}{RT}} f_{T_2}^{a,n-1} \Delta t \ln\left(\frac{RTC_{Q_2tot}^{n-1}}{p_{eq}}\right) & p > p_{eq}^a \\ 0 & p_{eq}^d < p < p_{eq}^a \\ N^p A^p K_d e^{-\frac{E_d}{RT}} f_{T_2}^{d,n-1} \Delta t \frac{RTC_{Q_2tot}^{n-1} - p_{eq}}{p_{eq}} & p < p_{eq}^d \end{array} \right\} \end{array} \begin{array}{l} C_{Qtot}^{n-1} < C_{min} \\ C_{Qtot}^{n-1} > C_{min} \end{array}$$

Balance to HT gas

$$a_{2,0} = \begin{cases} \begin{cases} 0 & p > p^a_{eq} \\ N^p A^p K_a e^{-\frac{E_a}{RT}} f^{a,n-1}_{HT} \Delta t \frac{C_{max} - C^{n-1}_{Qtot}}{C^{n-1}_{Q_2 tot}} & p^d_{eq} < p < p^a_{eq} \\ 0 & p < p^d_{eq} \\ N^p A^p K_d e^{-\frac{E_d}{RT}} f^{d,n-1}_{HT} RT \Delta t \frac{C^{n-1}_{Qtot} - C_{min}}{p_{eq}} & \end{cases} & C^{n-1}_{Qtot} > C_{min} \\ 0 & C^{n-1}_{Qtot} < C_{min} \end{cases}$$

$$a_{2,1} = \begin{cases} \begin{cases} 0 & p > p^a_{eq} \\ N^p A^p K_a e^{-\frac{E_a}{RT}} f^{a,n-1}_{HT} \Delta t \frac{C_{max} - C^{n-1}_{Qtot}}{C^{n-1}_{Q_2 tot}} & p^d_{eq} < p < p^a_{eq} \\ 0 & p < p^d_{eq} \\ N^p A^p K_d e^{-\frac{E_d}{RT}} f^{d,n-1}_{HT} RT \Delta t \frac{C^{n-1}_{Qtot} - C_{min}}{p_{eq}} & \end{cases} & C^{n-1}_{Qtot} > C_{min} \\ 0 & C^{n-1}_{Qtot} < C_{min} \end{cases}$$

$$a_{2,2} = Vol_i + A^w k^w_{d,HT} RT \Delta t +$$

$$+ \begin{cases} \begin{cases} 0 & p > p^a_{eq} \\ N^p A^p K_a e^{-\frac{E_a}{RT}} f^{a,n-1}_{HT} \Delta t \frac{C_{max} - C^{n-1}_{Qtot}}{C^{n-1}_{Q_2 tot}} & p^d_{eq} < p < p^a_{eq} \\ 0 & p < p^d_{eq} \\ N^p A^p K_d e^{-\frac{E_d}{RT}} f^{d,n-1}_{HT} RT \Delta t \frac{C^{n-1}_{Qtot} - C_{min}}{p_{eq}} & \end{cases} & C^{n-1}_{Qtot} > C_{min} \\ N^p A^p k^p_{d,HT} RT \Delta t & C^{n-1}_{Qtot} < C_{min} \end{cases}$$

$$a_{2,3} = -A^w K^w_{r,HT} C^{w,n-1}_T \Delta t$$

$$a_{2,4} = -A^w K^w_{r,HT} C^{w,n-1}_H \Delta t$$

$$a_{1,pb^0+1} = \begin{cases} \begin{cases} N^p A^p K_a e^{-\frac{E_a}{RT}} f^{a,n-1}_{HT} \Delta t \ln\left(\frac{RTC^{n-1}_{Q_2 tot}}{p_{eq}}\right) & p > p^a_{eq} \\ 0 & p^d_{eq} < p < p^a_{eq} \\ N^p A^p K_d e^{-\frac{E_d}{RT}} f^{d,n-1}_{HT} \Delta t \frac{RTC^{n-1}_{Q_2 tot} - p_{eq}}{p_{eq}} & p < p^d_{eq} \end{cases} & C^{n-1}_{Qtot} > C_{min} \\ -N^p A^p K^p_{r,HT} C^{sp,n-1}_T \Delta t & C^{n-1}_{Qtot} < C_{min} \end{cases}$$

$$a_{1,pb^0+2} = \begin{cases} \begin{cases} N^p A^p K_a e^{-\frac{E_a}{RT}} f^{a,n-1}_{HT} \Delta t \ln\left(\frac{RTC^{n-1}_{Q_2 tot}}{p_{eq}}\right) & p > p^a_{eq} \\ 0 & p^d_{eq} < p < p^a_{eq} \\ N^p A^p K_d e^{-\frac{E_d}{RT}} f^{d,n-1}_{HT} \Delta t \frac{RTC^{n-1}_{Q_2 tot} - p_{eq}}{p_{eq}} & p < p^d_{eq} \end{cases} & C^{n-1}_{Qtot} > C_{min} \\ -N^p A^p K^p_{r,HT} C^{sp,n-1}_H \Delta t & C^{n-1}_{Qtot} < C_{min} \end{cases}$$

Balance to H at pebble surface

$$a_{pb^0+1,0} = \begin{cases} -2RTK^p_{d,H_2} & C^{n-1}_{Qtot} < C_{min} \\ \begin{cases} -K_a e^{-\frac{E_a}{RT}} f^{a,n-1}_H \frac{C_{max}-C^{n-1}_{Qtot}}{C^{n-1}_{Q_2tot}} & p > p^a_{eq} \\ 0 & p^d_{eq} < p < p^a_{eq} \\ -K_d e^{-\frac{E_d}{RT}} f^{d,n-1}_H RT \frac{C^{n-1}_{Qtot}-C_{min}}{p_{eq}} & p < p^d_{eq} \end{cases} & C^{n-1}_{Qtot} > C_{min} \end{cases}$$

$$a_{pb^0+1,1} = \begin{cases} 0 & C^{n-1}_{Qtot} < C_{min} \\ \begin{cases} -K_a e^{-\frac{E_a}{RT}} f^{a,n-1}_H \frac{C_{max}-C^{n-1}_{Qtot}}{C^{n-1}_{Q_2tot}} & p > p^a_{eq} \\ 0 & p^d_{eq} < p < p^a_{eq} \\ -K_d e^{-\frac{E_d}{RT}} f^{d,n-1}_H RT \frac{C^{n-1}_{Qtot}-C_{min}}{p_{eq}} & p < p^d_{eq} \end{cases} & C^{n-1}_{Qtot} > C_{min} \end{cases}$$

$$a_{pb^0+1,2} = \begin{cases} -RTK^p_{d,HT} & C^{n-1}_{Qtot} < C_{min} \\ \begin{cases} -K_a e^{-\frac{E_a}{RT}} f^{a,n-1}_H \frac{C_{max}-C^{n-1}_{Qtot}}{C^{n-1}_{Q_2tot}} & p > p^a_{eq} \\ 0 & p^d_{eq} < p < p^a_{eq} \\ -K_d e^{-\frac{E_d}{RT}} f^{d,n-1}_H RT \frac{C^{n-1}_{Qtot}-C_{min}}{p_{eq}} & p < p^d_{eq} \end{cases} & C^{n-1}_{Qtot} > C_{min} \end{cases}$$

$$a_{pb^0+1,pb^0+1} = \frac{2D_H}{\Delta r} + \begin{cases} 4k^p_{r,H_2} C^{sp,n-1}_H + k^p_{r,HT} C^{sp,n-1}_T & C^{n-1}_{Qtot} < C_{min} \\ \begin{cases} K_a e^{-\frac{E_a}{RT}} f^{a,n-1}_H \ln\left(\frac{RTC^{n-1}_{Q_2tot}}{p_{eq}}\right) & p > p^a_{eq} \\ 0 & p^d_{eq} < p < p^a_{eq} \\ -K_d e^{-\frac{E_d}{RT}} f^{d,n-1}_H \frac{RTC^{n-1}_{Q_2tot}-p_{eq}}{p_{eq}} & p < p^d_{eq} \end{cases} & C^{n-1}_{Qtot} > C_{min} \end{cases}$$

$$a_{pb^0+1,pb^0+2} = \begin{cases} k^p_{r,HT} C^{sp,n-1}_H & C^{n-1}_{Qtot} < C_{min} \\ \begin{cases} K_a e^{-\frac{E_a}{RT}} f^{a,n-1}_H \ln\left(\frac{RTC^{n-1}_{Q_2tot}}{p_{eq}}\right) & p > p^a_{eq} \\ 0 & p^d_{eq} < p < p^a_{eq} \\ -K_d e^{-\frac{E_d}{RT}} f^{d,n-1}_H \frac{RTC^{n-1}_{Q_2tot}-p_{eq}}{p_{eq}} & p < p^d_{eq} \end{cases} & C^{n-1}_{Qtot} > C_{min} \end{cases}$$

$$a_{pb^0+1,pb^0+3} = -\frac{2D_H}{\Delta r}$$

Balance to T at pebble surface

$$a_{pb^0+2,0} = \begin{cases} 0 & C^{n-1}_{Qtot} < C_{min} \\ \begin{cases} -K_a e^{-\frac{E_a}{RT}} f_T^{a,n-1} \frac{C_{max}-C^{n-1}_{Qtot}}{C^{n-1}_{Q_2 tot}} & p > p^a_{eq} \\ 0 & p^d_{eq} < p < p^a_{eq} \\ -K_d e^{-\frac{E_d}{RT}} f_T^{d,n-1} RT \frac{C^{n-1}_{Qtot}-C_{min}}{p_{eq}} & p < p^d_{eq} \end{cases} & C^{n-1}_{Qtot} > C_{min} \end{cases}$$

$$a_{pb^0+2,1} = \begin{cases} -2RTK^p_{d,T_2} & C^{n-1}_{Qtot} < C_{min} \\ \begin{cases} -K_a e^{-\frac{E_a}{RT}} f_T^{a,n-1} \frac{C_{max}-C^{n-1}_{Qtot}}{C^{n-1}_{Q_2 tot}} & p > p^a_{eq} \\ 0 & p^d_{eq} < p < p^a_{eq} \\ -K_d e^{-\frac{E_d}{RT}} f_T^{d,n-1} RT \frac{C^{n-1}_{Qtot}-C_{min}}{p_{eq}} & p < p^d_{eq} \end{cases} & C^{n-1}_{Qtot} > C_{min} \end{cases}$$

$$a_{pb^0+2,2} = \begin{cases} -RTK^p_{d,HT} & C^{n-1}_{Qtot} < C_{min} \\ \begin{cases} -K_a e^{-\frac{E_a}{RT}} f_T^{a,n-1} \frac{C_{max}-C^{n-1}_{Qtot}}{C^{n-1}_{Q_2 tot}} & p > p^a_{eq} \\ 0 & p^d_{eq} < p < p^a_{eq} \\ -K_d e^{-\frac{E_d}{RT}} f_T^{d,n-1} RT \frac{C^{n-1}_{Qtot}-C_{min}}{p_{eq}} & p < p^d_{eq} \end{cases} & C^{n-1}_{Qtot} > C_{min} \end{cases}$$

$$a_{pb^0+1,pb^0+1} = \begin{cases} k^p_{r,HT} C^{sp,n-1}_H & C^{n-1}_{Qtot} < C_{min} \\ \begin{cases} K_a e^{-\frac{E_a}{RT}} f_T^{a,n-1} \ln\left(\frac{RTC^{n-1}_{Q_2 tot}}{p_{eq}}\right) & p > p^a_{eq} \\ 0 & p^d_{eq} < p < p^a_{eq} \\ -K_d e^{-\frac{E_d}{RT}} f_T^{d,n-1} \frac{RTC^{n-1}_{Q_2 tot}-p_{eq}}{p_{eq}} & p < p^d_{eq} \end{cases} & C^{n-1}_{Qtot} > C_{min} \end{cases}$$

$$a_{pb^0+2,pb^0+2} = \frac{2D_H}{\Delta r} + \begin{cases} 4k^p_{r,H_2} C^{sp,n-1}_H + k^p_{r,HT} C^{sp,n-1}_T & C^{n-1}_{Qtot} < C_{min} \\ \begin{cases} K_a e^{-\frac{E_a}{RT}} f_T^{a,n-1} \ln\left(\frac{RTC^{n-1}_{Q_2 tot}}{p_{eq}}\right) & p > p^a_{eq} \\ 0 & p^d_{eq} < p < p^a_{eq} \\ -K_d e^{-\frac{E_d}{RT}} f_T^{d,n-1} \frac{RTC^{n-1}_{Q_2 tot}-p_{eq}}{p_{eq}} & p < p^d_{eq} \end{cases} & C^{n-1}_{Qtot} > C_{min} \end{cases}$$

$$a_{pb^0+2,pb^0+N^l+3} = -\frac{2D_H}{\Delta r}$$

H diffusion inside the pebble

For $j = 1$ (outer layer):

$$a_{pb^0+3,pb^0+1} = -\frac{2r_p^2}{\Delta r} D_H \Delta t$$

$$a_{pb^0+3,pb^0+3} = \frac{1}{3}\left((r_p)^3 - (r_p - \Delta r)^3\right) + \frac{2r_p^2}{\Delta r} D_H \Delta t + \frac{(r_p - \Delta r)^2}{\Delta r} D_H \Delta t$$

$$a_{pb^0+3,pb^0+4} = -\frac{(r_p - \Delta r)^2}{\Delta r} D_H \Delta t$$

For $j \in \left[2, N^{lp} - 1\right]$ (intermediate layers):

$$a_{pb^0+2+j,pb^0+1+j} = -\frac{1}{\Delta r}\left(\left(N^{lp} - j + \frac{1}{2}\right)\Delta r\right)^2 D_H \Delta t$$

$$a_{pb^0+2+j,pb^0+2+j} = \frac{1}{3}\left(\left(\left(N^{lp} - j + 1/\right)\Delta r\right)^3 - \left(\left(N^{lp} - j - \frac{1}{2}\right)\Delta r\right)^3\right) +$$

$$+\frac{1}{\Delta r}\left(\left(N^{lp} - j + \frac{1}{2}\right)\Delta r\right)^2 D_{H} \Delta t + \frac{1}{\Delta r}\left(\left(N^{lp} - j - \frac{1}{2}\right)\Delta r\right)^2 D_H \Delta t$$

$$a_{pb^0+2+j,pb^0+3+j} = -\frac{1}{\Delta r}\left(\left(N^{lp} - j - \frac{1}{2}\right)\Delta r\right)^2 D_H \Delta t$$

For $j = N^{lp}$ (core layer):

$$a_{pb^0+2+N^{lp},pb^0+1+N^{lp}} = -\frac{(\Delta r/2)^2}{\Delta r} D_H \Delta t$$

$$a_{pb^0+2+N^{lp},pb^0+1+N^{lp}} = \frac{1}{3}\left(\frac{\Delta r}{2}\right)^3 + \frac{(\Delta r/2)^2}{\Delta r} D_H \Delta t$$

T diffusion inside the pebble

For $j = 1$ (outer layer):

$$a_{pb^0+3+N^{lp},pb^0+2} = -\frac{2r_p^2}{\Delta r} D_T \Delta t$$

$$a_{pb^0+3+N^{lp},pb^0+3+N^{lp}} = \frac{1}{3}\left((r_p)^3 - (r_p - \Delta r)^3\right) + \frac{2r_p^2}{\Delta r} D_T \Delta t + \frac{(r_p - \Delta r)^2}{\Delta r} D_T \Delta t$$

$$a_{pb^0+3+N^{lp},pb^0+4+N^{lp}} = -\frac{(r_p-\Delta r)^2}{\Delta r} D_T \Delta t$$

For $j \in \left[2, N^{lp}-1\right]$ (intermediate layers):

$$a_{pb^0+2+N^{lp}+j,pb^0+1+N^{lp}+j} = -\frac{1}{\Delta r}\left(\left(N^{lp}-j+\frac{1}{2}\right)\Delta r\right)^2 D_T \Delta t$$

$$a_{pb^0+2+N^{lp}+j,pb^0+2+N^{lp}+j} = \frac{1}{3}\left(\left(\left(N^{lp}-j+\frac{1}{2}\right)\Delta r\right)^3 - \left(\left(N^{lp}-j-\frac{1}{2}\right)\Delta r\right)^3\right) +$$

$$+\frac{1}{\Delta r}\left(\left(N^{lp}-j+\frac{1}{2}\right)\Delta r\right)^2 D_T \Delta t + \frac{1}{\Delta r}\left(\left(N^{lp}-j-\frac{1}{2}\right)\Delta r\right)^2 D_T \Delta t$$

$$a_{pb^0+2+N^{lp}+j,pb^0+3+N^{lp}+j} = -\frac{1}{\Delta r}\left(\left(N^{lp}-j-\frac{1}{2}\right)\Delta r\right)^2 D_T \Delta t$$

For $j = N^{lp}$ (core layer):

$$a_{pb^0+2+2N^{lp},pb^0+2+2N^{lp}-1} = -\frac{(\Delta r/2)^2}{\Delta r} D_H \Delta t$$

$$a_{pb^0+2+2N^{lp},pb^0+2+2N^{lp}} = \frac{1}{3}\left(\frac{\Delta r}{2}\right)^3 + \frac{(\Delta r/2)^2}{\Delta r} D_H \Delta t$$

B.2.2. Independent terms matrix $[B]$

Balance to H_2 gas

$$b_0 = Vol_i C_{H_2}^{n-1} + \Delta t D_{H_2}\left(\frac{C_{H_2,i-1}^{n-1} - C_{H_2,i}^{n-1}}{\Delta x^2} - \frac{C_{H_2,i}^{n-1} - C_{H_2,i+1}^{n-1}}{\Delta x^2}\right) + \dot{V}\left(C_{H_2,i-1}^{n-1} - C_{H_2,i}^{n-1}\right) - \Delta t A^w k_{r,H_2}^w \left(C_H^{w,n-1}\right)^2 +$$

$$+ \begin{cases} \begin{cases} N^p A^p k_{r,H_2}^p \left(C_H^{sp,n-1}\right)^2 & \\ N^p A^p K_a e^{-\frac{E_a}{RT}} f_{H_2}^{a,n-1} \Delta t \left(C_{max}\left(\ln\left(\frac{RTC_{Q_2tot}^{n-1}}{p_{eq}}\right) - 1\right) - C_{Qtot}^{n-1}\right) & p > p_{eq}^a \\ 0 & p_{eq}^d < p < p_{eq}^a \\ N^p A^p K_d e^{-\frac{E_d}{RT}} f_{H_2}^{d,n-1} \Delta t \left(\frac{p_{eq}-RTC_{Q_2tot}^{n-1}}{p_{eq}} C_{min} - RT\frac{C_{Qtot}^{n-1}-C_{min}}{p_{eq}} C_{Q_2tot}^{n-1}\right) & p < p_{eq}^d \end{cases} & \begin{matrix} C_{Qtot}^{n-1} < C_{min} \\ \\ C_{Qtot}^{n-1} > C_{min} \end{matrix} \end{cases}$$

Balance to T_2 gas

$$b_1 = Vol_i C_{T_2}^{n-1} + \Delta t D_{T_2}\left(\frac{C_{T_2,i-1}^{n-1} - C_{T_2,i}^{n-1}}{\Delta x^2} - \frac{C_{T_2,i}^{n-1} - C_{T_2,i+1}^{n-1}}{\Delta x^2}\right) + \dot{V}\left(C_{T_2,i-1}^{n-1} - C_{T_2,i}^{n-1}\right) - \Delta t A^w k_{r,T_2}^w \left(C_T^{w,n-1}\right)^2 +$$
$$+ \begin{cases} N^p A^p k_{r,T_2}^p \left(C_T^{sp,n-1}\right)^2 & C_{Qtot}^{n-1} < C_{min} \\ \begin{cases} N^p A^p K_a e^{-\frac{E_a}{RT}} f_{T_2}^{a,n-1} \Delta t \left(C_{max}\left(\ln\left(\frac{RTC_{Q_2tot}^{n-1}}{p_{eq}}\right) - 1\right) - C_{Qtot}^{n-1}\right) & p > p_{eq}^a \\ 0 & p_{eq}^d < p < p_{eq}^a \\ N^p A^p K_d e^{-\frac{E_d}{RT}} f_{T_2}^{d,n-1} \Delta t \left(\frac{p_{eq} - RTC_{Q_2tot}^{n-1}}{p_{eq}} C_{min} - RT\frac{C_{Qtot}^{n-1} - C_{min}}{p_{eq}} C_{Q_2tot}^{n-1}\right) & p < p_{eq}^d \end{cases} & C_{Qtot}^{n-1} > C_{min} \end{cases}$$

Balance to HT gas

$$b_2 = Vol_i C_{HT}^{n-1} + \Delta t D_{HT}\left(\frac{C_{HT,i-1}^{n-1} - C_{HT,i}^{n-1}}{\Delta x^2} - \frac{C_{HT,i}^{n-1} - C_{HT,i+1}^{n-1}}{\Delta x^2}\right) + \dot{V}\left(C_{HT,i-1}^{n-1} - C_{HT,i}^{n-1}\right) - \Delta t A^w k_{r,HT}^w C_H^{w,n-1} C_T^{w,n-1} +$$
$$+ \begin{cases} N^p A^p k_{r,HT}^p C_H^{sp,n-1} C_T^{sp,n-1} & C_{Qtot}^{n-1} < C_{min} \\ \begin{cases} N^p A^p K_a e^{-\frac{E_a}{RT}} f_{HT}^{a,n-1} \Delta t \left(C_{max}\left(\ln\left(\frac{RTC_{Q_2tot}^{n-1}}{p_{eq}}\right) - 1\right) - C_{Qtot}^{n-1}\right) & p > p_{eq}^a \\ 0 & p_{eq}^d < p < p_{eq}^a \\ N^p A^p K_d e^{-\frac{E_d}{RT}} f_{HT}^{d,n-1} \Delta t \left(\frac{p_{eq} - RTC_{Q_2tot}^{n-1}}{p_{eq}} C_{min} - RT\frac{C_{Qtot}^{n-1} - C_{min}}{p_{eq}} C_{Q_2tot}^{n-1}\right) & p < p_{eq}^d \end{cases} & C_{Qtot}^{n-1} > C_{min} \end{cases}$$

Balance to H at pebble surface

$$b_{pb^0+1} = \begin{cases} 2k_{r,H_2}^p \left(C_H^{sp,n-1}\right)^2 + k_{r,HT}^p C_H^{sp,n-1} C_T^{sp,n-1} & C_{Qtot}^{n-1} < C_{min} \\ \begin{cases} K_a e^{-\frac{E_a}{RT}} f_H^{a,n-1} \left(C_{max}\left(\ln\left(\frac{RTC_{Q_2tot}^{n-1}}{p_{eq}}\right) - 1\right) - C_{Qtot}^{n-1}\right) & p > p_{eq}^a \\ 0 & p_{eq}^d < p < p_{eq}^a \\ K_d e^{-\frac{E_d}{RT}} f_H^{d,n-1} \left(RT\frac{C_{Qtot}^{n-1} - C_{min}}{p_{eq}} C_{Q_2tot}^{n-1} - \frac{p_{eq} - RTC_{Q_2tot}^{n-1}}{p_{eq}} C_{min}\right) & p < p_{eq}^d \end{cases} & C_{Qtot}^{n-1} > C_{min} \end{cases}$$

Balance to T at pebble surface

$$b_{pb^0+2} = \begin{cases} 2k_{r,T_2}^p \left(C_T^{sp,n-1}\right)^2 + k_{r,HT}^p C_H^{sp,n-1} C_T^{sp,n-1} & C_{Qtot}^{n-1} < C_{min} \\ \begin{cases} K_a e^{-\frac{E_a}{RT}} f_T^{a,n-1} \left(C_{max}\left(\ln\left(\frac{RTC_{Q_2tot}^{n-1}}{p_{eq}}\right) - 1\right) - C_{Qtot}^{n-1}\right) & p > p_{eq}^a \\ 0 & p_{eq}^d < p < p_{eq}^a \\ K_d e^{-\frac{E_d}{RT}} f_T^{d,n-1} \left(RT\frac{C_{Qtot}^{n-1} - C_{min}}{p_{eq}} C_{Q_2tot}^{n-1} - \frac{p_{eq} - RTC_{Q_2tot}^{n-1}}{p_{eq}} C_{min}\right) & p < p_{eq}^d \end{cases} & C_{Qtot}^{n-1} > C_{min} \end{cases}$$

H diffusion inside the pebble

For $j = 1$ (outer layer):

$$b_{pb^0+3} = \frac{1}{3}\left((r_p)^3 - (r_p - \Delta r)^3\right) C_H^{p1,n-1}$$

For $j \in \left[2, N^{lp} - 1\right]$ (intermediate layers):

$$b_{pb^0+2+j} = \frac{1}{3}\left(\left(\left(N^{lp} - j + \frac{1}{2}\right)\Delta r\right)^3 - \left(\left(N^{lp} - j - \frac{1}{2}\right)\Delta r\right)^3\right) C_H^{pj,n-1}$$

For $j = N^{lp}$ (core layer):

$$b_{pb^0+2+N^{lp}} = \frac{1}{3}\left(\frac{\Delta r}{2}\right)^3 C_H^{pN^{lp},n-1}$$

T diffusion inside the pebble

For $j = 1$ (outer layer):

$$b_{pb^0+3+N^{lp}} = \frac{1}{3}\left((r_p)^3 - (r_p - \Delta r)^3\right) C_T^{p1,n-1}$$

For $j \in \left[2, N^{lp} - 1\right]$ (intermediate layers):

$$b_{pb^0+N^{lp}+2+j} = \frac{1}{3}\left(\left(\left(N^{lp} - j + \frac{1}{2}\right)\Delta r\right)^3 - \left(\left(N^{lp} - j - \frac{1}{2}\right)\Delta r\right)^3\right) C_T^{pj,n-1}$$

For $j = N^{lp}$ (core layer):

$$b_{pb^0+2+2N^{lp}} = \frac{1}{3}\left(\frac{\Delta r}{2}\right)^3 C_T^{pN^{lp},n-1}$$

C. Large Set Up Thermal Analysis

This brief appendix shows how has been considered the thermal analysis and the results of the large set up reactor proposal shown in section 8.3.

C.1. Data

Boundary conditions

$$T_{amb} = 20\ [C] \qquad \text{Ambient temperature}$$

$$T_{in} = 500\ [C] \qquad \text{Argon inlet temperature}$$

$$p_{Ar} = 150\ [KPa] \qquad \text{Argon pressure}$$

$$p_{Atm} = 101\ [KPa] \qquad \text{Atmospheric pressure}$$

Flow

$$\dot{V}_{Ar} = 600\ [mL/min] \qquad \text{Volumetric flow}$$

$$\dot{m}_{Ar} = \dot{V}_{Ar} \cdot \left| 1.66667 \times 10^{-8}\ \frac{m^3/s}{mL/min} \right| \cdot \rho_{Ar} \qquad \text{Mass flow}$$

Geometry

$$L = 60\ [m] \qquad \text{Pipe length}$$

$$d = (1/4)\ [in] \cdot \left| 0.0254\ \frac{m}{in} \right| \qquad \text{Exterior diameter}$$

$$e_t = 0.035\ [in] \cdot \left| 0.0254\ \frac{m}{in} \right| \qquad \text{Pipe thickness}$$

$$r_e = d/2 \qquad \text{Exterior pipe radius}$$

$$r_i = d/2 - e_t \qquad \text{Internal pipe radius}$$

$$D = 0.4\ [m] \qquad \text{Reactor diameter}$$

$$H = 0.51\ [m] \qquad \text{Reactor height}$$

$$e_{ais} = 5\ [cm] \cdot \left| 0.01\ \frac{m}{cm} \right| \qquad \text{Isolating thickness}$$

$$\Delta L = L/N_s \qquad \text{The pipe is discretized into } N_s = 500 \text{ layers.}$$

$$A_{R,i} = 2 \cdot \left(\pi \cdot \frac{D^2}{4}\right) + \pi \cdot D \cdot H \qquad \text{Internal reactor surface area}$$

$$A_{R,o} = 2 \cdot \left(\pi \cdot \frac{(D + e_{ais})^2}{4}\right) + \pi \cdot (D + e_{ais}) \cdot H \qquad \text{External reactor surface area}$$

$$A_{t,i} = \pi \cdot (d - 2 \cdot e_t) \cdot \Delta L \qquad \text{Internal, tube surface (section)}$$

$$A_{t,o} = \pi \cdot (d) \cdot \Delta L \qquad \text{External, tube surface (section)}$$

$$Vol = H \cdot \pi \cdot \frac{D^2}{4} - L \cdot \pi \cdot \frac{d^2}{4} \qquad \text{Reactor volume}$$

,

Properties

$$K_t = 20.04\,[W/m \cdot K] \qquad \text{Stainless steel AISI316 thermal conductivity}$$

$$K_{ais} = 0.04\ [W/m \cdot K] \qquad \text{Glass wool thermal conductivity}$$

$$\rho_{Ar,i} = \rho\left(Ar,\ p\ = p_{Ar},\ T = \bar{T}_i\ [C]\right) \qquad \text{Density}$$

$$Cp_{Ar,i} = C_p\left(Ar,\ T = \bar{T}_i\ [C]\right) \qquad \text{Heat capacity}$$

Convective heat transfer coefficients

$$h_{cv,R,i} = 2\ \left[W/K \cdot m^2\right] \qquad \text{Free convection over vertical wall, closed volume}$$

$$h_{cv,R,o} = 5\ \left[W/K \cdot m^2\right] \qquad \text{Free convection over vertical wall, exterior}$$

$$h_{cv,t,i} = 10\ \left[W/K \cdot m^2\right] \qquad \text{Forced convection inside a pipe, laminar flow}$$

$$h_{cv,t,o} = 5\ \left[W/K \cdot m^2\right] \qquad \text{Free convection at pipe exterior}$$

C.1.1. System of equations

Global transfer coefficient of tube

$$\frac{1}{UA_{t,s}} = \frac{1}{(A_{t,i} \cdot h_{cv,t,i})} + \frac{\ln\left(\frac{d-2\cdot e_t}{d}\right)}{(2 \cdot \pi \cdot K_t \cdot \Delta L)} + \frac{1}{A_{t,o} \cdot h_{cv,t,o}}$$

Thermal resistances of the reactor wall

$$R_{cv,R,i} = \frac{1}{A_{R,i} \cdot h_{cv,R,i}} \qquad \text{Convective at internal wall}$$

$$R_{ais,R} = \frac{e_{ais}}{K_{ais} \cdot (A_{R,i}/2 + A_{R,o}/2)} \qquad \text{Conductive}$$

$$R_{cv,R,o} = \frac{1}{A_{R,o} \cdot h_{cv,R,o}} \qquad \text{Convective at external wall}$$

Node temperatures

$$T_{in} = T_{in,1} \qquad \text{First slice inlet temperature}$$

$$T_{out} = T_{out,N,s} \qquad \text{Outlet flow temperature}$$

$$\bar{T}_i = \frac{T_{in,i} + T_{out,i}}{2} \quad \text{for } i = 1,\ N_s \qquad \text{Average slice temperature}$$

$$T_{out,i} = T_{in,i+1} \quad \text{for } i = 1,\ N_s - 1 \qquad \text{Boundaries}$$

Heat balances

$$\dot{W} = 0\ [W] \qquad \text{Power provided by a heater}$$

$$\dot{Q}_{s,i} = \dot{m}_{Ar} \cdot Cp_{Ar} \cdot (T_{in,i} - T_{out,i}) \quad \text{for } i = 1,\ N_s \qquad \text{Argon flow heat capacity}$$

$$\dot{Q}_{s,i} = UA_{t,s} \cdot \left(\bar{T}_i - T_V\right) \quad \text{for } i = 1,\ N_s \qquad \text{Argon flow heat transfered}$$

$$\dot{Q}_t = \sum \dot{Q}_{s,1..N,s} \qquad \text{Total heat of all slices}$$

$$\dot{Q}_R = \frac{T_V - T_{s,i}}{R_{cv,R,i}} = \frac{T_{s,i} - T_{s,o}}{R_{ais,R}} \qquad \text{Heat scaping out of the reactor}$$

$$\dot{Q}_R = \frac{T_{s,o} - T_{amb}}{R_{cv,R,o}} + \sigma \cdot A_{R,o} \cdot \epsilon \cdot \left(T_{s,o,K}^4 - T_{amb,K}^4\right)$$

$$\dot{W} + \dot{Q}_t = \dot{Q}_R \qquad \text{Global balance}$$

C.1.2. Results

As figure C.1 shows, no matter how well isolated is the reactor, due to its big size, the heat loss is always much larger than the heat supplied by the hot argon flow. Indeed, the fluid only takes few centimetres to be cooled down to reactor temperature, which ends up being quite close to the environment one (27.3°C). This is because inlet flow only supplies 5.7 *W* of thermal power, which is clearly far of being enough for heating up the reactor to the desired temperatures without ancillary heating systems.

All in all, permeation effects are not expected to be seen in this set up since their thermal behaviour does not allow it to be kept at a reasonable temperature.

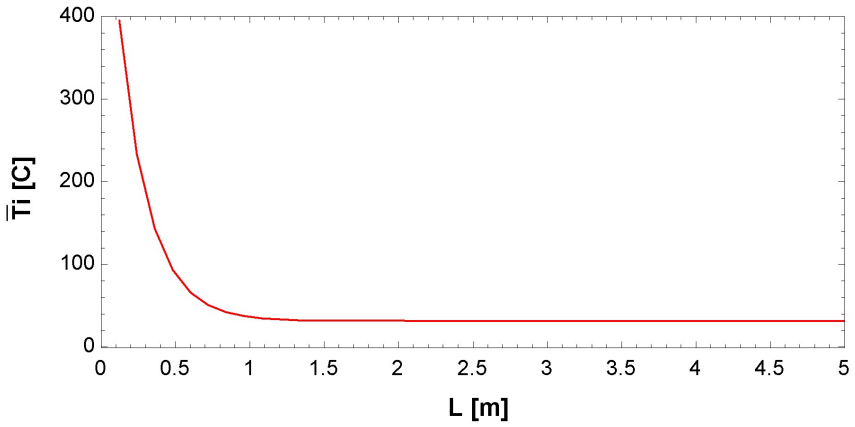

Figure C.1.: Argon temperature evolution in the experimental set up pipe.